UNIVERSITAT DE BARCELONA

Mechanical stress in curved epithelia of designed size and shape

Ariadna Marín Llauradó

ADVERTIMENT. La consulta d'aquesta tesi queda condicionada a l'acceptació de les següents condicions d'ús: La difusió d'aquesta tesi per mitjà del servei TDX (**www.tdx.cat**) i a través del Dipòsit Digital de la UB (**diposit.ub.edu**) ha estat autoritzada pels titulars dels drets de propietat intel·lectual únicament per a usos privats emmarcats en activitats d'investigació i docència. No s'autoritza la seva reproducció amb finalitats de lucre ni la seva difusió i posada a disposició des d'un lloc aliè al servei TDX ni al Dipòsit Digital de la UB. No s'autoritza la presentació del seu contingut en una finestra o marc aliè a TDX o al Dipòsit Digital de la UB (framing). Aquesta reserva de drets afecta tant al resum de presentació de la tesi com als seus continguts. En la utilització o cita de parts de la tesi és obligat indicar el nom de la persona autora.

ADVERTENCIA. La consulta de esta tesis queda condicionada a la aceptación de las siguientes condiciones de uso: La difusión de esta tesis por medio del servicio TDR (**www.tdx.cat**) y a través del Repositorio Digital de la UB (**diposit.ub.edu**) ha sido autorizada por los titulares de los derechos de propiedad intelectual únicamente para usos privados enmarcados en actividades de investigación y docencia. No se autoriza su reproducción con finalidades de lucro ni su difusión y puesta a disposición desde un sitio ajeno al servicio TDR o al Repositorio Digital de la UB. No se autoriza la presentación de su contenido en una ventana o marco ajeno a TDR o al Repositorio Digital de la UB (framing). Esta reserva de derechos afecta tanto al resumen de presentación de la tesis como a sus contenidos. En la utilización o cita de partes de la tesis es obligado indicar el nombre de la persona autora.

WARNING. On having consulted this thesis you're accepting the following use conditions: Spreading this thesis by the TDX (**www.tdx.cat**) service and by the UB Digital Repository (**diposit.ub.edu**) has been authorized by the titular of the intellectual property rights only for private uses placed in investigation and teaching activities. Reproduction with lucrative aims is not authorized nor its spreading and availability from a site foreign to the TDX service or to the UB Digital Repository. Introducing its content in a window or frame foreign to the TDX service or to the UB Digital Repository is not authorized (framing). Those rights affect to the presentation summary of the thesis as well as to its contents. In the using or citation of parts of the thesis it's obliged to indicate the name of the author.

UNIVERSITAT DE BARCELONA

Mechanical stress in curved epithelia of designed size and shape

Memòria per optar al grau de Doctora per la Universitat de Barcelona

Novembre 2021

Presentada per:
Ariadna Marín Llauradó

Dirigida per:
Dr. Xavier Trepat Guixer

To my lab mates,

who were there for me

every step of the way.

Panta rhei (everything flows)

– Heraclitus

PREFACE

A hundred years ago, D'Arcy Thomson already stated that the morphology of live beings depended greatly on physical and mathematical principles. In his book "*On Growth and Form*"[1], he rejected the idea of randomness and chaos, prevalent among his contemporaries, and explained the size and shape of organisms in terms of mechanical phenomena, geometric transformations, and physical constraints.

In the present day, and after more than a century of research, many of the ideas that he postulated still hold. D'Arcy Thompson proposed that principles such as force balance or energy minimisation can be applied to biological systems as they are to inorganic ones. For example, he discussed how force balance at tricellular junctions can lead to the emergence of hexagonal packing when each cell exerts a similar force. This emphasis on the importance of mechanics to study biology is the preface of the field of mechanobiology.

In the past decades, the swift succession of technological advances has allowed us to transition from a qualitative description of biological processes and structures to a quantitative study. This ability to reliably measure magnitudes such as molecular concentrations, times and forces has been key for the advance of mechanobiology and has allowed us to pursue D'Arcy Thompson's ambition: to develop a physical understanding of the processes that underlie biology. In this thesis, I present my modest contribution to this

endeavour: during my PhD, I have analysed how the size and shape of three-dimensional epithelia depend on luminal pressure and mechanical stress.

This thesis has six chapters. In chapter 1, I introduce this work by reviewing the state-of-the-art knowledge of epithelial mechanics, epithelial morphogenesis, and methods to measure mechanics in luminal epithelia. In chapter 2, I expose the aims of the thesis. In chapter 3, I detail the necessary methods to carry out this project. In chapter 4, I expose the results obtained during my PhD work under the supervision of Prof. Xavier Trepat, which has been carried out in close collaboration with the labs of Prof. Marino Arroyo (Universitat Politècnica de Catalunya) and Prof. Sohan Kale (Virginia Tech). In chapter 5, I discuss the implications of our findings, as well as possible future work. Finally, in chapter 6, I the summarize the main conclusions of this thesis.

CONTENTS

CONTENTS

1 INTRODUCTION

Epithelia are ubiquitous tissues that cover the internal and external surfaces of the body, and they carry out many functions such as transport of nutrients, protection against pathogens or compartmentalization[2]. To perform these functions, epithelia fold into three-dimensional structures that often enclose a fluid-filled cavity called lumen. Luminal epithelia can attain a great diversity of shapes, from nearly spherical structures like blastocysts[3], to tubular ones like the lining of the nephrons[4,5], or ellipsoidal ones such as the otic vesicle[6,7]. They can also present a broad range of sizes, from a few microns[8,9] to millimetres[5,10].

The geometry of luminal epithelia is mainly determined by the balance between cellular surface tensions and luminal pressure. Undoubtedly, the research and technological advances of recent years have expanded our knowledge about lumen formation and coalescence [9,11], and the effect of fluid pressure on the surrounding tissues[7,3]. However, how this lumen-epithelium balance is established as a function of shape and size remains an unanswered question. To address this question systematically, we present an experimental and computational approach to design epithelia of controlled size and shape and to map the stress tensor at any monolayer location without assumptions of mechanical properties.

With this in mind, the introduction covers the key properties and mechanics of epithelial tissues, the processes that lead to their three-dimensional folding during morphogenesis and the principal methods to measure their mechanical properties. I first outline the structure of epithelia, including their subcellular cytoskeletal structure, and their ECM and intercellular

adhesions. I then describe their mechanical properties at the cell and tissue level, as well as modelling approaches at both scales. Afterwards, I discuss morphogenetic processes that lead to epithelial folding and growth, and lumenogenesis. Finally, I introduce some invasive and non-invasive methods to measure forces and pressures in luminal epithelial tissues.

1.1 Properties and mechanical models of epithelia

1.1.1 Structure of epithelia

Epithelia are thin cellular sheets that derive from all three embryonic layers. The epithelia lining the skin, the mouth, the nose and the anus develop from the ectoderm. Those of the airways and most of the digestive system derive from the endoderm. Finally, the endothelia that cover vessels in the circulatory and lymphatic system develop from the mesoderm[12].

Since epithelia have very different origins, it should not be striking that they can present many different organizations and shapes. Epithelial sheets can present one or several layers, which classifies them into simple and stratified, respectively. Individual cells can be squamous (flat and thin) or columnar (tall and narrow) and generate different three-dimensional structures such as tubes or folds. All these morphologic characteristics are closely related with the functions they carry out. For example, the epithelium covering the small intestine presents small finger-like projections called villi that increase the surface of the organ, thus allowing more absorption of nutrients. Another example is the skin, which is a squamous stratified epithelium whose many layers act as a barrier to protect the organism from physical and chemical attrition.

Despite these differences, epithelia present many common characteristics that arise from their main function: the separation of compartments. Epithelial cells are densely packed and are generally adhered on a basement membrane, which separates them from the underlying tissue. They usually exhibit a polarized distribution of the organelles and membrane-bound proteins, clearly differentiating the basal surface from the apical one. In the next subsections we will talk about some components that participate in this polarization and play a key role in the mechanical properties of epithelia, namely the cytoskeleton (specially the actomyosin cortex), cell-matrix adhesions and intercellular adhesions.

1.1.1.1 Cytoskeleton and actomyosin cortex

The cytoskeleton is a network of cross-linked protein filaments that spans from the cell nucleus to the inner surface of the cell membrane. This network is constantly destroyed and reassembled, consuming a large part of the metabolic energy of the cell. It is this extremely dynamic remodeling that enables cells to change shape, contract and engulf other objects. The cytoskeleton also has a critical role in cell movement, division, cell-cell adhesion and signaling.

In eukaryotic organisms, the cytoskeleton is formed by three main components: microtubules, intermediate filaments, and actin filaments (**Figure 1**). These components form different networks that interact with each other, as well as with hundreds of regulatory proteins that control filament assembly, link the filaments to other cell components, etc. The most important differences between these three main polymers are their stiffness (the extent to which they resist deformation in response to an applied force), their polarity, the dynamics of their assembly and the molecular motors with which they associate.

Microtubules are composed by α- and β-tubulin monomers. They are long, hollow cylinders with an external diameter of about 25nm[13]. Microtubules are the most rigid filaments of the cytoskeleton and have the most complex assembly dynamics. They commonly originate from the MicroTubule-Organizing Center, MTOC (the centrosome, in animal cells), which acts as an anchor for one of their ends[13]. The two ends of the tubules have a distinct polarity, and they grow at different rates, giving rise to what is called treadmilling: one end grows in length while the other shrinks. The nucleation of α/β-tubulin dimers is accelerated by the presence of the γTuRC (γ-tubulin Ring Complex), that acts as a template[14]. Microtubules are involved in the movement of organelles and vesicles, and they guide and support appendages associated with cell movement (cilia and flagella), among other functions.

Intermediate filaments (IFs) have a diameter of about 8-12nm[13]. They are the least stiff and the most stable components of the cytoskeleton and their contribution to the mechanical properties of the cell is thought to take place primarily at large deformations and long timescales[15]. IFs are also the most heterogeneous components of the cytoskeleton, and the proteins that form them are tissue specific. The most abundant IFs in epithelial cells are keratins, which span the cytoplasm from one intercellular junction to another. Unlike the

other two cytoskeletal components, they are not polarized and, thus, they cannot support directional movement of molecular motors[16].

Actin filaments have a diameter of about 7nm and they are formed by reversible polymerization of G-actin (globular) into F-actin (filamentous)[13]. Like microtubules, these filaments are polarized structures with two ends that grow at different rates, presenting treadmilling. Actin filaments are less rigid than microtubules, even though the abundance of crosslinkers that assemble them leads to the creation of highly organized and stiff networks with different architectures, such as bundles or branched networks (with tree-like structure)[17]. Also unlike microtubules, that extend from one or two central organizing complexes, the actin cytoskeleton is assembled and disassembled in response to local signaling cues.

One of the most crucial features of actin filaments is their ability to contract due to its interaction with the myosin motor proteins that bind and unbind actin cyclically thanks to ATP hydrolysis; a macroscopic consequence of this actomyosin binding is that of muscle contraction. Non-muscle cells present a specific type of myosin, non-muscle myosin II, that associates with actin to form thick contractile bundles named stress fibers. These **stress fibers** provide mechanical support for cells by connecting with the extracellular matrix through cell-matrix adhesions and with other cells through intercellular adhesions[16].

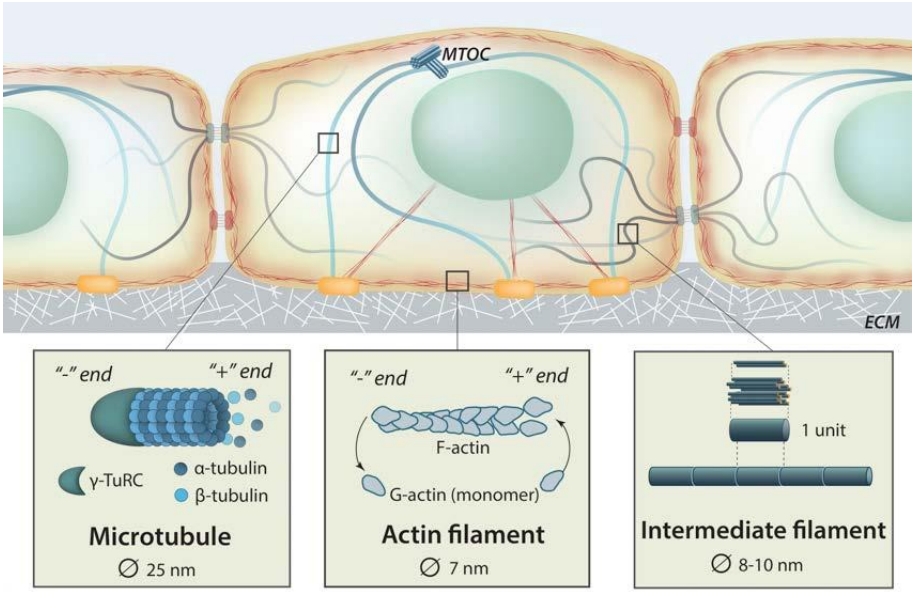

***Figure 1: Main components of the cytoskeleton**. Scheme showing the main components of the cytoskeleton (microtubules, actin filaments and intermediate filaments) and their structure in epithelial cells. Adapted from ref.*18.

In most animal cells, the actin cytoskeleton is dispersed through the cell, but it is most concentrated in the **actomyosin cortex** (or cell cortex). The cell cortex is a thin (about 200 nm) and dense layer of actin filaments, myosin and actin binding proteins that is bound to the cell membrane[19]. Myosin pulls on actin filaments and generates internal contractile forces in this network that give rise to cortical tension. Both the cortex and the cell membrane contribute to cellular surface tension, but cortical tension is more than one order of magnitude higher, thus dominating the mechanical properties of the cell[20].

One of the mechanisms known to control cortical tension is the regulation of the abundance and activity of myosins downstream of Rho-GTPase signalling. Rho-GTPases cycle between an active (GTP-bound) and an inactive (GDP-bound) state thanks to regulatory proteins. Among Rho-GTPases, RhoA stands out for its activity in the cell cortex. RhoA activates Rho-kinase (ROCK), that increases myosin activity by direct phosphorylation. Moreover, RhoA also modulates the organization of actin filaments by activating formins, a group of proteins involved in actin polymerization. Other proteins that play a key role in cortical organization and, consequently, in cortical tension, are the formin mDia, that polymerizes linear filament arrays, and the Arp2/3 complex, that drives branching of filaments[19] (**Figure 2**).

The main function of the cortex is controlling the shape of animal cells. This includes homeostatic situations, as well as processes that involve large remodelling, like facilitating cell migration through cytoplasmatic projections such as lamellipodia or filopodia. Local changes in cortical tension at the cell-cell interface influence the formation of intercellular adhesions, and the modulation of cortex contractility drives the shape changes underlying cell division. In summary, the architecture and composition of the cortex give rise to very

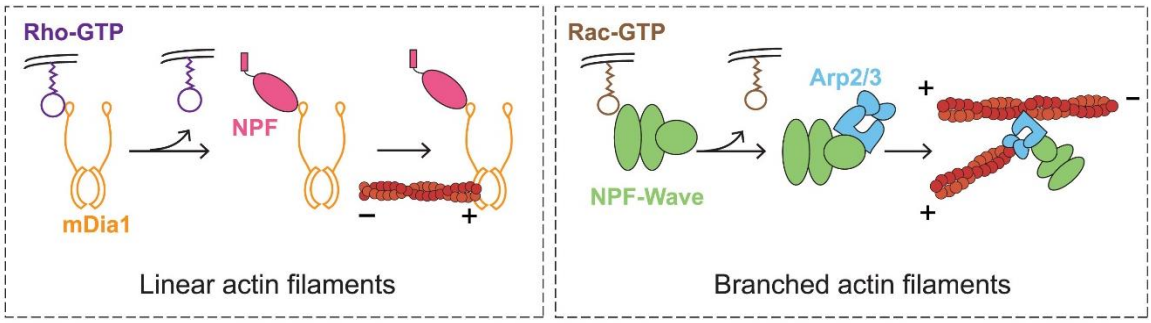

***Figure 2: Actin nucleation**. Linear actin nucleation occurs by direct activation of formins by RhoA-GTP. Branched networks are nucleated by the Arp2/3 complex, which is indirectly activated by Rac1-GTP via the Wave complex. Nucleation can be further regulated by nucleation promoting factors (NPFs). From ref.*21.

interesting mechanical properties that contribute to the versatility of cells (see Section 1.1.2 for more information on mechanical properties).

1.1.1.2 Cell-matrix adhesions

Epithelia have little extracellular matrix (ECM) and cell-matrix adhesions occur only between the basal side of the cell and the **basement membrane**. This membrane is a very thin (40-120 nm) and flexible matrix formed by glycoproteins (laminin, type IV collagen, fibronectin…) and proteoglycans[13]. It acts as a connection between the epithelial tissue and the underlying connective tissue, thus having an essential role in tissue architecture. It also determines cell polarity and promotes cell survival, proliferation, or migration.

These influences on cell behaviour are exerted through transmembrane cell adhesion proteins. These proteins act as receptors that tie the extracellular matrix to the cellular cytoskeleton. In animal cells, the principal receptors are **integrins**, which form heterodimers that are able to transmit signals in both directions across the cell membrane. To transmit these signals, integrins need to change their structural conformation. This can occur through either inside-out activation (biochemical interactions) or outside-in activation (extracellular force)[22].

Inside-out activation occurs when the adaptor protein talin binds an integrin, thus facilitating the binding of other intracellular proteins. Outside-in activation occurs when a ligand binds an integrin and force is applied. Both processes lead to the assembly of a macromolecular complex that contains proteins such as kindlin, vinculin and paxillin, and links to the actin cytoskeleton[23]. These cell-matrix junctions can be small and transient or form large and durable structures; an example of the latter are focal adhesions, that are dense plaques of integrin clusters that associate with stress fibers[24] (**Figure 3**).

The assembly of mature cell-ECM adhesion complexes allows cells to sense and respond to their microenvironment. Moreover, cell-ECM adhesions can convert mechanical signals into molecular ones and the other way around, thus being a key element for mechanotransduction[22].

1.1.1.3 Intercellular adhesions

Epithelial cells present different types of intercellular adhesions with different morphologies and that carry out different functions. In the case of simple epithelia, cell polarization produces a distinct distribution of each type of junction along the lateral surfaces of the membrane. The most apical ones are tight junctions, that hold the cells closely together, sealing the gap between them and preventing leakage across the epithelium. Below them, there are two types of anchoring junctions that link the cytoskeletons of neighboring cells: **adherens junctions** (AJs) anchor actin filaments, while **desmosomes** (placed further below) anchor intermediate filaments. Together, these three types of adhesions form what is known as the junctional complex[25]. Near the basal end of the membrane, we find gap junctions, that

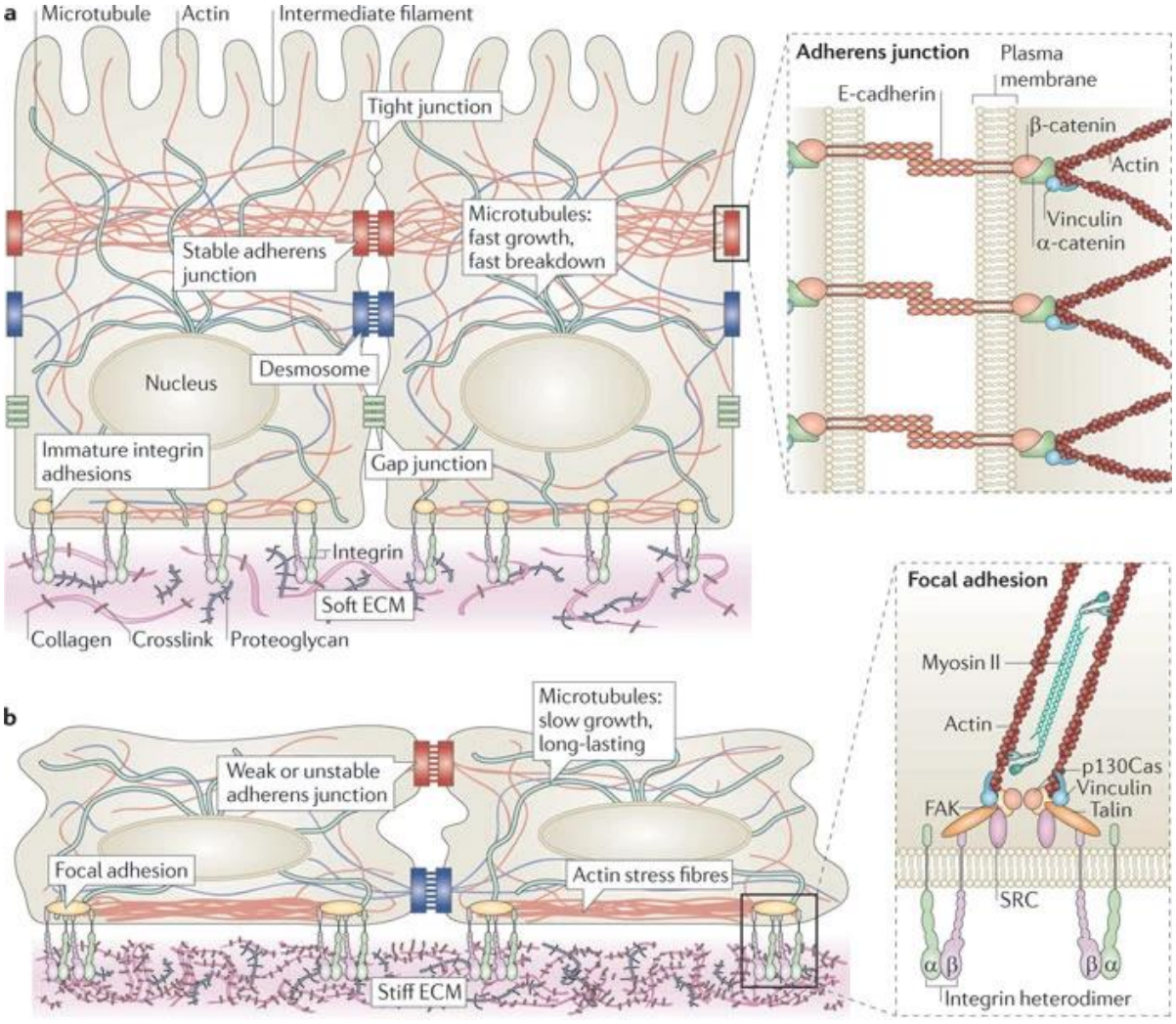

***Figure 3: Mechanical organization of epithelia**. Scheme showing the interconnected networks of the cytoskeleton, intercellular adhesions and cell-matrix adhesions. Intercellular adhesions couple the cytoskeleton of adjacent cells, allowing a collective mechanical behaviour of the epithelium. The physical properties of the ECM also affect the cytoskeleton: (a) a soft ECM leads to immature integrin adhesions, while (b) a stiff ECM promotes the assembly of strong complexes (focal adhesions) that lead to the formation of actin stress fibres. Image from ref.[24].*

are channels linking the cytoplasm of two adjacent cells and allowing the passage of small water-soluble molecules[12] (**Figure 3**).

For the purpose of this thesis, we will only discuss in depth anchoring junctions. The main mechanical function of both types of anchoring junctions is resisting external forces that pull the cells apart, while being dynamic and responsive to rearrangements when the tissue is being remodeled or repaired.

On the one hand, adherens junctions employ proteins of the **cadherin** family, which are dependent on Ca^{+2}, to link the cytoskeleton between the cells. These cadherins have transmembrane domains that associate with the analogous cadherin domains in the adjacent cell. Meanwhile, the cadherin cytoplasmatic domains link to members of the *armadillo* family, a family of proteins sharing a central domain with a series of amino acid repeats, that act as a platform where cytoskeletal adaptors bind. In these junctions, the binding with actin is mediated by α- and β-catenin. β-catenin binds the intracellular tail of cadherin and recruits α -catenin. Many actin-binding proteins present interactions with α-catenin, which suggests that its interaction with actin may be indirect. The application of force promotes the recruitment of other proteins that form a macromolecular complex which increases the stability of the adhesions[26].

On the other hand, desmosomes emerged in vertebrates and use updated versions of cadherins and armadillo proteins with respect to AJs. As we mentioned before, desmosomes bind IFs, which present different mechanical properties than actin, therefore playing a different role in the cell[27]. In the next section, we will explain how the properties of the different components of the cytoskeleton, as well as the adhesions, integrate to give rise to the mechanical properties of epithelia.

1.1.2 Mechanical properties and modelling of cells

Normal tissue development requires that cells in different microenvironments differentiate and acquire specialized phenotypes to carry out their specific functions. This specialization occurs also in the mechanical properties of tissues; in fact, these mechanical properties are key for the correct development of cell function in many cell types. A very clear example is

that of leucocytes, that need to undergo large deformations to extravasate and reach the damaged tissue[28].

When we want to quantify the mechanical properties of cells, we speak about **rheology**, that is the branch of physics that studies the deformation and flow of materials, both liquids and solids. The mechanical behaviour of materials can be studied by applying a defined stress, a force per unit area, and measuring the resulting strain (a relative deformation), or vice versa, by measuring the necessary stress to achieve a certain strain. We can measure the mechanical properties of cells using a wide variety of methods, each one with its advantages and limitations[29]. For example, atomic force microscopy offers high spatial resolution and a wide force range, but it is a low throughput method; on the contrary, optical tweezers measurements have a good throughput, but they have a narrower force range.

As mentioned previously, the cell cortex is the main contributor to cellular surface tension, thus being responsible for most of the mechanical properties measured by rheological techniques. Depending on the timescales analysed, that can range between milliseconds and hours, the cortex presents different mechanical behaviours[30]. Furthermore, different measurement techniques study different aspects of cell rheology. Integration of all these different data into a model of cell mechanics is not an easy work and it requires a proper combination of elasticity and fluid mechanics.

1.1.2.1 Viscoelasticity

Solid and liquid (fluid) materials behave differently when a force is applied. **Elasticity** is the tendency of solid materials to resist deformation when a force is applied and to return to its original shape and size when the force is removed[31]. It can be quantified with the Young modulus: materials with large Young moduli are difficult to deform, like iron, while ones with low Young moduli are elastic, like rubber. Conversely, fluid materials tend to flow in response to force application. However, not all fluids flow in the same way, some fluids resist motion, such as honey, while others flow easily, like water. This resistance to flow is termed **viscosity**[31].

Materials that present elastic behaviour do not dissipate energy when a force is applied. They store it by increasing their internal stress and, once the force is removed, they return to their initial state. On the contrary, materials with viscous behaviour flow, thus dissipating the

applied force, and deform in an irreversible way. Cells show both elastic properties, resembling those of a solid, and viscous properties, like those of fluids. Therefore, to study the response of cells and living tissues to external forces and deformations, we need models that account for the elastic and viscous components; such models are called **viscoelastic models**[32].

In these models, viscoelastic materials are traditionally described by mechanical equivalent circuits of connected springs, representing the elastic components, and dashpots, representing the viscous ones. The simplest models are the Maxwell and the Kelvin-Voigt models (**Figure 4**). They are linear models and, therefore, they describe systems where the relationship between stress and strain is linear at any given time. These two models can then be combined into more complex models with any number of components. In the case of cells, each one of these components can reflect the contribution of a different structural element, such as the cell membrane or the cortex. By adding more components, we can create sophisticated models that better reproduce the mechanical response of cells to numerous rheological techniques. However, precise characterization of cells using techniques such as magnetic tweezers or micropipette aspiration has revealed that the basic assumptions of linearity and decoupling of the viscous and elastic properties into different components are not correct[29]. If the external stress or strain we apply are small, the assumption of linearity holds, but properties such as stress-stiffening and fluidization confer nonlinear mechanical properties to the cell.

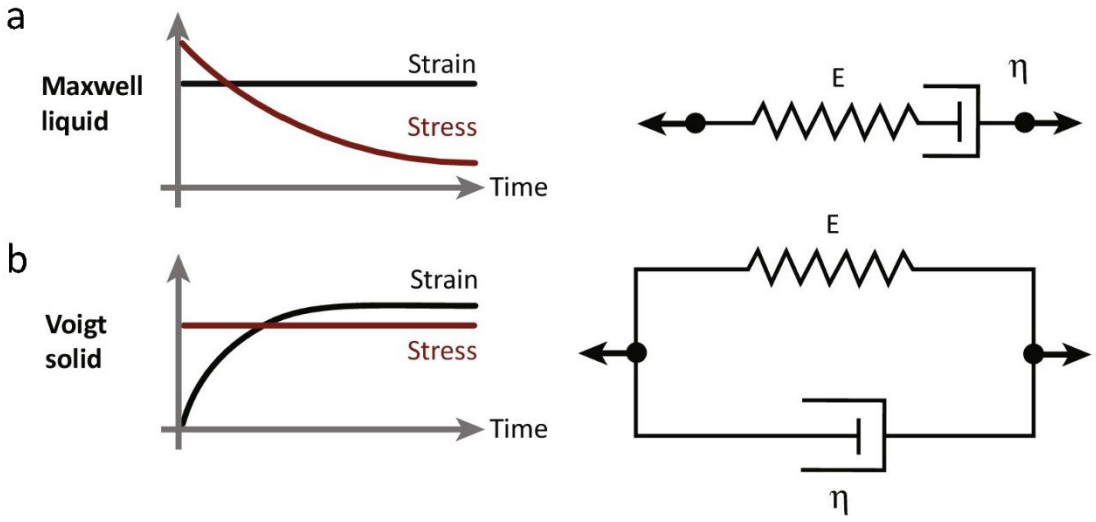

Figure 4: Basic rheological models. *a, Left: Stress behaviour of the Maxwell model at constant strain. Right: schematic of the model. b, Left: Strain behaviour of the Kelvin-Voigt model at constant stress. Right: schematic of the model. Adapted from ref.* 32.

Experiments with cytoskeletal networks generated *in vitro* show that these semi-flexible polymers often increase their Young modulus with increased strain, a phenomenon that is called **strain-stiffening**[33]. The strain-stiffening of these networks has important implications: their linear elastic modulus is orders of magnitude smaller than that of cells, but, when prestressed into the nonlinear regime, their modulus increases greatly and approaches that of cells[34]. These findings suggest that cells are always subject to an internal stress, or contractile prestress, that influences their mechanical response. Other experiments with fibroblasts also show that the elasticity of cells increases dramatically when they are stretched[35], further supporting the hypothesis of strain-stiffening. It is important to mention that not all reconstituted cytoskeletal networks display stiffening: weakly connected networks, such as pure microtubule networks or weakly cross-linked actin networks, present reversible stress-softening [36,37].

Another nonlinear phenomenon is **fluidization**, where the cell behaves in a more fluid-like fashion. This fluidization occurs both during stretch application and right after it, and is also dependent on prestress; stiff solid-like cells fluidize more during stretch than softer fluid-like ones[38].

1.1.2.2 Power-Law Rheology and Soft Glassy Materials

Since the viscoelastic response of cells is not linear, it is very difficult to model using only dashpots and springs. However, it can surprisingly be described by a power law with a single exponent over many orders of magnitude of time or frequency[29]. This power-law behaviour can be represented using a component called “springpot” that has an intermediate response between a spring and a dashpot. When subjected to constant stress, the strain of the material represented by the springpot follows the equation $strain(t) = t^{\beta}$, where β has a value between 0 and 1 (**Figure 5**a)[21]. It is important to note that β=0 would correspond to the behaviour of a spring and β=1 to that of a dashpot. This power-law rheology seems to be a universal property of adherent cells (**Figure 5**b) and holds even after treatment with a wide range of drugs that affect the cytoskeleton[38], such as cytochalasin D (that disrupts actin filaments). This behaviour can be explained by the theory of **soft glassy materials** (SGMs)[39].

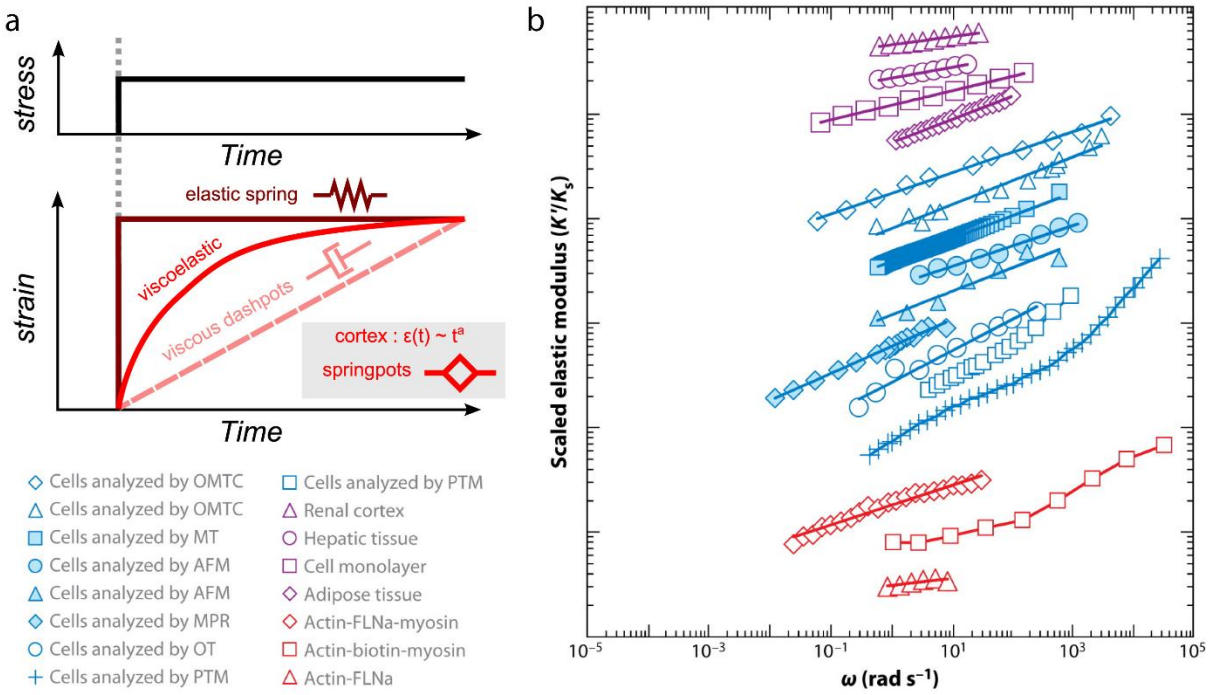

Figure 5: Power-law rheology of biological materials*. a, Strain response under constant stress of elastic, viscous, and viscoelastic materials following power-law rheology. Adapted from ref.* 21*. b, The response of cells (blue), tissues (purple) and cytoskeletal networks (red) to stress follows a power-law over many orders of magnitude of frequency . The absolute values of the differential elastic modulus K' measured at a fixed prestress vary according to specimen type and experimental technique and are difficult to compare between different studies. For clarity, the curves have been shifted in the y direction to emphasize the similarity of the frequency dependency. Abbreviations: AFM, atomic force microscopy; FLNa, filamin A; MPR, microplate rheometer; MT, magnetic tweezers; OMTC, optical magnetic twisting cytometry; OT, optical tweezers; PTM, particle tracking microrheology. Adapted from ref.*29*.*

SGMs are a diverse group of very soft materials with power-law exponents on the order of 0.1. This group includes foams, emulsions, and colloids. Since SGMs are so heterogeneous, their rheological properties must be a consequence of their structural organization, instead of a reflection of specific molecular mechanisms. SGMs are formed by elements aggregated to one another through weak interactions, and their structure is inherently disordered and metastable, which means that the state of the system is not the state of least energy[29]. This metastability means that each element of the matrix or network exists in an energy landscape with many wells (low energy states). For an SGM to deform elastically, its elements must remain in the energy wells, in other words, its deformation energy must be stored as internal stress. Conversely, for an SGM to flow, its elements must escape these wells, thus dissipating the stored deformation energy.

The actomyosin cortex satisfies all the criteria listed above and can be considered an SGM with a power-law exponent of about 0.2.[21] The difference between inert SGMs and the cortex is that the source of the effective temperature are myosin molecular motors that transform

chemical energy (ATP) into forces exerted on the actin filaments. This model also accounts for cell fluidization, since mechanical stretch provides energy that contributes to augment the effective temperature, thus increasing the probability of escaping the energy wells. However, it does not predict strain-stiffening[29].

1.1.2.3 Front-rear polarization and Active Gel Models

Another important property of cells is their intrinsic ability to establish front-rear polarization. In isolated cells on rigid extracellular matrices, the cytoskeleton and cell-ECM adhesions can spontaneously organize in an anisotropic manner even in the absence of external biochemical or mechanical cues[32]. This process can also be induced by external cues, like differential substrate adhesivity or anisotropies in substrate stiffness. Polarization requires cell contraction and proteins present on focal adhesions, such as talin[40] and α-actinin[41].

By increasing substrate stiffness, we can see a transition in the ordering of the actin cytoskeleton akin to those observed in passive materials such as liquid crystals. Liquid crystals are materials with mechanical properties resembling those of liquids, but whose molecular units are sufficiently ordered to give rise to some anisotropy; an example of this is an LCD screen (standing for Liquid Crystal Display), where the anisotropy affects the optical properties of the material. These liquid crystals may be rod-shaped molecules, similar to cytoskeleton filaments, that can transition from an isotropic disordered state to an ordered one in response to various stimuli (temperature, electric fields, density changes…). The ordered state can be a polar phase, where the molecules have distinct heads and tails and are on average oriented in the same direction, or a **nematic phase**, where the molecules can either be apolar or be aligned but with random head-tail orientations[32] (**Figure 6**). In the case of a cell, an example of a polar phase could be actin orientation in lamellipodia, while one of a nematic phase could be actin organization in stress fibres, where filaments are antiparallel.

This phase transition can be understood in the framework of the **active gel theory**. From a polymer physics perspective, the actin cytoskeleton can be considered as a gel, meaning a dilute cross-linked system, that exhibits no flow when in equilibrium[42]. *In vitro*, the actin gel is a very soft material, with Young's modulus of 0.1-1kPa[43]. After a mechanical perturbation, it presents an elastic response at short time scales and a viscous fluid-like response at time scales longer than the relaxation time, when actin starts to flow (about 100-1000s); this

behaviour is similar to the mentioned Maxwell model. However, it is important to remember that the actin cytoskeleton is not a passive gel; it is an active material where ATP is hydrolized to fuel both myosin motor activity and treadmilling, and, therefore, it is out of equilibrium. The active gel theory combines the properties of passive fluid-like materials in motion (hydrodynamics) with an active stress that reflects the forces and contractility generated by the actomyosin network. Therefore, it explains the short-time elastic behaviour and the long-time active liquid crystal behaviour of the cytoskeleton[20].

A model of the actomyosin gel can be obtained by simplifying the molecular complexity of the cytoskeleton and writing equations to describe the system at the mesoscopic or macroscopic scale using continuous variables such as density, velocities, and the orientation field of the filaments. The global stress within the gel in the long-time scale (σ) has two tensorial components, σ^p is the passive contribution, a purely hydrodynamic term, and σ^a is the active part (Equation 1)[32]. The active part is in turn composed of two terms that describe the isotropic component of the stress, independent of filament orientation, and the nematic component, which increases with filament alignment (Equation 2)[32].

$$\sigma_{ij} = \sigma_{ij}^{p} + \sigma_{ij}^{a} \quad (1)$$

$$\sigma_{ij}^{a} = \xi \delta_{ij} + \xi' Q_{ij} \quad (2)$$

The parameters ξ and ξ' depend on motor and filament densities and vanish when the system is in equilibrium (there is no ATP hydrolysis). If $\xi < 0$, the system tends to contract spontaneously; if $\xi > 0$, the system tends to expand. Similarly, for $\xi' < 0$ the system contracts and for $\xi' > 0$ the system expands, but it does so according to the nematic order parameter Q_{ij}. In the case of actomyosin gels, the system is known to be contractile (ξ, $\xi' < 0$).

Active gel models have proven useful to describe many cellular processes (**Figure 6**). A remarkable example is the emergence of actin retrograde flows that are required for lamellipodium motion[44]; in this case, actin flows from the lamellipodium to the back of the cell, pulling the cell body. These models can also describe the properties and behaviour of the actomyosin cortex. It is important to note that there is not a perfect model of the cell that can account for all its mechanical properties; however, efforts in modelling are providing an increasingly better understanding of the mechanical behaviour of cells.

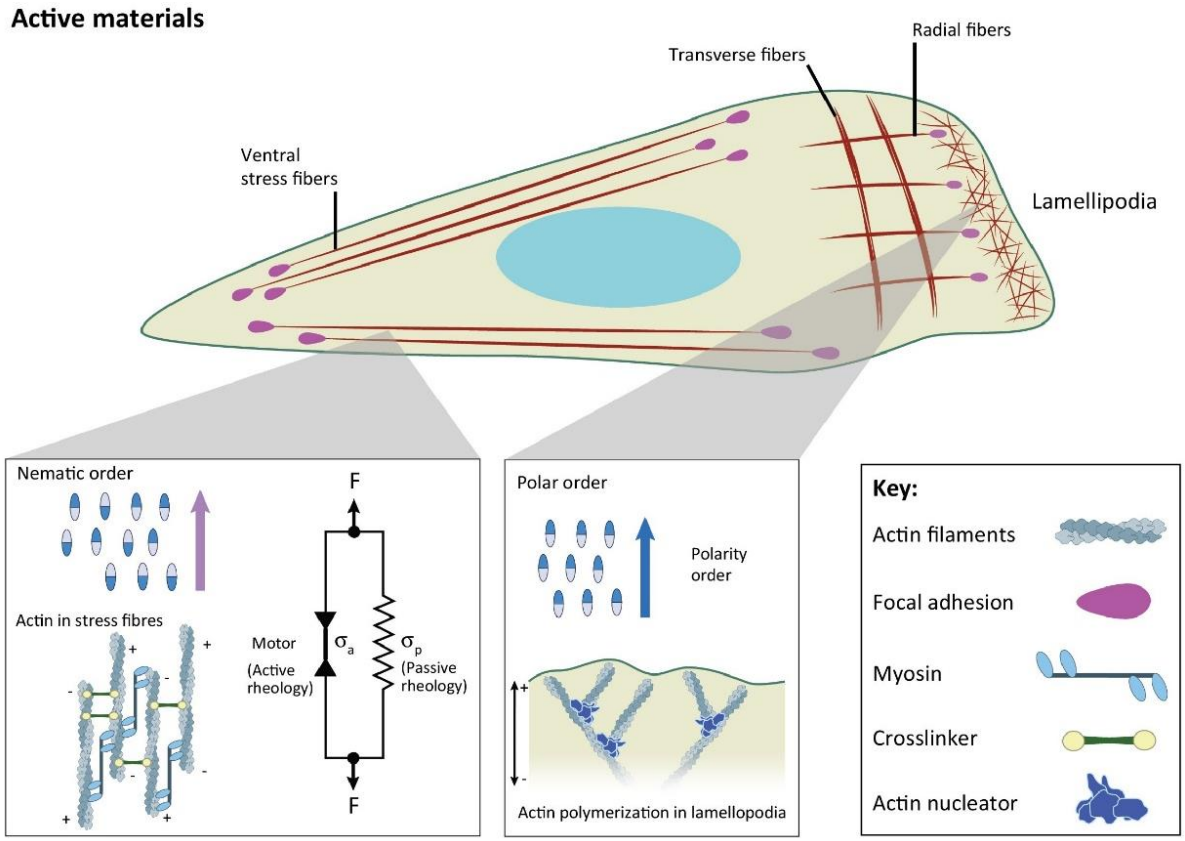

Figure 6: Actin architecture in a migrating cell. *Stress fibres present an antiparallel filament organization (nematic order). Lamellipodia present a rearward flow of branched actin filaments (polar order). Adapted from ref.*32.

1.1.3 Mechanical properties and modelling of epithelia

The behaviour of epithelia is as closely related to the mechanical properties of the tissue as cell behaviour is linked to the properties of the cytoskeleton. In a similar manner to individual cells, epithelial monolayers also present viscoelastic behaviour. A clear example is morphogenesis, a process where cells must sort and flow like a liquid to organize themselves into tissues, and then stiffen and support mechanical stresses once the tissue is formed[45]. The change from a viscous behaviour to an elastic solid-like one can be achieved by a relatively small change in the mechanical parameters of the tissue. These parameters can be intercellular interactions, mediated by cadherins, or interactions between the cells and the extracellular matrix[46,47]. However, cells are not passive elements, and the internal activity of each cell affects the large-scale behaviour of the tissue. That is, the coupling of cells with their environment is affected by intracellular contractility and other properties of the cytoskeleton

and cell adhesions, which are in turn actively remodelled by the environment, creating a complex feedback loop.

1.1.3.1 Tissue-scale models of epithelia

Theoretical models of multicellular processes can be classified in two categories[48]. The first category comprises continuum models, which describe the cell sheet as a fluid or elastic continuum; some examples are phase field models and the previously mentioned active gel models. Unlike cellular active gel models, the elements of tissue-scale active gel models are cells instead of filaments, but the same generic equations can be applied due to the similarity of their properties. Cells can also be described as nematic or polar elements, and tissue dynamics are also governed by the viscoelastic properties of the material and active stresses (largely generated by the actomyosin system)[20].

The second category comprises mesoscale models, that incorporate some minimal characteristics of individual cells, like contractility, and examine how intercellular interactions and coupling to the environment determine mechanical properties at the tissue scale. Some examples are vertex models (that we will explain in the next Subsection 1.1.3.2) and Voronoi models. Both models capture the behaviour of confluent tissues and describe cells as irregular polygons that tend to adjust their area and perimeter to minimize an energy function.

It is important to note that continuum and mesoscale models do not try to accurately incorporate intracellular processes. They aim to characterize the modes of organization and the mechanical properties of epithelial monolayers in terms of a few macroscopic parameters, like cell density, cell-cell adhesiveness, or contractility[48]. This approach attempts to provide experimentalists with predictions that may help to correlate families of signalling pathways to tissue organization.

1.1.3.2 Two-dimensional vertex models of epithelial tissues

In two-dimensional vertex models, each cell is represented as a polygon with edges shared between adjacent cells. These models present a set of rules that define the movement of each vertex based on location, connection between vertices and geometrical features, like volume of neighbouring cells[49]. These models were first applied to the study of inorganic structures, such as bubbles and foams, and they can be applied to epithelial tissues due to their resemblance to this kind of structures. To study epithelia, we need to incorporate

components describing the active properties of the material, like cell contractility and rules for neighbour exchange.

Each vertex in a vertex model is subjected to equations that govern its movement; these equations can either be written as forces explicitly applied on the vertices or as the result of an energy minimization function. A simple two-dimensional example using the energy-based approach for a cell "i" can be seen in Equation 3 ([50]):

$$E_i = \beta_i(A_i - A_0)^2 + \xi_i P_i^2 + \gamma_i P_i \quad (3)$$

The first term refers to the resistance to height fluctuations in the monolayer; each cell has a preferred area, A_0, which in this case is equal for all the cells. Deviations from this value imply a spring-like penalty defined by the parameter β. The second term refers to active contractility of the actomyosin cortex, which is proportional to the perimeter squared (P^2). Finally, the last term reflects the competition between cortical tension and cell-cell adhesion. γ can be positive if cortical tension is greater, or negative if adhesion dominates. Depending on the process being modelled, additional rules can be added to the model to better reproduce the behaviour of the tissue. For example, in confluent homeostatic tissues we may add T1 transitions, that are cell rearrangements where an edge between two cells shrinks and a new edge arises between two neighbouring cells. If we are modelling a growing tissue, we should also incorporate cell division and cell growth into our model[49].

In the case of confluent monolayers, vertex models suggest that as cell-cell adhesion increases toward a critical value, cortical tension suddenly drops. This critical value marks what is called a **jamming transition**, where cells switch from a solid-like configuration (jammed state) to a liquid-like one (unjammed)[50]. This transition is consistent with the change in behaviour that has been observed in tissues that remain at constant density, such as the airway epithelium in asthma (**Figure 7**). Homeostatic tissues, where cells are quiescent and rarely change neighbours, experience a change in behaviour where cells start to migrate in a collective fashion and form packs and swirls[51]. Cell morphology also presents changes, with cells transitioning from a close-to-regular hexagonal grid to more elongated and diverse shapes. The ability of vertex models to capture these behavioural changes makes them a great tool to study morphogenesis. However, most morphogenetic processes involve three-dimensional

conformations of tissues; for this reason, researchers are increasingly developing 3D vertex models.

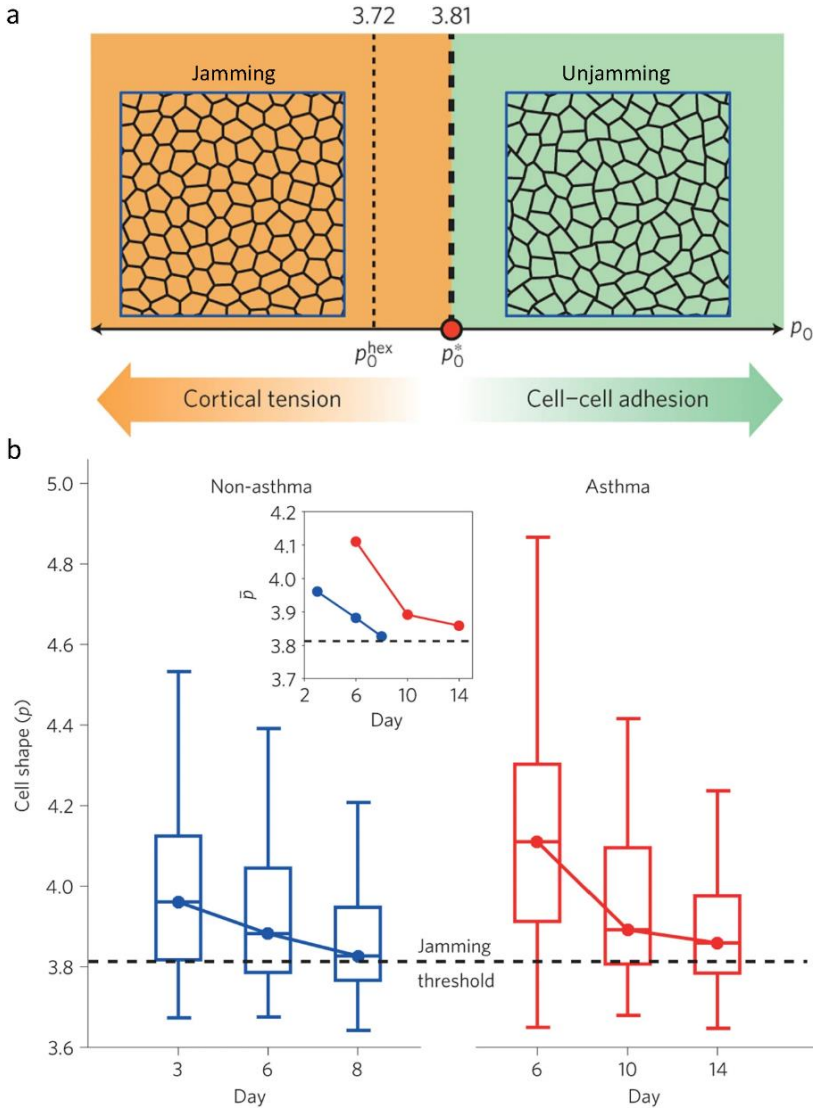

Figure 7: Jamming transitions in asthma. *a, Vertex model simulations of jammed and unjammed epithelia. There is a transition in epithelial behaviour when the shape parameter, p_0, is equal to p_0^*. p_0 is computed as P/VA, where P is the perimeter and A is the area of each cell. p_0^{hex} indicates the value of a regular hexagon. Adapted from ref.*50. *b, Cell shape parameter of HBECs from a non-asthmatic and an asthmatic donor over maturation in culture. Over time, and in both cases, $\bar{p}$ systematically approached the jamming threshold p_0^*, but the approach was considerably delayed in the samples from the asthmatic donor. Inset: $\bar{p}$ for representative non-asthmatic and asthmatic donors plotted with the same axis of culture days to allow comparison of the jamming transition timing. Boxplot shows median and quartiles. Whiskers are maximum and minimum data points. Adapted from ref.* 52.

1.1.3.3 Three-dimensional vertex models of epithelial tissues

In three-dimensional vertex models, cells are represented by polyhedrons, and the dynamics of the epithelia are described by the forces that act in the vertices of these polyhedrons (like in the two-dimensional case). The cells display the apicobasal polarity characteristic of epithelial cells, with adhesion to the substrate defining the basal side and a contractile actomyosin belt on the apical side. Thus, the equation describing the energy-based approach for a cell "i" has some differences with respect to the 2D case (Equation 4)[53]:

$$E_i = \beta_i(V_i - V_0)^2 + \Lambda_a P_{apical,i} + \alpha_{l,i} A_{lat,i} + \gamma_i A_{basal,i} \quad (4)$$

In this case, instead of assuming that the cell has a preferred area, we assume it has a preferential volume, V_i. The second term, that refers to active contractility of the cell, is associated with the apical perimeter, $P_{apical,i}$, due to the location of the actomyosin belt. The third term, that refers to the competition between cortical tension and adhesion, is proportional to the lateral area of the cell, $A_{lat,i}$, and α_l can be either negative (adhesion dominates) or positive (tension dominates). Finally, a new term describing cell-substrate adhesion has been added; this term depends on the basal area of the cell, $A_{basal,i}$.

Changing the parameters of this model allows us to explore many shape transitions and curvature generation processes that can be seen *in vivo*. By changing the adhesion and contractility parameters, we can model the transition between a squamous epithelium and a columnar one (**Figure 8**a,b). Since basal tension and apical belt tension are applied in different

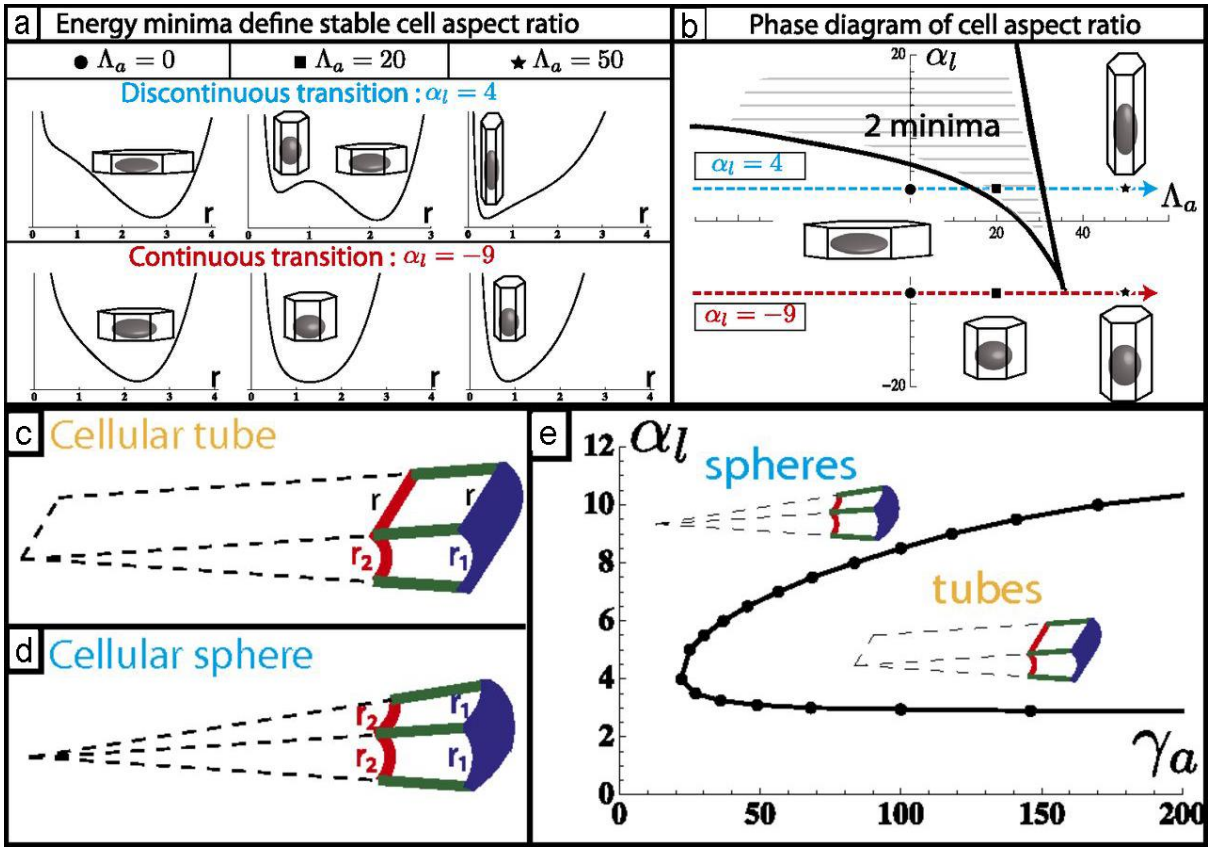

Figure 8: Epithelial cell shape and curvature in 3D vertex models. *a, Cell aspect ratio as a function of cell base length, r, when apical belt tension Λ_a is increased. If contractile forces dominate α_l, the system presents two energy minima and cells "jump" from squamous to columnar aspect ratios (top row). If adhesion dominates, the system presents only one minimum and there is a continuous transition from squamous to cuboidal to columnar aspect ratios (bottom row). b, Phase diagram of cell aspect ratio as a function of Λ_a and α_l, for $\gamma = -15$, showing regions of continuous and discontinuous transitions. c-d, Comparison of the mechanical stability for cellular tubes, made of cells curved in one direction (c), and cellular spheres, curved in two directions (d). e, Stability diagram as a function of lateral adhesion, α_l, and apical tension γ_a. Adapted from ref.* 53.

locations, differential values will lead to bending of the epithelial sheet (if substrate deformation is allowed); a larger apical tension will produce negative curvatures (invaginations), and a larger basal tension, positive ones (evaginations). Furthermore, we can modify the parameters anisotropically through the tissue or change their contribution according to direction, and thus create non-spherical geometries, such as tubes[53](**Figure 8**c-e).

Depending on the modelled epithelia, we can also change the energy equation to better describe the properties of the tissue and its environment. For example, MDCK cells are known to present a uniform thin actin layer lining the lateral surfaces instead of an apical belt; therefore, we should substitute the term describing the apical belt with a term of active surface tensions along lateral cell faces. These models can also be used to model lumen formation or epithelia that surround lumens; in these cases, the basal adhesion term can be eliminated or modified depending on the conformation of the system[54].

1.2 Epithelial Morphogenesis and Growth

The generation of shape in multicellular organisms, also known as morphogenesis, is frequently driven by the deformation of epithelial tissues[55]. This can be easily understood if we examine the distribution of epithelia in the human body. These tissues form the surfaces that separate the body from the external milieu, such as the skin, the gastrointestinal tract, or the interior of the lungs. A specialized type of epithelium, the endothelium, constitutes the inner surface of both blood and lymphatic vessels. Furthermore, the mesothelium, another type of epithelia, forms the pleura and the peritoneum, the membranes that line the thoracic and abdominal cavities, respectively. Briefly, they delimitate the different compartments in the organism, and changes in their shape result in changes in the underlying compartments.

Another process that has great relevance in development is that of tissue growth. Growth and morphogenesis occur concomitantly during most of embryogenesis, from the blastula stage to organogenesis, and they are strongly related. Growth can generate asymmetries in the embryo that lead to changes in shape, and shape must be resilient to changes in the size of tissues. Developing tissues present many strategies that allow them to maintain this balance between shape and size and give rise to adult organs[56,57]. In all these strategies, changes in

mechanical properties of different system components play a key role, like contractility of individual cells, fluid accumulation or generation of in-plane stresses.

In the next subsections we will describe some methods for inducing curvature changes and elongating tissues, as well as the formation of different types of lumens.

1.2.1 Tissue folding

Epithelial cells present a clear apicobasal polarity and form cohesive sheets where the actomyosin cytoskeleton of one cell is strongly connected to that of its neighbours through adherent junctions. These junctions allow force transmission between cells, thus permitting coordinated movement and rearrangement of cells, that can give rise to complex changes in tissue shape. Some examples of these processes are bending and buckling of epithelia.

1.2.1.1 Apical constriction

Apical constriction is defined by a shrinkage of the apical side of a cell and it is driven by the contraction of F-actin networks due to the action of myosin. Many cell types exhibit an actomyosin belt that exerts forces on the apical perimeter through adherens junctions, while others tend to accumulate actomyosin in the medioapical domain[58] (**Figure 9**a). This process is facilitated by the action of RhoA (and other proteins of the Rho family, **Figure 9**b) and **Shroom**, which is an actin-binding protein that is localized at apical junctions. Shroom is both necessary and sufficient for apical constriction in vertebrates[59].

During shrinkage of the apical domain, actomyosin flows towards the centre of the apical cell cortex. These flows do not occur in a continuous manner, but as pulses caused by assembly and disassembly of F-actin with myosin[60]. It is interesting to note that these pulses occur during a wide variety of cell shape changes and, even though their function is not yet fully understood, evidence suggests that they contribute to maintain tissue integrity during contractile processes.

Apical constriction is a key mechanism in many developmental processes, and it is conserved in many different organisms. A clear example is gastrulation, where it leads to inward folding of the blastula (made up of one layer) to generate the different germ layers; apical constriction is involved in this process in a variety of organisms as disparate as the sea urchin

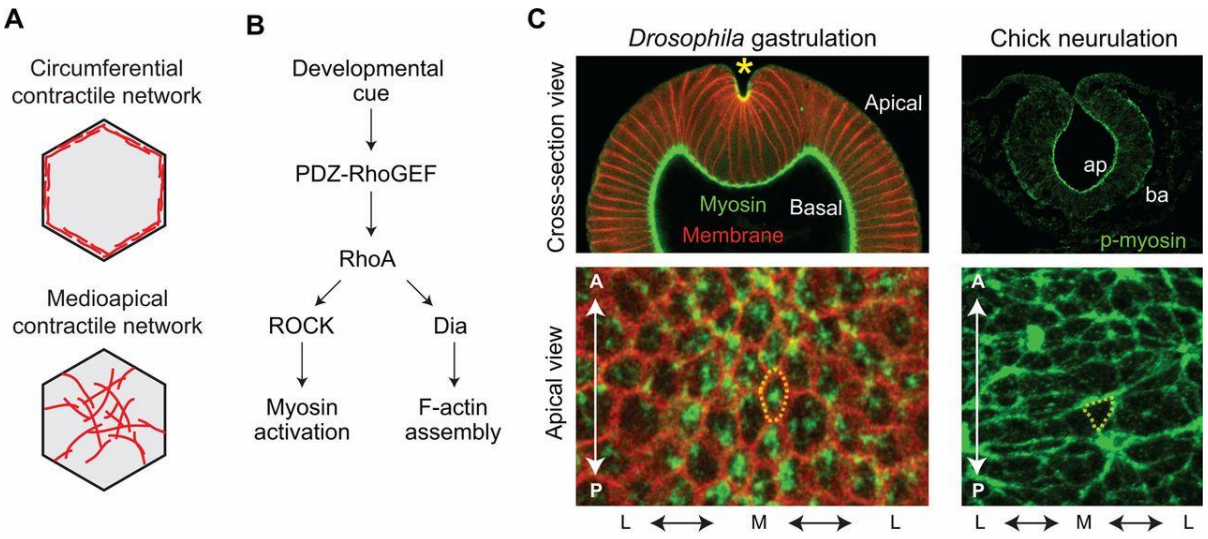

Figure 9: Variations in the spatial localization of actomyosin during apical constriction. *a, Schematic of circumferential actin-myosin networks and medioapical actin-myosin networks (both illustrated in red). b, A conserved pathway, involving PDZ-RhoGEF, RhoA, ROCK and Dia, regulates myosin activation and F-actin assembly in* Drosophila *mesoderm cells (medioapical networks) and the chicken neural tube (circumferential networks). c, Cross-section views (top) and apical surface views (bottom) of* Drosophila *mesoderm cells during gastrulation (left) and of the chick neural tube (right). Myosin (green) is preferentially in the medioapical region in the* Drosophila *mesoderm precursor cells, but it is preferentially circumferential during chick neurulation. Asterisk marks the site of invagination, where mesoderm precursor cells are undergoing apical constriction. Axes are also marked: apical-basal (ap-ba), medial-lateral (M-L) and anterior-posterior (A-P). From ref.* 58.

and *Xenopus*[61]. In individual cells, it can lead to cell ingression from the epithelium, sometimes as part of an epithelial-mesenchymal transition. This is the case of the mouse embryo, where this process leads to ingression of mesenchyme cells into the primitive streak[62] (a structure that establishes bilateral symmetry and starts germ layer formation). Apical constriction of individual cells can also participate in cell extrusion of apoptotic cells, thus helping to regulate tissue growth and maintain tissue homeostasis.

Bending of epithelial tissues can occur when cells retain intercellular adhesions while undergoing apical constriction, thus generating **invaginations** or **tubes**. In the *Drosophila* gastrula, cells located at the ventral midline constrict apically resulting in a wedge shape that helps move the ventral furrow beneath the epidermis; this creates a tube of mesoderm[63]. In vertebrates, apical constriction of cells retaining adhesions is involved in the formation of the neural tube, the precursor of the central nervous system, from the neuroepithelium[64] (**Figure 9**c).

1.2.1.2 Tissue buckling

Apical constriction involves the active generation of mechanical forces by the cells undergoing the morphogenetic event. However, passive forces that arise from mechanical instabilities

between the epithelia and their surroundings can also lead to folding and shaping of the embryo. This is the case of buckling, a process where in-plane compression of the tissue results in out-of-plane folding[65].

Buckling has been extensively studied in inert materials, particularly in thin elastic beams with compressive force applied at their two ends. As a response to the compression, the beam deforms with a characteristic curvature that depends on the applied force and the physical properties of the beam (length, thickness, Young modulus…), thus relaxing the in-plain strains. Buckling is also relevant in the context of thin films floating on liquids or soft elastic materials, where uniaxial compression generates parallel wrinkles or undulations on the film that are perpendicular to the direction of the forces[66]. It is important to keep in mind that compression does not need to be applied externally to produce buckling, it can be caused by non-uniform growth of the film or by growth under confinement[67,68]. Epithelial tissues are formed by very thin sheets, with a height on the order of 10 μm, that can nonetheless extend up to meters in width and length. In gastrulation, they are usually adhered to the mesenchyme, which later in embryogenesis differentiates into other tissues that line epithelia, such as connective tissue and smooth muscle. Therefore, due to the geometry and boundary conditions of epithelia, they are very susceptible to the same instabilities that lead to buckling in non-living materials.

In epithelial tissues, buckling usually arises from inhomogeneous growth within a single layer or from different growth rates on adjacent cell layers. An example combining both approaches could be the cerebral cortex, where recent studies suggest that folding is driven by differential growth between various layers of the brain and regions of the cortex. Subcortical layers present slower growth and restrict cortical expansion, thus putting the cortex in a compressive state and causing it to buckle[69]. Additionally, neuronal progenitors divide at higher rates in the regions that will become gyri (cortical ridges) than in those that will become sulci (depressions)[70].

Another remarkable example is the formation of intestinal villi. In the chick embryo, the gut is initially formed by an epithelium surrounded by a mesenchymal layer, and its luminal surface is smooth. In this case, the differentiation of a part of this mesenchyme into three subsequent layers of smooth muscle is sufficient to induce the different stages of villus formation[71]. Smooth muscle presents higher stiffness than the epithelium and, therefore, it

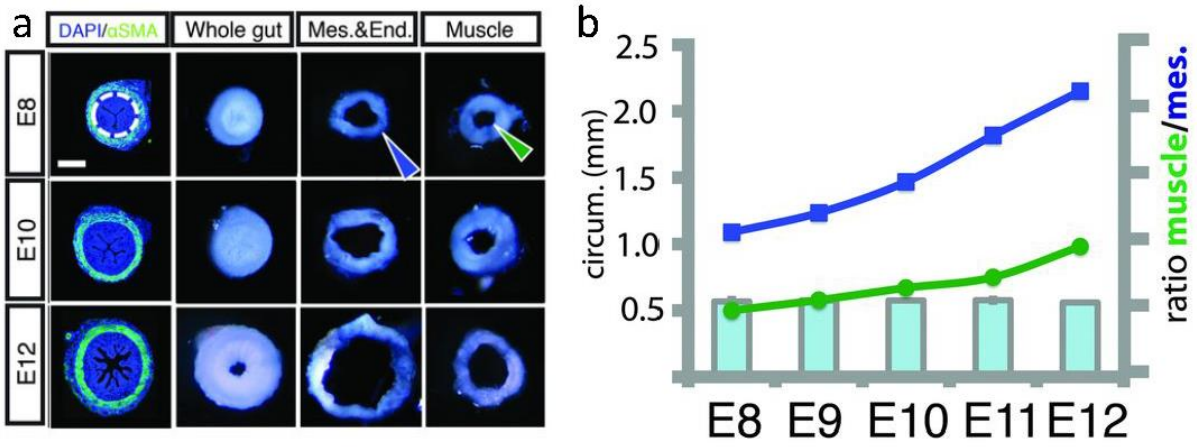

***Figure 10: Chick gut morphogenesis**. a, Transverse slices of developing chick guts immunostained for nuclei (DAPI, blue) and smooth muscle actin (αSMA, green) at developmental stages E8, E10 and E12. Whole guts (left) are surgically separated along the junction between the mesenchyme and the smooth muscle (dashed line). Upon separation, the luminal ridges in the mesenchyme and the attached endoderm unfold and expand (middle), while the smooth muscle remains unchanged (right). The outer circumference of the mesenchyme (blue arrowhead) is larger than the inner circumference of the smooth muscle (green arrowhead). b, Inner circumference of the smooth muscle (green line) compared with outer circumference of the separated mesenchyme-endoderm (blue line) over time, along with the compression ratio (bar graph). Scale bar: 100 µm. Adapted from ref.* 71.

can direct morphogenesis by constraining epithelial tissues (**Figure 10**). Another useful property of smooth muscle in this context is its anisotropy; it forms fibres that tend to orient in one direction. Thus, the different fibre directions of the three smooth muscle layers lead to the sequential formation of ridges, zigzags and, finally, the villi[71].

1.2.2 Tissue growth and rearrangement

Tissue growth is a necessary process by which multicellular organisms increase their size. In animals, this process occurs during embryonic development (concomitantly with tissue buckling and bending), as well as during post-natal growth and wound healing (maintaining organ shape). Separately, tissue rearrangement is a process of structural reorganization of the tissue. This rearrangement involves coordinated changes of cell shape and reorganization of cell-cell contacts, and it modifies tissue geometry[72]. During development, changes in size and shape are coordinated to give raise to the adult tissues and organs. In this context, isotropic growth leads to an increase in size, without altering the shape of tissues and organs. Conversely, anisotropic growth or rearrangements can lead to changes in the geometry, thus playing an active role in morphogenesis.

In animal epithelial tissues, the direction of growth is influenced by planar cell polarity (PCP), which consists on the polarization of epithelia within the plane of the cell sheet. PCP implies

the establishing of molecular asymmetries that include cytoskeleton reorganization and junction composition, and it arises from tissue wide cues. Usually, we associate these cues with biochemical signals, such as Wnt gradients in the wing of *D. melanogaster*[57]. However, mechanical cues such as tissue stresses and fluid flows can also induce the creation of PCP patterns or change their orientation[73]. Therefore, the magnitude and direction of these mechanical stimuli can affect growth rate and lead to either isotropic or anisotropic growth. In this subsection, I will describe two main mechanisms of tissue growth in morphogenesis, that are related to PCP and mechanical cues: cell intercalation and cell division.

1.2.2.1 Cell intercalation

Cell intercalation is a process that allows cell rearrangement by changing the position of intercellular junctions in the tissue. Initially, junctions are removed, bringing four or more cells together at one vertex. These high-order vertices are transient and disappear when new junctions, orthogonal to the original ones, are formed. When only four cells are involved in this process, it is called a T1 transition[74]. When five or more cells share a vertex, these transient structures are called rosettes and their formation can involve a T2 transition (cell extrusion)[75].

Intercalation is an irreversible process that can be directed by the polarity of the epithelium (PCP). The polarity is imposed by the direction of the stresses transmitted across intercellular junctions: the set of junctions that is removed depends on its orientation relative to these stresses, leading to asymmetric tissue extension. In fact, cell intercalation is a driving force in a process called **convergent extension** (**Figure 11**). This process leads to tissue extension along the anteroposterior axis and narrowing (convergence) along the dorsal-ventral axis in the embryos of many organisms[61].

Remarkably, junctions do not passively respond to the forces in the tissue: they actively remodel cell-cell contacts and allow the dissipation of the tissue stresses on long time scales, conferring fluid properties to the cell sheet. This junction remodelling can be driven by either global or local cues[74]. One the one hand, it can be driven by external constraints acting on the epithelium, like hinge contraction causing rearrangement on the pupal wing in *Drosophila*[76]. On the other hand, there are systems where PCP allows cells to locally produce the energy needed to rearrange by forming planar-polarized supracellular cables of actomyosin, such is

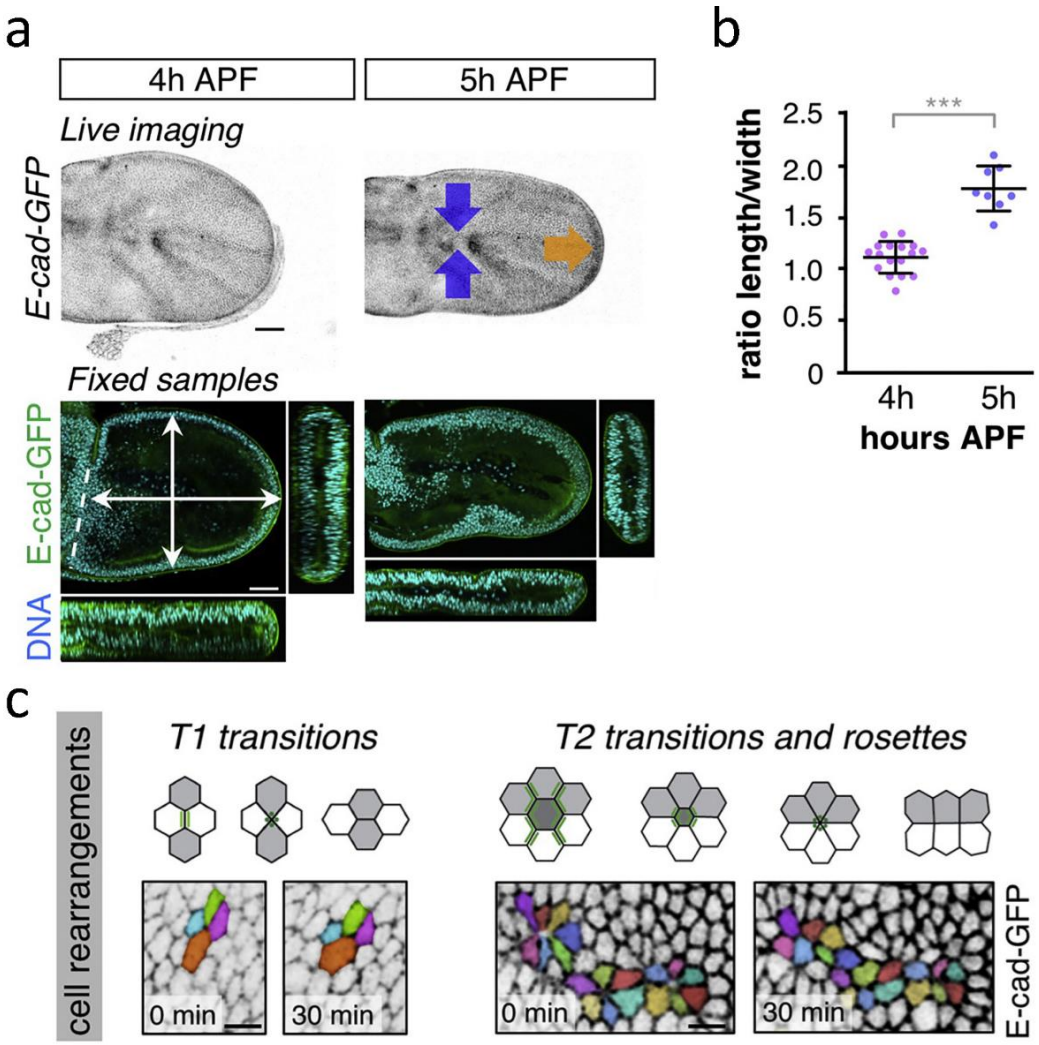

Figure 11: Convergent extension in the* Drosophila *pupal wing*. a, E-cad-GFP live imaging (top) and fixed imaging (bottom) of developing wings at 4 and 5 hr after pupa formation (APF). From 4 to 5 hr APF, the wing contracts along the anterior-posterior axis (blue arrows) and elongates along the proximal-distal axis (orange arrow), which is consistent with convergent extension. Scale bar: 50 µm. b, Quantification of the length-to-width ratio of fixed samples at 4 and 5hr APF, showing an increase in wing anisotropy. c, E-cad-GFP live imaging during convergent extension. Time is measured from 4h APF. Cell tracking (coloured cells) shows how the epithelia contract along the anterior-posterior axis by cell rearrangements (T1 transitions, T2 transitions and rosettes) and cell shape changes. Scale bar: 10 µm. Adapted from ref.*75.

the case of the chick neural tube[77]. Defects on the establishment of PCP can lead to failure of convergent extension in the neural tube of animals and result in neural tube defects, which are a common birth defect in humans[78].

1.2.2.2 Cell division

In contrast to cell intercalation, which leads to tissue remodelling through reorganization of the existing cells, cell division affects tissue shape and size by addition of new cells. In epithelia, cell division is tightly regulated in both time and space, because it must balance growth and morphogenesis in developing organisms, and homeostasis in adult ones. In

addition to sensing stress patterns in the tissue, proliferation also affects this force distribution, thus creating a mechanical feedback loop between orientation of cell divisions and tissue stress[79].

When cellular density is high, the compressive stresses generated by the cytoskeleton and transduced by cadherin-mediated intercellular junctions lead to suppression of cell division (and increase of cell extrusion) and, in turn, to a decrease in overall tissue stress. Conversely, at low cellular densities, tensile stresses lead to an increase in cell division rate and, consequently, of tissue stress. Cell division also affects the rheology of a tissue, "solidifying" it by increasing cell density, and fluidizing it through mitotic rounding (which causes a drop in viscosity due to a reduction of intercellular contacts)[80]. Differential rates of cell proliferation in a tissue can determine its stress distribution and orient tissue growth, as seen in the *Drosophila* wing imaginal disc[81]. Additionally, differential division rates across adjacent tissues also have an important impact on morphogenesis and can lead to the formation of 3D structures from 2D tissues (as previously explained in Subsection 1.2.1.2).

The orientation of cell division is controlled by the mitotic spindle orientation, a microtubule structure that separates sister chromatids to each daughter cell. The first experiments on division orientation in single cells were carried out at the end of the XIXth century, when

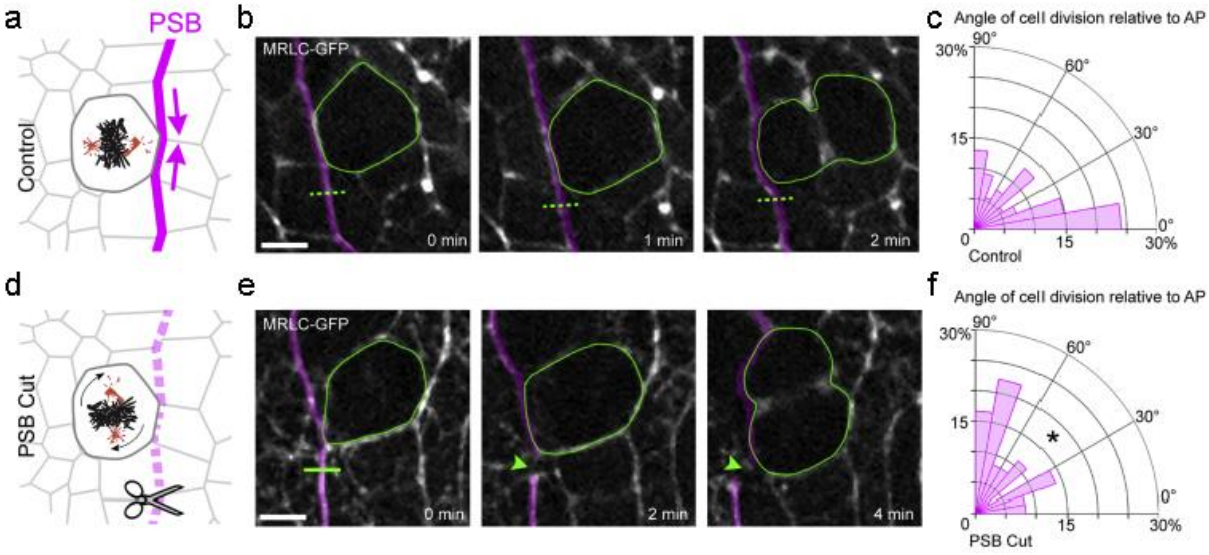

***Figure 12: Actomyosin cable tension orients division of cells at the parasegmental boundary (PSB) in* Drosophila**. *a,d, To impair tension locally, the actomyosin cable is illuminated with control low-intensity laser light (a) or cut (d) next to a mitotic cell in metaphase. b,e, Fluorescent images of myosin regulatory light chain (MRLC-GFP) following cell division during a loss of PSB tension experiment (e) and its control (b). The dotted line indicates the region of illumination (b). The small solid green line shows the laser cut and the arrowheads highlight cable recoil (e). Scale bar: 5 µm. c,f, Cell division angles relative to the antero-posterior axis for the control (c) and laser cut (f) experiments. Adapted from ref.* 82.

Hertwig flattened amphibian eggs and observed that the first cleavage was perpendicular to the long axis of the cell[83]. From then onwards, the long axis of the cell was used as a predictor of spindle orientation; this criterion was named "Hertwig's rule". However, recent findings suggest that Hertwig's rule only works in very anisotropic cells[82]. When the anisotropy is moderate, the mitotic spindle and cell division orient according to different parameters depending on the maturity of the epithelium.

In mature epithelia, the best predictor for spindle orientation is tricellular junctions, which accumulate proteins that regulate cortical attachment of spindle microtubules and are aligned with the principal axis of local stress[84] (**Figure 12**). In immature epithelia or epithelia where regulators of the orientation of cell division do not localize at tricellular junctions (like MDCK monolayers), division aligns with global tissue stress[85]. This orientation of cell division relative to global or local stress allows stress dissipation within the tissue and facilitates tissue expansion, as shown by experiments with MDCK cells and gastrulating zebrafish[86,87].

1.2.3 Intercellular fluid and lumenogenesis

In addition to the mechanical properties of the tissue, there is another physical component that plays a key role in morphogenesis and shape maintenance: **intercellular fluid**. Tissues are immersed in fluid, whose composition, volume and movement are controlled by compartments such as lumens, organs and vessels[88]. Due to the incompressible nature of liquids, these fluids generate considerable hydrostatic pressure that can act both at a local level, affecting the surrounding tissue, and at great distances, thus affecting organs or even the whole organism[89]. The isotropic stress exerted by this pressure can change tissue geometry and lead to a build-up of supracellular tension, which can in turn modify cell behaviour or alter cell fate[90].

1.2.3.1 Fluid regulation and ionic pumps

In order to control fluid transport and secretion, epithelial cells rely on osmotic gradients. One of the main proteins involved in the formation of these gradients is the **Na^+/K^+-ATPase**, also known as sodium-potassium pump. This pump creates sodium and potassium gradients across the plasma membrane that are used to facilitate the transport of molecules, such as sugars or neurotransmitters, and other ions. The subcellular localisation of the Na^+/K^+-

ATPases is key for several physiological processes (**Figure 13**). It depends on the isoform of the different units that compose the pump, which vary according to organ and cell type[91,92]. The neuroepithelium that lines the brain ventricles sorts this pump to the apical membrane domain, which helps maintain a low potassium level while facilitating fluid secretion to the ventricular lumen[93]. Conversely, in the renal tubular system, this pump is expressed in the basolateral domain to minimize bodily loss of sodium through urine[94]. It has been found that this pump is necessary for the formation of lumens across many organisms. A remarkable example of this is blastocyst cavitation in mouse, rabbit and cow[95,96].

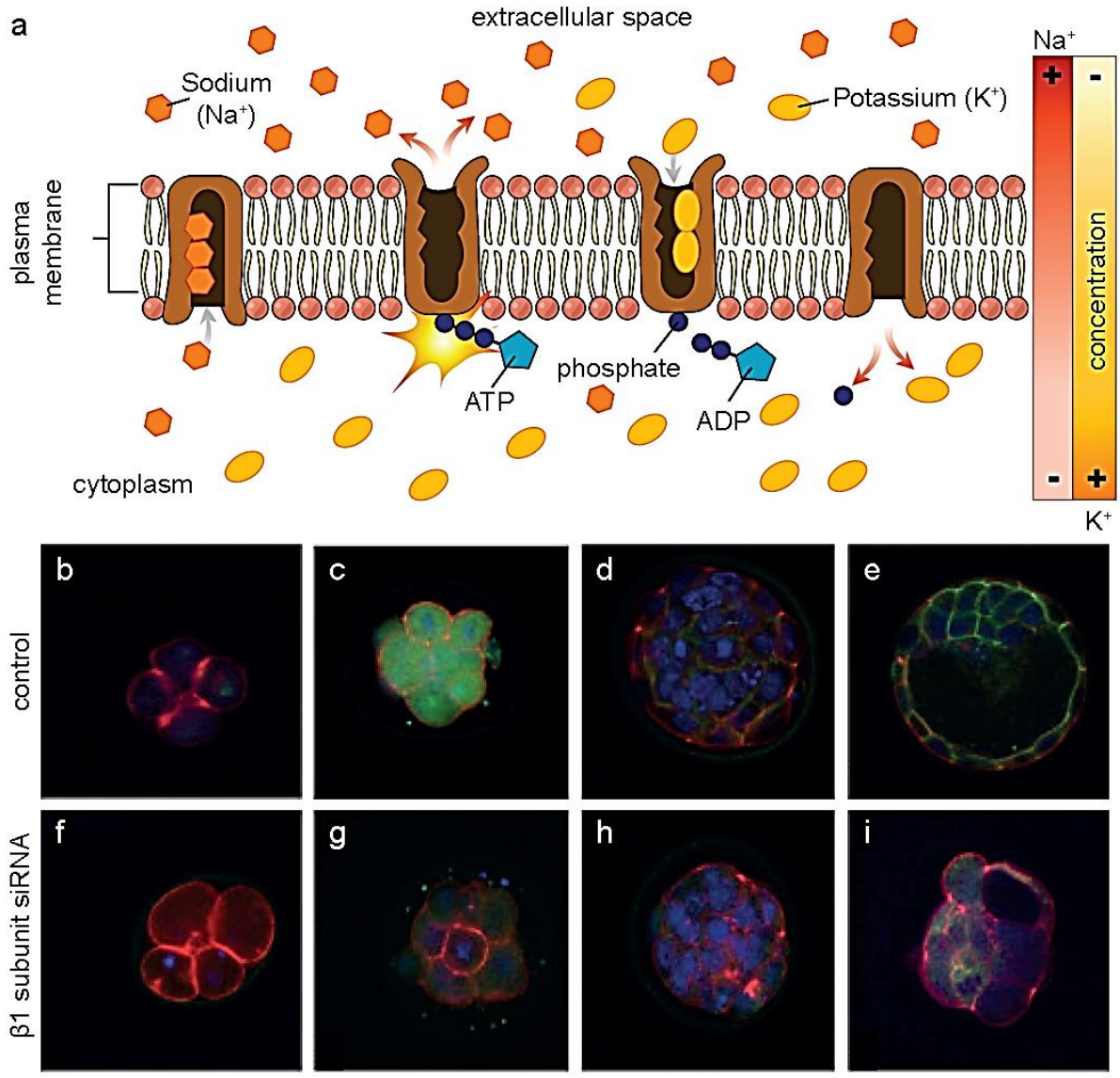

Figure 13: Function and location of sodium-potassium pumps in the early mouse embryo. *a) The sodium-potassium pump is a transmembrane protein powered by ATP. The pump moves sodium and potassium ions in opposite directions, each against its concentration gradient. In a single cycle of the pump, three sodium ions are extruded from the cell and two potassium ions are imported into the cell. Adapted from ref.*97*. b-e, Distribution of Na/K-ATPase β1 subunit during murine preimplantation development of a control embryo. f-i, Distribution of Na/K-ATPase β1 subunit of an embryo after microinjection of β1 siRNAs. Green, red, and blue colors in (b-i) indicate positive staining for the respective primary antibody, F-actin (rhodamine phalloidin), and nuclei (4,6-diamidino-2-phenylindole), respectively. Adapted from ref.*92*.*

The ion gradients generated by Na^+/K^+-ATPases drive chloride secretion into the luminal space through channels like **CFTR**[98]. The accumulation of chloride generated by CFTR leads to a luminal electrochemical gradient that favours the transport of water and sodium, and the consequent growth of the lumen. Fluid incorporation to the lumen is also dependent on tight junctions, mainly on proteins of the occludin and claudin families, that can form ion-selective pores that contribute to regulate fluid secretion[89].

The correct regulation of fluid secretion allows the formation and maintenance of the lumens that are present in almost all internal organs. Conversely, abnormalities in this regulation can lead to developmental defects[91]. Perhaps the clearest example of such a defect is the Kupffer vesicle in zebrafish, an organ transiently present in the embryo that controls left-right asymmetry; loss of CFTR function in the embryo impairs expansion of this organ, leading to loss of laterality in brain, heart and gut[99]. Deregulation of fluid secretion can also lead to disfunction in adult organisms; an example of this is polycystic kidney disease, where clusters of cysts develop and enlarge, eventually causing loss of kidney function[100].

1.2.3.2 Apical lumen formation and growth

The correct formation and maintenance of lumens is critical to help shape the embryo and to maintain proper organ function in adults. Therefore, understanding the mechanical and biochemical cues that regulate cell behaviour in luminal tissues is of utmost importance. Lumen formation can be initiated by many different processes. An example is apical constriction, that can lead to invagination of a cellular sheet and ultimately to tube formation, as is the case of chick neurulation[77]. In the early mammalian embryo (blastocyst), sorting of different cell populations contributes to formation of the lumen or blastocoel, through a process involving cadherin and actomyosin tension[101]. Other processes driving lumen shaping and formation are intercalation and convergent extension, and collective cell migration.

To start lumenogenesis, **apicobasal polarity** of the surrounding epithelia is required. Most lumens form on the apical side of cells and, therefore, apical and basal membranes are specialized into two distinct domains, where the apical surface responds to a fluid environment (either gaseous or aqueous) and the basolateral one is surrounded by cells or ECM. Initial fluid secretion and lumen opening require the transient assembly of polarity and trafficking machinery close to the apical membrane[102]. One of the proteins implicated in this

process is **podocalyxin**, a transmembrane glycoprotein with a large highly anionic extracellular domain with anti-adhesive properties; the localization of this protein to the apical membrane is necessary for renal tube formation and opening of vascular lumens in mice, and its knockout induces a lethal phenotype[103]. Podocalyxin is first localized at the membrane in contact with the ECM and requires internalization via Rab11a-positive vesicles, a type of vesicles regulated by a member of the small GTPase Rab family (which regulates membrane transport). Afterwards, vesicle transport to the apical surface is controlled by polarity regulators such as Cdc42 (a member of the Rho GTPase family). Cdc42 indirectly regulates both actin and microtubule cytoskeleton, thus linking cell polarization and lumenogenesis with cytoskeletal reorganization[102]. After acquiring the correct polarity, in vertebrates, epithelial cells drive lumen opening and expansion by liquid secretion. This process is permitted by the action of the Na+/K+-ATPase and CFTR channels, which generate ionic gradients that drive the secretion of fluid.

Lumens can present an infinity of different shapes, among which tubes are probably the most common ones. We can find organs formed by long unramified tubes, like the gut, and others that exhibit very complex branching, as the lung. However, independently of their final form, **tubulogenesis** presents two basic elements: the opening of the lumen requires filling (as mentioned above for any lumen) and mature tubes have a single lumen. Typically, one or multiple lumens form through cell rearrangements and establish a restricted space, then they expand due to liquid accumulation[89]. A critical step in tube formation is the resolution of a single lumen, that requires coordinated remodelling of the tissue and changes in the apicobasal polarity of cells. A dramatic example of this is anastomosis, or blood vessel fusion, in zebrafish (**Figure 14**). In anastomosis, two neighbouring tip cells guiding tube sprouts contact each other and form an apically polarized junctional ring, that encloses a luminal compartment. Then, cell rearrangements can bring two junctional rings together, merging the luminal compartments, displacing the middle cell to one side and, finally, forming a single tube[11].

Many lumenogenesis processes, including anastomosis, are highly affected by fluid pressure and flow. Pressure drives lumen expansion by stretching the cells surrounding the lumen, and, typically, favouring trafficking of new membrane to the apical surface and/or inducing proliferation[104]. However, sometimes the contractile state of the epithelium needs to be

modified to allow this deformation, as is the case of the neuroepithelium surrounding the brain ventricle in zebrafish, where epithelial relaxation through myosin regulation allows lumen growth[105]. Another example that emphasizes the role of contractility is the early

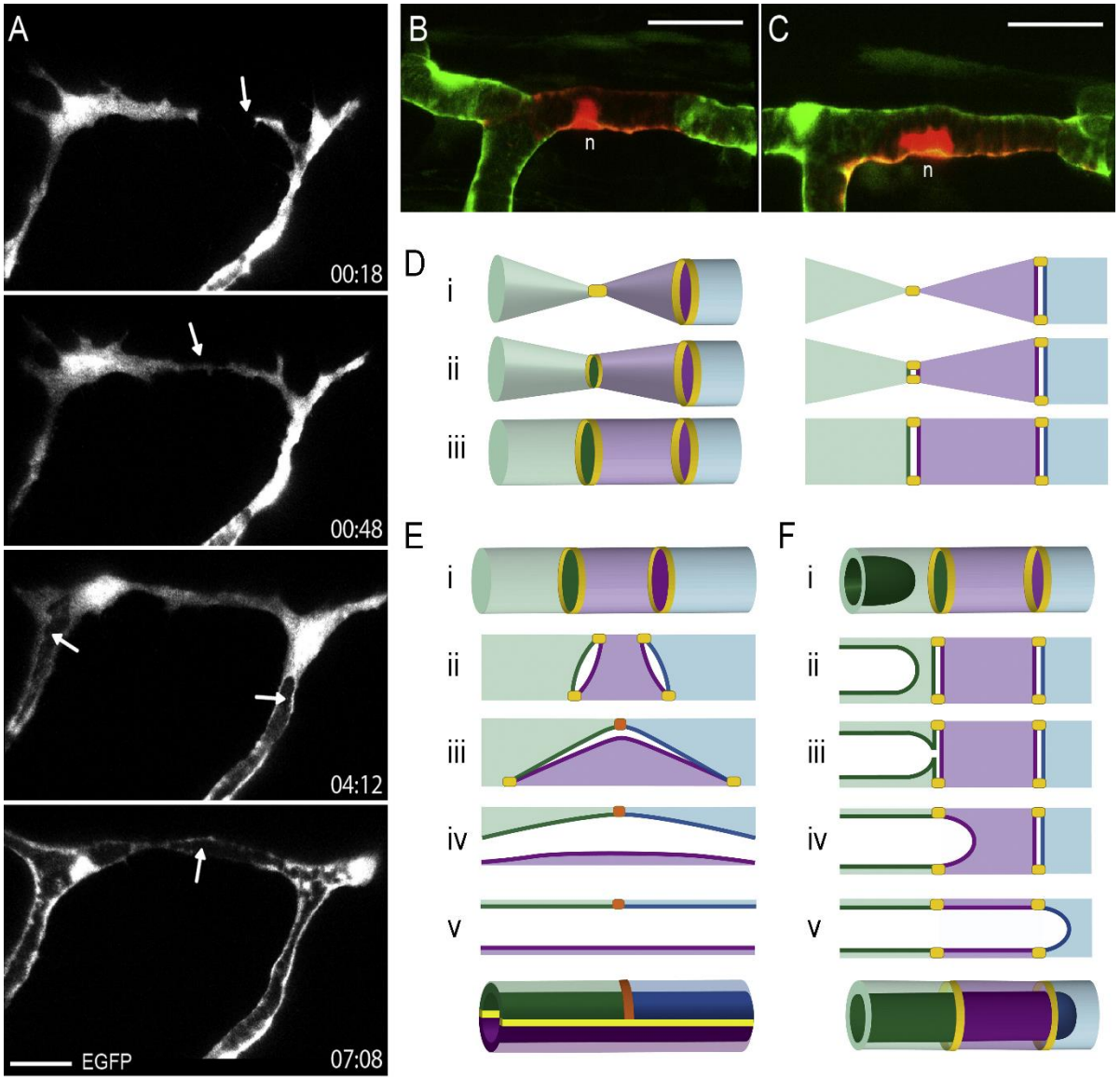

Figure 14: Anastomosis and heterogeneity of endothelial tubes. *a, Timelapse images showing steps during vessel anastomosis. Tip cells reach the dorsal side of the embryo and send filopodia in anterior and posterior directions (arrow in 00:18). The tip cells contact each other (arrow in 00:48) and the lumen opens from the stalk and proceeds into the contact region (arrows in 4:12 and 7:08). b,c, Different vessel architectures. Single photoconverted cells (red) show a unicellular (b) and a multicellular (c) tube section. n = nucleus. d, Schematic of contact formation during vessel fusion (left) and corresponding sagittal sections (right). At the contact site of two cells (green and purple), junctional proteins are deposited (yellow spot in i). Cells increase their mutual surface, the spot becomes a ring (ii, iii) and the enclosed membrane compartment becomes apically polarized (dark green and dark purple areas). Subsequently, two different cellular mechanisms can complete the fusion process (e and f). e, Schematic of the cord hollowing mechanism (results in a multicellular tube). Cell rearrangements bring together two apical membrane compartments that then merge into one membrane compartment. This is achieved by the formation of a new junction (orange) between the green and blue cell, which leads to the detachment of the middle cell (purple). f, Schematic of the cell membrane invagination mechanism (formation of a unicellular tube). The apical membrane of the green cell invaginates into the green cell. It then fuses with its own apical membrane at the previously formed contact side between the green and purple cells (see d). From here the apical membrane of the neighbouring cell (dark purple), begins to invaginate. Adapted from ref.*11.

development of the inner ear, where mitotic rounding leads to axis-specific lumen expansion and contributes to lumen anisotropy[6]. The geometry of lumens is also affected by contraction-generated flows (or more specifically, the shear stress they cause)[106]; this mechanical cue also plays a role in establishing left-right symmetry in many species[99,107].

1.2.3.3 Basal lumen formation and growth

Even though most lumens form on the apical side of epithelia, where the interface is more favourable due to a lower concentration of adhesion molecules, there are several examples of basolateral lumens. In fact, the cardiovascular system of most invertebrates is formed on the basal side of cells[108]. Another relevant basolateral lumen is the blastocoele in the early embryos of echinoderms, amphibians or mammals[88]. There are also examples of tumours that exhibit cysts with inverted polarity[109]. Additionally, MDCK cells, a canonical model for apical lumen formation, can also form cysts with a lumen on the basolateral side[110,111]. Therefore, basal lumens may not be such an uncommon occurrence in physiological and pathological settings.

The most studied occurrence of a basal lumen is the **blastocoel** in the mammalian blastocyst, an early developmental structure consisting of two groups of cells: the inner cell mass (ICM), consisting of the cells that will form the embryo, and an outer layer of cells called the trophoectoderm, that gives rise to the placenta. During the initial phase of the blastocoel formation, pressurized fluid is injected into the intercellular space due to an osmotic gradient (partially generated by Na^+/K^+-ATPases); the liquid is probably injected through a combination of vesicle release and paracellular transport via tight junctions[88].

At first, hundreds of micrometre-sized lumens form through the embryo due to **hydraulic fracturing** of cadherin cell-cell contacts[9]. The pressure inside of these small lumens is related to the tension and curvature of the enclosing membranes by the Young-Laplace equation. This equation, that will be explained further on Section 1.3.3, states that pressure is higher in smaller lumens if the enclosing membranes present the same tension, thus leading to small lumens discharging into larger ones. This process is similar to that occurring in foams, where big bubbles grow at the expense of smaller ones, thus increasing mean size and decreasing boundary surface in a process called **coarsening**. Coarsening leads to the resolution of a single lumen that becomes the blastocoel[9] (**Figure 15**). The final position of the blastocoel is

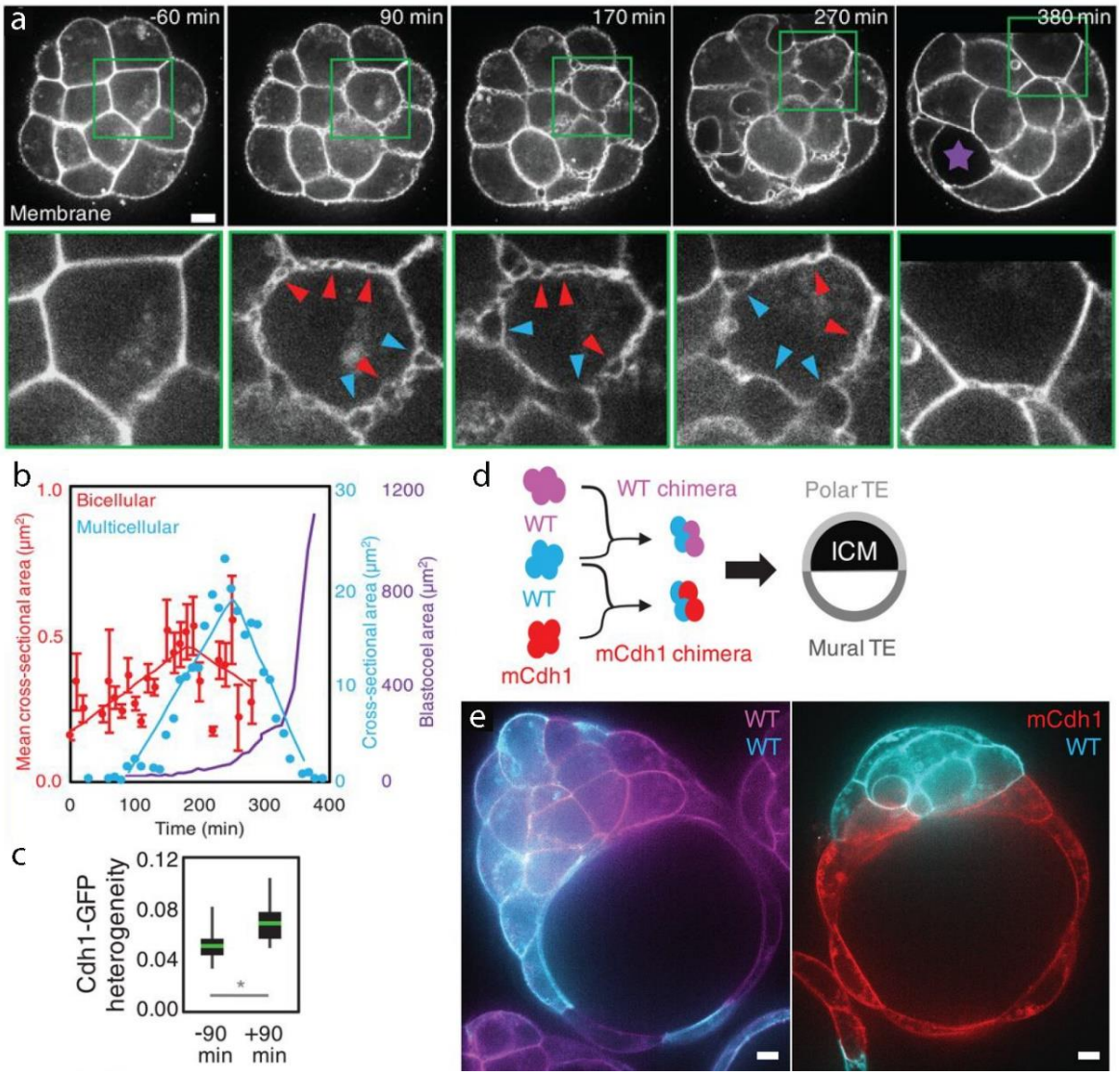

Figure 15: Lumen coarsening can be directed by cell adhesion. *a, Timelapse images of blastocoel formation. Microlumens form transiently at cell-cell contacts (red arrowheads) and multicellular junctions (blue arrowheads). They first swell and then shrink as the blastocoel (purple star) expands. The lower panels are 3x magnifications of the green squares. b, Growth dynamics of the blastocoel (purple), and microlumens at bicellular (red) and multicellular (blue) cell junctions. c, Coefficient of variation of cadherin1-GFP intensity along cell-cell contacts at –90 and +90 min compared to the time of microlumen appearance. d, Diagram of chimera experiments. Chimeric embryos were formed with two differently labelled WT embryos (control), and a WT and a mCdh1 embryo. WT, wild type. mCdh1, maternally knocked-out Cdh1. e, Chimeric control embryos composed of WT and WT cells, and experiment embryos with WT and mCdh1 cells. In the mCdh1 chimeras, the blastocoel formed preferentially on the mCdh1 half. Scale bars: 10 µm. Adapted from ref.*9.***Figure 15***

determined by the different contractility levels of the two cell types forming the blastocyst. Since cells from the ICM have higher surface tension, the lumen is located between these cells and the surrounding layer of trophoectoderm cells (instead of at the ICM-ICM interface)[112]. This combination of hydraulic fracturing of intercellular adhesions, coarsening, and differences in contractility observed in the blastocoel could be a general process explaining the formation and positioning of many lumens, both basolateral and apical ones.

1.2.3.4 MDCK basal lumens

As previously mentioned, Madin-Darby Canine Kidney cells (MDCK) can also form basolateral cysts, meaning that the lumen is in contact with the basal cell membrane. This occurs when the cells are cultured in suspension, with no matrix cues for polarity[110]. Within 24 hours, the initial single cell suspension gives raise to cell aggregates with a diameter of about 50 µm. These aggregates can be maintained in culture for more than a week and their size plateaus at around 90 µm-diameter. The apicobasal polarity of these cysts has been checked using antibodies for several proteins, including podocalyxin (a known apical marker) and Na+/K+-ATPase (which is expressed basolaterally in MDCK cells[94]). In contrast to apical lumens, podocalyxin was localized at the outer cell-free membrane and, after 5 days, Na+/K+-ATPase was localized at the luminal membrane (and at the membrane between adjacent cells)[113].

In this thesis, we have worked with a specific type of MDCK basal lumens commonly called **domes.** Domes were first described in 1969 by Leighton and colleagues[111]. After seeding

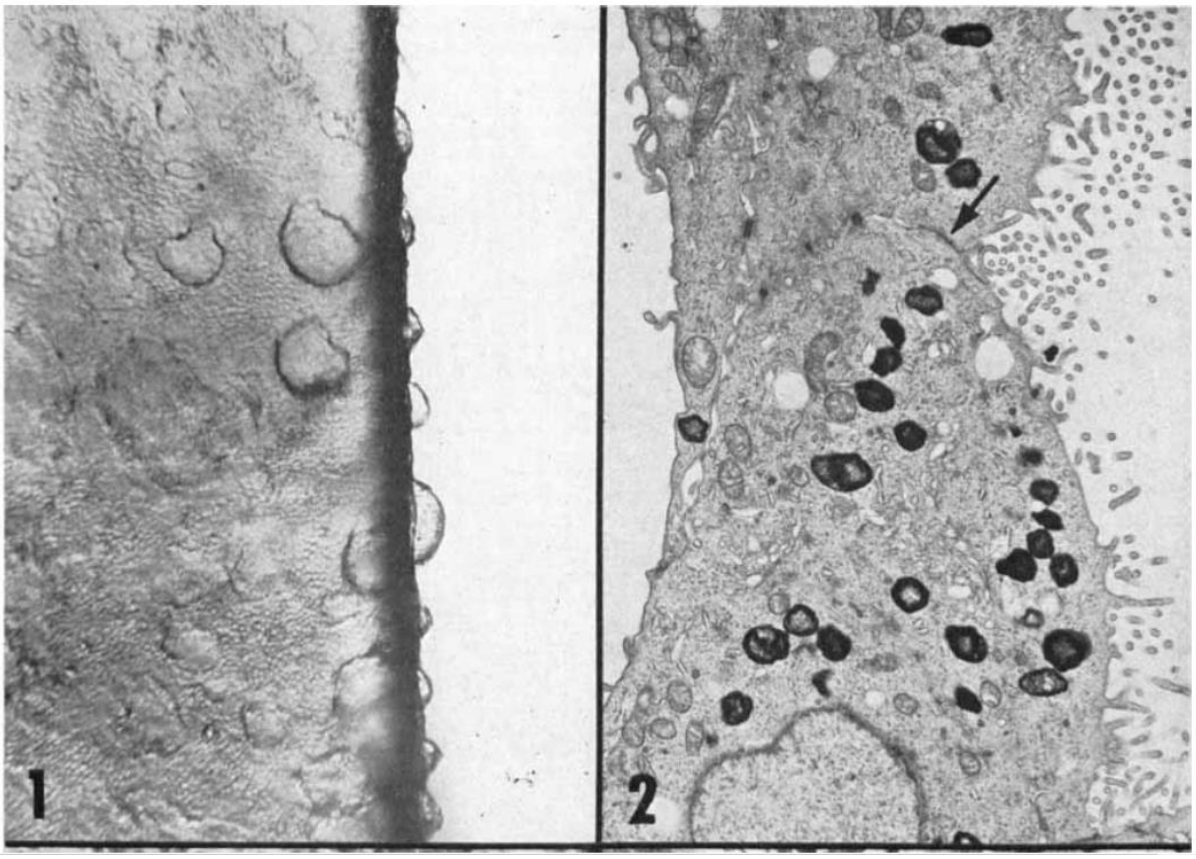

Figure 16: First images of MDCK domes. *(1) Culture of MDCK growing on the surface of a microscope slide. The slide is completely covered with a sheet of epithelium interspersed with Irregular, oval multicellular structures (domes). That these are vesicles is evident from the pattern of growth seen on the edge of the slide, where hemispherical blisters appear on profile. (2). Electron micrograph of a vesicle wall. The convex surface on the right (the outer surface of a blister) is covered with microvilli. A tight junction (arrow) joins 2 cell borders. From ref. 110.*

MDCK cells on glass slides and growing them to confluency, they observed the formation of lesions that they initially described as “ulcers”. Upon closer examination, they realised that the supposed lesions were in fact hemispherical vesicles or blisters composed of many cells. When they studied the morphology of the cells enclosing the lumen, they found clear markers of apical polarity (microvilli and tight junctions) in the outward facing membrane of the dome. This demonstrated that the apical surface of the cells was not facing the lumen, as happens in renal tubules, but the outer cell media [111] (**Figure 16**).

Domes are dynamic structures that can inflate, deflate, or even collapse abruptly (**Figure 17**a). Upon collapse, the monolayer is then repaired, and the inflation process is resumed. Domes are formed by fluid accumulation between the cellular membrane and the impermeable substrate. Leighton and colleagues also showed that this accumulation of fluid is associated with the function of the sodium-potassium ion pump (Na^+/K^+-ATPase), as indicated by the reduction of the number of domes after an overnight treatment with its inhibitor, ouabain[110].

In 1983, Tanner and colleagues observed that spontaneous domes not only present mostly circular bases, but their shape closely matches that of a spherical section (spherical cap)[114]. They then reasoned that, since domes are pressurized structures with a spherical cap morphology, the tension along the enclosing cell monolayer should be uniform and it can be computed using Laplace law (for more information, refer to Subsection 1.3.3). They made the first measurements of luminal pressure in domes, whose diameters spanned between 80 and 200 µm, and inferred a monolayer tension of around 25 mN/m.[114]Recently, Latorre *et al* performed new measurements of dome luminal pressure in a controlled set-up (possible thanks to three decades of technological advances)[54]. These new measurements gave pressure values around 1-3 mN/m (one tenth of the values estimated by Tanner *et al*.). Moreover, these experiments, that were carried out in domes with a radius of 100 µm (200 µm diameter) led to the discovery that the strain-stress relationship in domes was not trivial: they exhibited an **active superelastic** behaviour[54] (**Figure 17**b,c).

Superelasticity is a feature observed in some inert materials, such as nickel-titanium alloys. These alloys undergo large reversible deformations at nearly constant stress by means of a phase transformation that occurs heterogeneously through the material, giving raise to regions with high strain. In domes, superelasticity is an active process, achieved by progressive switching of individual cells from an unstretched to a super-stretched state (**Figure**

17d). This phase transition is caused by strain-induced cell softening, that occurs due to a limited availability of cytoskeletal components that results in cortical dilution (**Figure 17**e-g). This softening is combined with re-stiffening at extreme strains to confine the high-strain phase and allow the stabilization of super-stretched cells. This re-stiffening is prompted by the intermediate filament network[54].

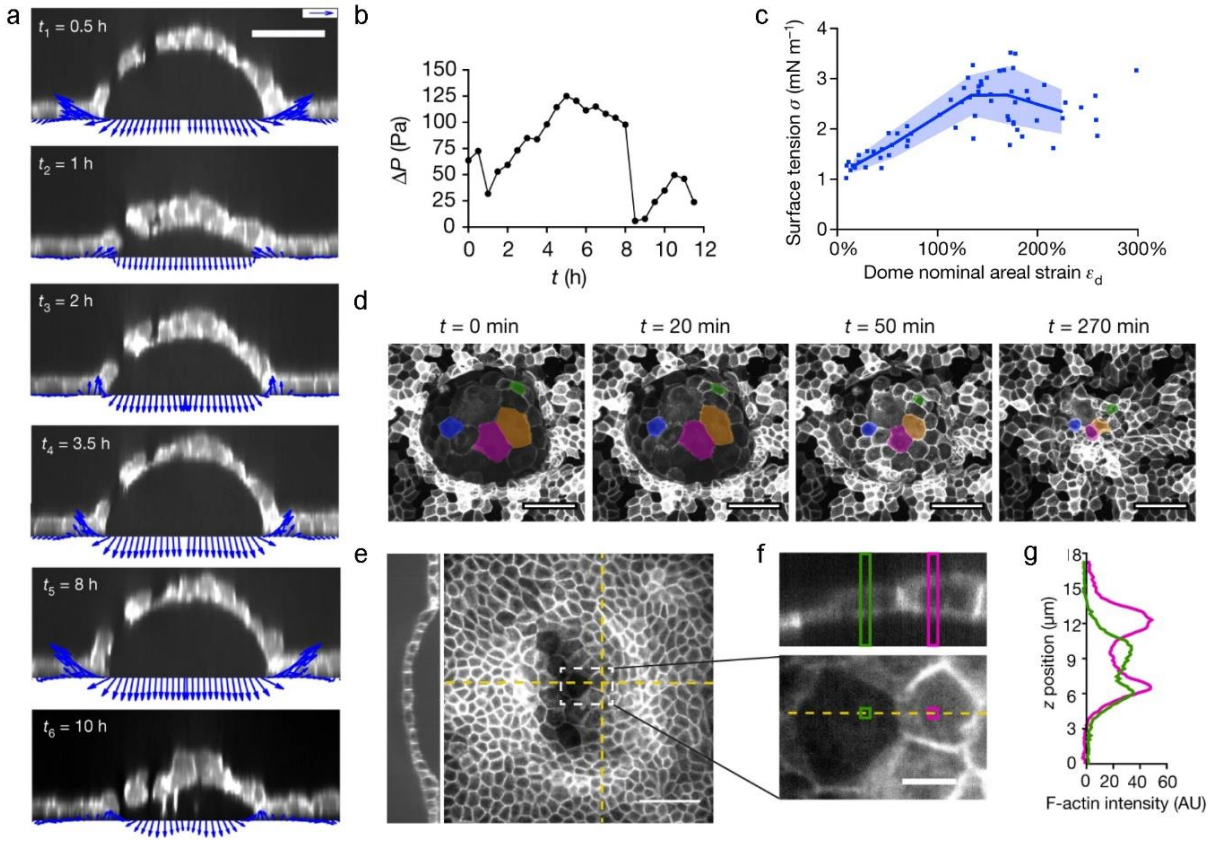

Figure 17: Superelasticity in MDCK domes*. a, Time evolution of MDCK domes and tractions (y-z section). b, Evolution of the luminal pressure of dome shown in (a). c, Surface tension in the free-standing sheet as a function of the dome areal strain (inflation level). d, Deflating MDCK dome with membrane marked (CAAX-GFP). Cells with different cellular areal strain are coloured. e, Sum-of-intensity projection and confocal section of a dome stained with phalloidin for F-actin. f, Zoom of representative cells. g, F-actin intensity along the bands marked in (f). AU, arbitrary units. Scale bar: 50 μm (a,d,e), 10 μm (f). Adapted from ref.*54.

1.2.3.5 Luminal size control

Vesicular tissues containing lumens of different sizes and shapes are present in many organs from very diverse species, including hearts, brains and guts. Since the acquisition of proper size is crucial for the healthy function of many organs, the existence of control mechanisms that ensure homeostasis is necessary. Although chemical signalling is known to play a role in this control, it is becoming increasingly clear that mechanical forces are also important at tissue and organ scales. The mechanical factors that have an impact can include cell proliferation, cell shape, material properties, or transepithelial transport. In the context of

luminal tissues, we need to underline the role of fluid accumulation. As mentioned in Subsection 1.2.3.2 ("Apical lumen formation and growth"), fluid accumulation can lead to lumen formation and expansion. Moreover, it can change the rate of luminal growth or even limit it[7].

Even though the ion transporters necessary for fluid accumulation have already been identified, many aspects of how they regulate fluid flow and their role in size control are only beginning to be unravelled. The main consequence of fluid accumulation is an increase of hydrostatic pressure that is applied on the surrounding tissues, leading to changes in cell shape and behaviour. The idea that pressure can drive the growth of luminal organs and even control their size is not new, as exemplified by the papers of AJ Coulombre on the development of the chick eye published in the 50s[115,116]. However, the lack of tools to measure pressure and forces non-invasively (see Section 1.3) has delayed the acquisition of quantitative data and the elucidation of specific mechanisms.

One of the most studied structures in terms of the effects of hydrostatic pressure is the blastocyst, partially thanks to its simple morphology and the accessibility to its lumen. During the development of mouse blastocysts, luminal pressure increases two-fold, leading to increased cortical tension in the enclosing trophectoderm cells[112]. This tension induces mechanosensing via vinculin, that accumulates at tight junctions (suggesting that they are responsible for stress-bearing in the blastocyst, instead of adherens junctions). Since reduced tension results in defective tight-junction seals, this hints at a positive feedback loop linking tension and maturation of these junctions and aimed at withstanding pressure growth. However, there is a critical cortical tension above which cell-cell adhesion cannot be maintained during mitotic rounding, thus resulting in junctional leakage and, ultimately, a collapse of the blastocyst cavity. Furthermore, stiffening the trophectoderm by increasing cortical contractility causes a reduction on growth rate and size of the lumen. Conversely, softening produces increased lumen growth. Therefore, this process of luminal growth and collapse is dependent on tissue stiffness, and it generates oscillations that control blastocyst size[112] (**Figure 18**a,b).

Another structure whose size is controlled via a hydraulic feedback loop is the zebrafish inner ear[7]. At early developmental stages, the inner ear originates from an ectodermal thickening that cavitates to form the otic vesicle, which is filled with a fluid liquid called endolymph. In

this vesicle, pressure increases with luminal growth and it negatively regulates fluid transport. After puncturing of an otic vesicle (and the consequent pressure loss) luminal growth rate is increased, as demonstrated by regeneration of the luminal volume relative to the untouched otic vesicle of the same embryo, thus restoring bilateral symmetry. Later in development, the inner ear is connected through a duct to the endolymphatic sac. This sac helps to maintain pressure homeostasis by acting as a relief valve[117]. When pressure in the ear increases, it slowly inflates with endolymph and then rapidly deflates, causing inflation-deflation cycles.

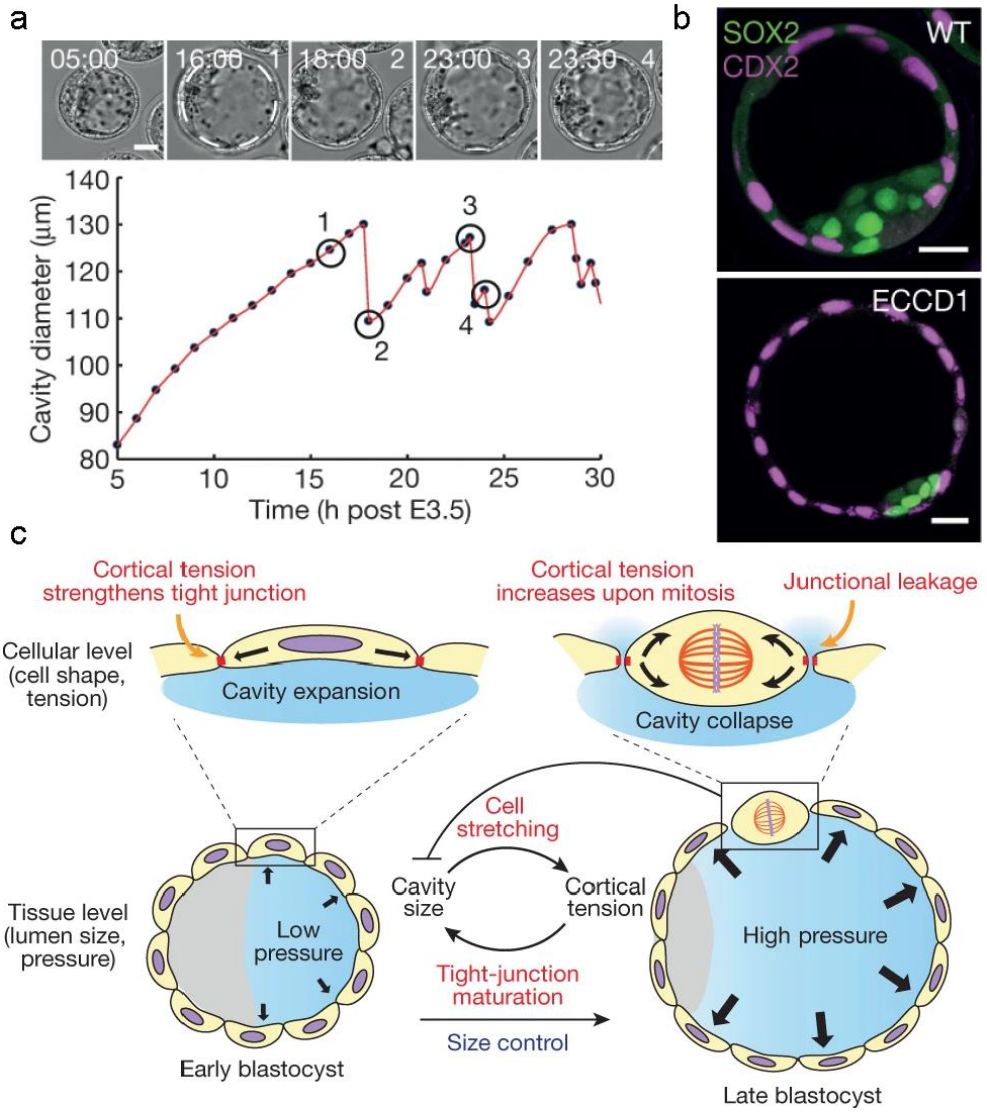

Figure 18: Blastocyst oscillations and size control. *a, Top, Timelapse images of a blastocyst. Dotted circle denotes cavity. Time is shown as h:min after E3.5. Bottom, plot of cavity diameter with time of (a). b, Immunostaining of late blastocyst stage (E4.25) untreated and ECCD1-treated embryos, showing trophectoderm (CDX2, magenta) and epiblast (SOX2, green) fate. ECCD1 is an E-cadherin-blocking antibody that weakens cellular adhesion (tissue softening). ECCD1-treated embryos show enlarged blastocoel in comparison to untreated control. c, Schematic showing how multi-scale feedback mechanisms between luminal pressure and tissue mechanics control the size of blastocysts. Luminal pressure stretches cells and generates mechanical stress at the tissue scale, which reinforces junctional maturation through mechano-sensing at the cellular scale. As tissue stress reaches a critical threshold, cell–cell adhesion cannot be sustained during mitosis, triggering junctional rupture and the collapse of the cavity. Tight junctions then re-seal and the blastocyst expands again, and the whole process repeats itself to generate size oscillations. Scale bars, 20 µm. Adapted from ref.*3.

Both in the blastocyst and the inner ear, and in many other systems such as organoids or the whole organism of the cnidarian *H. vulgaris*[118], we find that size is controlled by periodic hydraulic oscillations. These oscillations consist of growth of a hollow tissue through liquid permeation and cell division, followed by tissue rupture (**Figure 18**c). The repetition of this pattern among different structures and organisms suggests that hydraulic oscillations are a robust mechanism for size control in multicellular tissue cysts[119]. However, this mechanism alone cannot explain size control in lumens of different geometries and with different structures. Therefore, many processes involved in lumen homeostasis and size control remain yet unknown.

1.3 Measuring mechanics in epithelia surrounding a lumen

As previously mentioned, cells present internal stresses generated by subcellular components, and are subjected to external stresses caused by the environment, such as neighbouring cells or the ECM. At a tissue level, the generation and transmission of stresses can drive collective phenomena ranging from simple tissue contraction to complicated morphogenetic events. Even though the clearest examples of the effect of mechanical stresses occur during morphogenesis, they are important throughout the life of every individual. Mechanical functions such as compression, stretching or division are common in homeostasis, and abnormal stresses mediate diseases, like asthma or cancer[51,120]. Therefore, the study of tissue stresses can provide meaningful information on the mechanical processes involved in development, homeostasis, and disease.

The great diversity of existing stress-measuring techniques allows us to measure mechanics in many different contexts, ranging from 2D *in vitro* culture to *in vivo* settings. In 2D *in vitro* set-ups, we can find techniques such as 2D traction force microscopy, micropillar arrays or monolayer stress microscopy. In a 3D *in vitro* or *ex vivo* context, commonly used techniques include 2.5 and 3D traction force microscopy, and the micro-bulge test. Finally, *in vivo* methods comprise servo-null methods, FRET tension sensors, inclusions, laser ablation and force-inference methods. Each one of these techniques presents strengths and limitations, meaning that there is not an absolute technique valid for all settings. Generally, 2D *in vitro* methods have higher spatial resolution, but the system does not capture essential attributes

of the *in vivo* tissue. The other way round, *in vivo* data is more physiologically relevant, but the techniques do not provide absolute stress values.

Due to the great number of stress-measuring techniques, in this section I will discuss only some techniques used to measure mechanics in epithelia surrounding lumens. These techniques are servo-null methods, traction force microscopy, the micro-bulge test and force-inference methods (see for an overview of 3D stress-measuring techniques).

Table 1: Techniques to measure mechanical stresses in 3D living tissues (from reference 121*).*

Technique	Measured quantity	Output	Strengths	Limitations
3D, in vitro and ex vivo methods				
2.5D traction force microscopy	3D displacement of a gel substrate	3D traction vector	3D traction can be measured	Anisotropic 3D point spread function; very sensitive to noise (high-quality measured displacements are needed); computational complexity
3D traction force microscopy	3D displacement of the ECM surrounding the tissue	3D traction vector	3D traction can be measured; physiologically relevant ECM	Anisotropic 3D point spread function; nonlinear material behaviour of the surrounding ECM; cells remodel and degrade ECM; computational complexity
Microbulge test (domes)	3D displacement of the substrate surface	Luminal pressure and internal stress of curved monolayer	No need to assume any constitutive behaviour for cells; accessing internal tension for curved monolayers	Only applicable to cell types that form domes
In vivo methods				
Servo-null methods (pressure gauges)	Electrical resistance at the capillary tip	Luminal pressure	Direct access to luminal interstitial pressure	Invasive; complex experimental set-up
Inclusions	Inclusion shape and/or deformation	Local tissue stress tensor components	Able to report 3D tissue stress	Only accesses stress value near to the inclusion; might perturb force transmission in the tissue; requires microinjection in vivo
FRET tension sensors	Fluorescence intensity	Local tension at the molecular level	Genetically encoded; local measurement	Only reports tension, not compression; calibration issues; no directional information; unclear effect of the surrounding medium and fluorophore stability
Laser ablation	Recoil velocity	Relative tissue stress	High spatiotemporal control of the perturbation; easy implementation	Invasive; relative measurements unless viscosity of the tissue is assumed
Force-inference methods	Tissue shape	Relative local internal stress	Very simple experimental implementation; non-invasive	Relative measurements only; computational complexity; highly sensitive to segmentation noise

1.3.1 Servo-null methods for measuring luminal pressure

Servo-null methods are techniques used to measure luminal pressure. They are based on the insertion into the lumen of a glass micropipette filled with a saline solution that has very low electrical impedance (resistance to the movement of electrons), much lower than the fluid of

the studied lumen. When the tip is introduced in the lumen, the higher pressure will drive luminal fluid into the tip, thus increasing the impedance of the solution. This difference in impedance is sensed by a servo system, that sends the signal to a transducer. This transducer then generates a counter-pressure that equilibrates luminal pressure and restores the initial impedance. The counter-pressure applied is assumed to be equivalent to the luminal pressure[121].

The development of these servo-null devices dates to the 1960s, and they were first used to measure pressure in microcirculation vessels[122]. Currently, the improvements in these devices allow us to measure pressures in many *in vivo* systems and at different length scales, ranging from the cytoplasm of a cell to a whole organ. Servo-null devices are broadly used to study embryonic development and they have led to many discoveries, such as the hydraulic feedback mechanisms described in Subsection 1.2.3.4.

Despite their clear applications and potential to measure pressure in microscopic structures, these systems have several disadvantages. They are invasive techniques with a complex experimental set-up that can lead to measurement errors, like leakage at the puncture site or the presence of bubbles inside of the tip. Additionally, the tip resistance is usually dismissed, possibly overlooking measurement biases.

1.3.2 Traction Force Microscopy

Traction Force Microscopy (TFM) is a technique that allows the measurement of the tractions exerted by cells and tissues on soft elastic substrates. The first attempt to quantify 2D cellular forces was carried out by Harris and co-workers in 1980 [123]. They seeded fibroblasts on silicon rubber substrates and measured the forces they exerted by mimicking the deformations on the membrane with calibrated glass microneedles.

Currently, 2D TFM is usually performed on polyacrylamide or soft polydimethylsiloxane gels, which are transparent and present tuneable stiffness. Traction forces generated by cells are transmitted to the substrate and measured by imaging the displacement of fluorescent markers embedded in the gel or attached to its surface. Usually, computing these displacements involves detaching the cells from the substrate to obtain a reference image of

the relaxed configuration. However, recent studies bypass this limitation by distributing the markers in a regular array[124].

To obtain cellular tractions, mechanical equilibrium is imposed for the substrate, meaning that there are no external forces acting on the tissue and, thus, the internal stresses balance themselves. Additionally, a constitutive behaviour is chosen for the substrate. Commonly this behaviour is assumed to be linear elastic: substrate deformations are assumed to be small and the relationship between stress and strain is linear. If these assumptions do not hold, the tractions have to be calculated using finite element methods[121].

TFM has been a crucial tool for the mechanical study of single-cells and tissues *in vitro*. It has shed light on the tractions that cells exert when they interact with their environment, migrate or divide. It has also enabled the *in vitro* study of collective processes such as wound healing

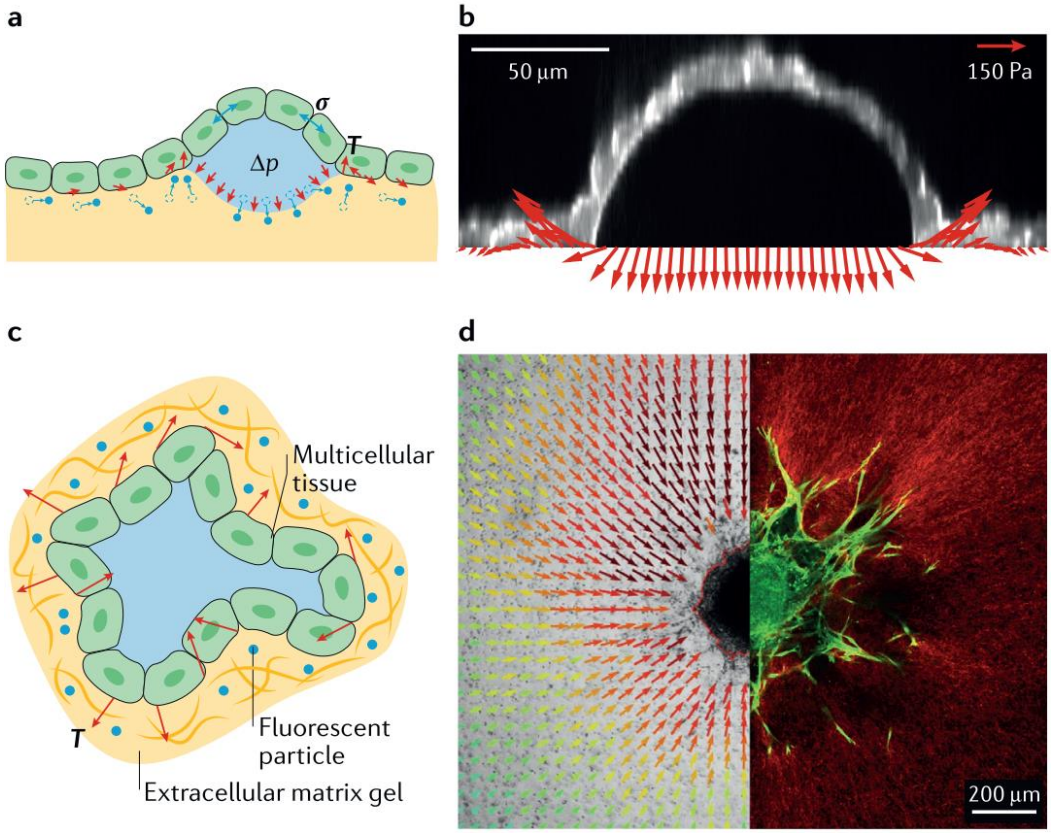

Figure 19: 2.5D TFM and 3D TFM. *a, Schematic of a 2.5D TFM setup. Cells are seeded on top of a 2D elastic substrate, and the changes in position of fluorescent particles embedded in the substrate (blue dots) are measured in 3D. From these displacements, the 3D traction field can be calculated. For spherical cap geometries, tissue stresses can be computed using the microbulge test. b, Representative 2.5D TFM experiment compatible with the microbulge test. 3D traction field (red arrows) generated by an epithelial dome (side view) on a flat substrate. c, Schematic of 3D TFM. The full 3D displacement field (red arrows) for tissues grown inside a deformable ECM gel can be measured by detecting changes in the position of embedded particle tracers by confocal microscopy. From this field, the full 3D traction field can be inferred. d, Representative 3D TFM experiment. Breast-cancer spheroid embedded in a 3D collagen I matrix. Bright- field microscopy image (left) with superimposed ECM displacements (arrows) and fluorescent-microscopy image (right) of the spheroid (green) and matrix (red) From ref.*121.

or jamming transitions[51,125]. However, even though this technique is very versatile and its application is straightforward, it presents some drawbacks. Firstly, sing the displacements to retrieve the tractions is an ill-posed problem, and therefore very sensitive to experimental noise. Secondly, as implied by its name, 2D TFM can only measure in-plane tractions and not out-of-plane components. This second limitation can be overcome with the implementation of 2.5D or 3D TFM techniques.

2.5D TFM measures a 3D displacement field on the surface of the gel and uses it to obtain the 3D traction vector field (**Figure 19**a,b). The mathematical and computational approaches used in 2.5D are the same ones as in 2D TFM. In addition to the previous assumptions about the substrate (isotropic, linear elastic), it is usually considered as incompressible, thus uncoupling the tractions parallel to the gel (in-plane) and the perpendicular ones (vertical)[126].

If we want to study cells or tissues in a physiological environment, we may want to measure the tractions exerted on 3D ECM. This calculation of a 3D traction field from 3D displacements is what is called **3D TFM** (**Figure 19**c,d). The biggest challenges of this technique are the differentiation of displacements due to cellular tractions from those generated by ECM remodelling, and the nonlinear behaviour of ECM. To deal with these problems, some experiments are carried out using materials with well-characterized viscoelastic properties or synthetized artificial matrices that have a linearly elastic behaviour[127,128]. Furthermore, some research groups have started to characterize the elastic properties of ECM components, such as collagen gels[129].

1.3.3 Micro-bulge test

The micro-bulge test consists on the formation of domes on a soft, impermeable and elastic substrate, such as polydimethylsiloxane gels. As explained in Section 1.2.3.4, domes are cell monolayers confining pressurized basal lumens. The enclosing monolayer is described as an infinitely thin membrane supporting stresses tangential to its surface and a uniform transepithelial pressure exerted by the luminal fluid. Due to the sharp contact angle between the domes and the gel, bending moments and out-of-plane stresses can be neglected[54].

As previously mentioned, these domes present a geometry very similar to a spherical cap[114]. This symmetry implies that the tangential stress is uniform, isotropic and can be described

using only a scalar value. Therefore, the stress state can be computed by imposing mechanical equilibrium. This equilibrium is described by Laplace's Law[130], which states that the surface stress (σ) is directly proportional to the hydrostatic luminal pressure (ΔP) and the radius of curvature of the dome (R).

$$\sigma = \frac{\Delta P R}{2} \tag{5}$$

Luminal pressure can be easily measured using 2.5D TFM and the radius of the dome can be estimated from confocal z-stacks of the cells. The micro-bulge test is a very robust technique for stress measurement because it is based solely on mechanical equilibrium. In other words, we do not need to assume any constitutive behaviour for the monolayer. However, this technique can be used only with cell types that form hemilumens.

1.3.4 Force-inference methods

Force-inference methods compute the internal mechanical balance of the tissue from images of cell geometry (**Figure 20**a). The forces involved in this balance include cell cortical tensions, internal pressures generated by the cytoplasm, the elastic and viscous responses of cellular components, and frictional responses to deformation[131]. In most experiments, inertia is negligible, and the forces equilibrate each other adding up to zero. Moreover, experiments often extend over timescales long enough that the contribution of viscous dissipation and elastic components is irrelevant. Therefore, force-inference models often consider only two sources of force: surface tensions and internal pressure[121].

These models assume that the tensions and pressures equilibrate at the vertices of cellular junctions and cell-cell interfaces, where Laplace's law is invoked (**Figure 20**b). The previous

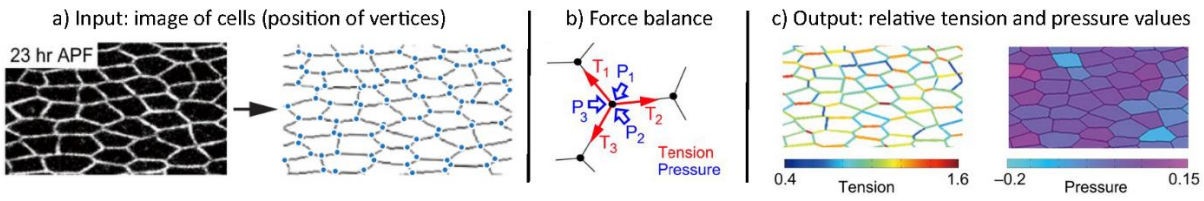

Figure 20: Force inference example in the* Drosophila *pupal wing. *a, Cell geometry and vertex positions are extracted from a fluorescence image of cell membrane from the* Drosophila *pupal wing at 23 h after pupa formation (APF). b, The force balance equations are defined for every vertex. The equations present a contribution from cell-cell interface tensions (T) and another from differences in cellular pressures (P). c, Solving these equations yields a map of cell-cell interface tensions, relative to an unknown constant, which is the average tissue tension. The inferred cell pressure map has another unknown, an additive constant, which is the average pressure. Adapted from ref.*132.

assumptions allow the calculation of relative pressures and tensions without assumptions of material properties of cells and tissues (**Figure 20**c). The scaling constant factor that relates the model calculations and the tissue pressure and tension can be obtained by measurements with another technique, such as TFM or servo-null methods. The methodology consists on measuring the contact angle between cells at intercellular junctions. Subsequently, forces are inferred from the deviation of these angles from the equilibrium configuration. This methodology can be formalized using vertex models.

Mechanical equilibrium requires that the sum of forces is equal to zero at each vertex and, therefore, it requires one equation per vertex. This equilibrium depends on the unknown pressure and tension of adjacent cells, making it possible to generate an algebraic system of equations from the geometrical information of the tissue[131]. However, at the vertices where multiple cells meet, the system is underdetermined. To solve this issue, different approaches have been applied, such as making the system overdetermined. An option to accomplish this is to assume that tension is uniform (reducing the unknowns to only cell pressures), like has been done in the retina of *Drosophila*[133]. Conversely, we can assume that all cells present the same pressure and consider the tensions as the only unknowns.

The main advantages of inference methods are that they are non-invasive and require only imaging of the tissue, they make minimal assumptions about the origin of tissue forces, and they can be easily combined with other methods. However, these methods also present several limitations. They assume that tensions along cell edges are positive and constant (which does not necessarily apply to wiggly junctions[134]), the measurements obtained are relative unless they are combined with another measuring technique, and results are highly dependent on the accuracy of the cellular segmentation. Furthermore, the underlying model may require modifications in the presence of actin belts, cell polarization, lamellipodia or other cellular processes that are not considered in the conceptual framework of force-inference methods.

It is interesting to mention that, although force-inference methods are usually applied to compute stresses at a cellular level, they can also be applied to estimate local stress on luminal epithelia. If the thickness of the epithelium is sufficiently small, we can model it as an inflated membrane. In membrane theory, stresses are assumed to be tangential to the surface; in other words, the bending stresses are assumed to be negligible. In this situation,

the system of equations is statically determinate, and we can infer stresses from tissue shape and pressure difference across the membrane. This kind of model has been applied to the estimation of stresses in brain aneurysms[135,136].

2 AIMS

2.1 General aim

The general aim of this thesis is to understand how mechanical stress depends on pressure, size and shape in fluid-filled curved epithelial sheets.

2.2 Specific aims

This general aim can be divided in the following specific objectives:

1. To develop a TFM-compatible protocol to generate curved epithelial monolayers with any desired size and shape.
2. To study the effect of size on the mechanical properties of spherical-cap epithelial monolayers.
3. To validate an inference method to map the stress tensor anywhere in the monolayer without assumptions of mechanical properties.
4. To study the effect of anisotropy on the mechanical properties of curved epithelial monolayers with rectangular and ellipsoidal footprints.
5. To study the relationship between stress anisotropy and cellular geometry and alignment in curved epithelial monolayers.
6. To study the relationship between stress anisotropy and nuclear geometry and alignment in curved epithelial monolayers.

3 METHODS

3.1 Cell lines and culture

All experiments described in this thesis were performed with Madin-Darby Canine Kidney cells type II (MDCK II). More specifically, we used a stable cell line containing the CIBN-GFP-CAAX construct[137]. This cell line presents a green fluorescent protein (GFP) anchored at the membrane using the CAAX motif, thus allowing visualization of the cell membrane. The construct also presents an optogenetic receptor (CIBN) that has not been used in this study. MDCK cells are the most suitable ones for this study because they spontaneously form pressurized hemi-lumens in 2D culture[111].

Cells were cultured in standard flasks for culture of adherent cells (Nunc EasyFlasks, Life Technologies) with MEM (31095052, Life Technologies) supplemented with 10% fetal bovine serum (10270-106, Life Technologies) and 1% penicillin-streptomycin-Glutamine (10378-016, Life Technologies). The same medium composition was used to carry out the experiments.

The cell line tested negative for mycoplasma contamination.

3.2 Preparation of soft polydimethylsiloxane substrates

3.2.1 Fabrication of soft polydimethylsiloxane gels

The experiments were carried out on soft silicone gels synthesized by mixing A and B polydimethylsiloxane (PDMS) components in a 1:1 weight ratio in ice (DOWSIL™ CY 52-276). The proportion of A and B components was critical to achieve the desired stiffness, which was 3 kPa. The mix was then degassed for 30 minutes and, afterwards, 100 µl were placed on each glass bottom dish (P35G-0-20 Mattek) and spun for 90 seconds at 400 rpm. The gels were curated overnight at 65°C in an oven.

3.2.2 Coating the PDMS gels with fluorescent beads

To reduce the amount of reagents used, a thin PDMS stencil with annular shape (internal diameter 7 mm, external diameter 10 mm) was placed on top of the gels.

The soft PDMS substrates were treated with (3-aminopropyl)triethoxysilane (APTES, Sigma-Aldrich, cat. no. A3648) diluted at 5% in volume in absolute ethanol for 3 minutes and then rinsed three times with absolute ethanol.

Red fluorescent carboxylate-modified beads (FluoSpheres™ F8801, Invitrogen) were diluted in a 1:60 ratio (for imaging with a 40x objective) or a 1:40 ratio (for a 60x objective) in a buffer consisting of sodium tetraborate (3.8 mg/ml, Sigma-Aldrich) and boric acid (5 mg/ml, Sigma-Aldrich). The suspension was then sonicated for 5 minutes and filtered with a 0.22 µm syringe filter (SLGV004SL, Millipore) to avoid clusters of beads. The gels were incubated with the beads' suspension for an hour, then rinsed with type I water four times.

The addition of fluorescent beads is necessary to perform Traction Force Microscopy. More details about TFM 2.5 methodology can be found in Subection 3.6.1.

3.2.3 Stiffness measurements

The stiffness of the gels was measured as described in ref.[54]. Briefly, a large 1 mm-diameter metal sphere of known mass was used to generate an indentation on the gels. Then, the depth of the indentation was quantified using confocal microscopy. Using the indentation depth and the sphere mass, we computed the Young modulus by applying Hertz theory and correcting for the finite thickness of the gel[138] (**Figure 21**). The resulting Young modulus was 2.9±0.7 kPa

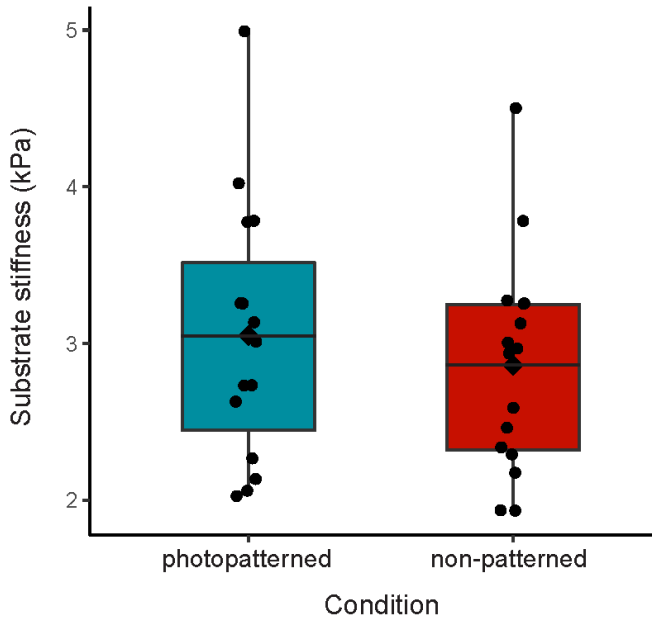

(mean±s.d.). Repeating the same measurements on photopatterned gels shows that stiffness was not affected by photoillumination (3.1±0.8 kPa).

Figure 21: Stiffness quantification of photopatterned and non-patterned soft PDMS gels. *Solid line indicates the mean. n=15 (photopatterned), n=16 (non-patterned). Samples from 3 independent batches.*

3.3 Micropatterning of soft polydimethylsiloxane substrates

3.3.1 Substrate passivation

The gels were incubated for 30 minutes with 1% poly-L-lysine (P8920, Sigma Aldrich) and then rinsed four times with 10 mM Hepes (H7523, Sigma Aldrich). Both reagents were diluted in type I water. This process ensured that the gels were covered with a layer of positive charges.

Afterwards, the gels were incubated with mPEG-Succinimidyl valerate (mPEG-SVA, Laysan Bio) at a concentration of 50 mg/ml in 10 mM Hepes for an hour. For a successful passivation, the Hepes solution must be adjusted to pH 8.2-8.4 to avoid fast decay of mPEG-SVA. mPEG-SVA forms amide bonds with PLL, thus leading to a good passivation of the substrate.

The gels were then rinsed four times (without letting them dry), covered with type I water and stored in the fridge until patterning (1-2 days).

3.3.2 Photopatterning using PRIMO

Micropatterning of the substrates was carried out using a device called PRIMO, developed by the company Alvéole. This system is based on LIMAP (Light Induced Molecular Adsorption of Proteins)[139] and uses a UV laser (λ=375nm) to locally activate a compound, 4-benzoylbenzyl-trimethylammonium chloride (custom synthesis by Sigma-Aldrich outsourced to SinoChem,

China), that cuts the PEG chains that cover the substrate (**Figure 22**). To generate the desired patterns, this system needs to be mounted on a microscope with a motorized stage.

The system is controlled by a MicroManager plugin called Leonardo. This software enables the selection of the jpg/pdf pattern that will be reproduced, the energy dosage used per mm², and the power of the laser. The pattern templates must be in greyscale and the brightness indicates the amount of light they will receive, from white (maximum) to black (no light). Therefore, a brighter shade will correspond with a higher amount of protein than a darker one.

To generate our samples, we loaded our patterns onto the Leonardo software and then selected a dosage of 900 mJ/mm^2 with maximal laser power. Afterwards, the samples were rinsed four times with PBS (D8662, Sigma Aldrich) incubated for 5 minutes with a 0.02% solution of fibronectin (F0895, Sigma-Aldrich) and 0.03 mg/ml fibrinogen (Alexa Fluor™ 647 Conjugate, F35200, Life Technologies) in PBS. The adhesion proteins attached to the illuminated regions, where the PEG chains were cut. Finally, the samples were rinsed four more times and left with PBS in the fridge until cell seeding (less than one week).

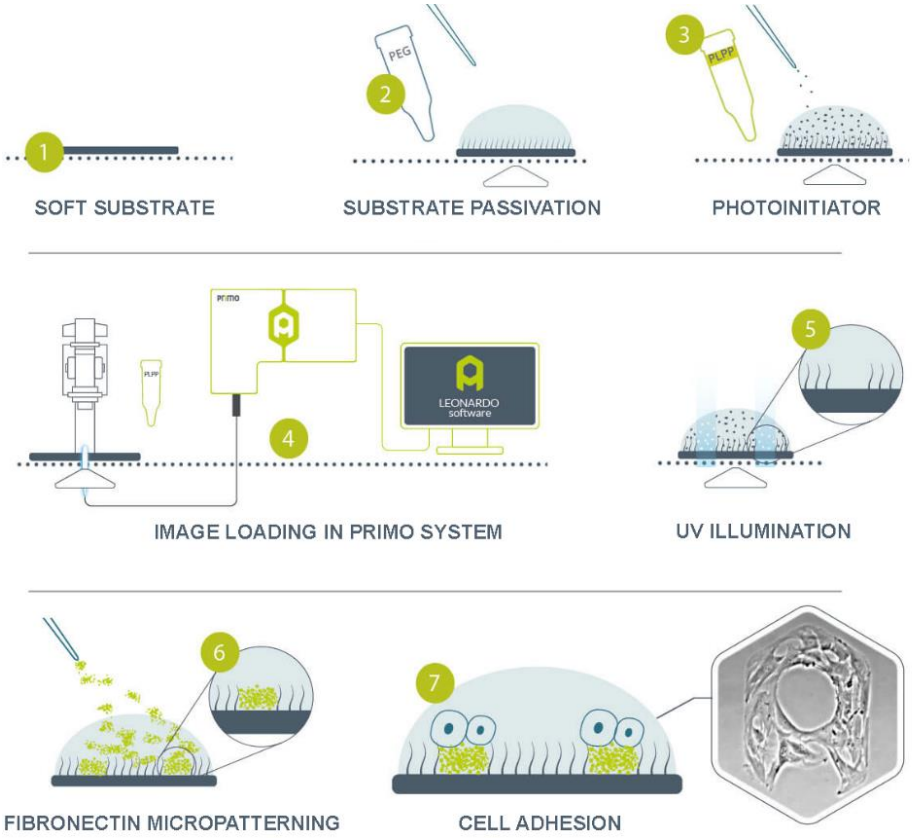

***Figure 22: Photo-patterning protocol with PRIMO**. First, (1,2) the soft substrate is incubated with a passivating PEG agent and then rinsed. (3) The photoinitiator is then added to the sample and the sample is placed in the microscope. (4) The desired pattern image is loaded into the Leonardo software and (5) the program starts illumination with a UV laser. (6) Afterwards, the sample is rinsed, incubated with fibronectin and rinsed again. (7) The sample is then ready for cell seeding. Adapted from ref.*140.

3.3.3 Pattern design

The patterns were designed using the Inkscape software. To examine the effects of size, we generated circles with diameters of 25, 50, 100 and 200 µm. To study the effect of shape, we generated ellipses (65x98 µm and 46x138 µm) and rectangles (71x71 µm, 50x100 µm, 35x141 µm) with the same area (5000 μm^2), but different degrees of anisotropy.

Different patterns were arranged using hexagonal ordering and with a separation of 200 µm between them into arrays of approximately 3x3 mm. The rectangular array was white, which corresponds to the maximum amount of protein attached using photopatterning. In patterns with big motifs (an area larger than 5000 μm^2), the low-adhesion area was designed a medium-dark grey color (1/5 of the maximum brightness) to allow some protein attachment and cell adhesion on the patterns (**Figure 23**). In patterns with smaller motifs, the low-adhesion area was a darker grey (1/8 of the maximum brightness).

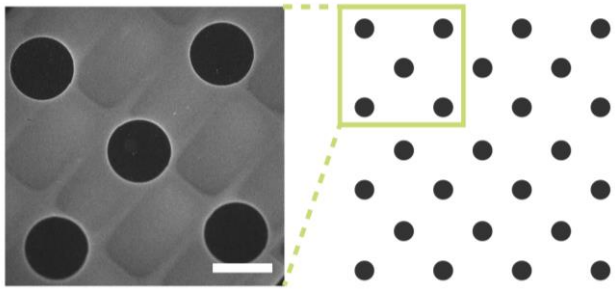

Figure 23: Circular dome pattern. *Left: Fluorescence image of a fibronectin and fluorescent fibrinogen pattern. Scale bar= 100 µm. Right: Section of a 100 µm-diameter input pattern.*

3.4 Cell seeding and density

Firstly, MDCK cells grown on culture flasks were rinsed with PBS (D8662, Sigma Aldrich) and incubated with 1.5 ml of 1X trypsin (T3924, sigma Aldrich) for 15 minutes at 37°C. When the cells detached from the substrate, they were resuspended in 10 ml of media and 10 µl of the suspension were placed on a Neubauer chamber to count the number of cells. The remaining cell suspension was centrifuged at 1000 rpm for 5 minutes. The supernatant was aspirated, and then the pellet was resuspended in media to achieve a concentration of $3 \cdot 10^6$ cells/ml.

Before cell seeding, the soft PDMS gels had been sterilized with UV light for 15 minutes inside of the culture hood. The PBS in the samples was aspirated and the region delimited by the stencil was rinsed once with 50µ l of media. Afterwards, 50 µl of the cell suspension were carefully placed inside the stencil. The samples were incubated at 37°C for approximately 50

minutes to allow the cells to attach to the gel. The samples were then thoroughly rinsed with PBS to remove cells that were not completely attached to the pattern. Then, 2 ml of media were added to each sample, and the samples were placed in the incubator at 37°C for 16-48 hours.

The incubation time depended on the size of the desired structures, with larger structures needing more time to form a cohesive monolayer on the low-adhesion areas and to inflate. Curved monolayers presented similar cell densities across sizes (refer to Section 4.2 for the data). Cell density was assessed using the following formula:

$$Density = \frac{(c_i + c_b/2)}{A} \quad (6)$$

, where c_i is the number of cells completely on the dome, c_b is the number of cells at the dome boundary (partially on the dome, partially outside of it) and A is the patterned substrate area.

3.5 Image acquisition

3.5.1 Multidimensional acquisition for traction force measurements

Live imaging was performed using an inverted Nikon microscope with a spinning disk confocal unit (CSU-W1, Yokogawa), Zyla sCMOS camera (Andor, image size 2048x2048 pixels). The microscope was equipped with temperature and CO_2 control. For imaging of big structures, with a diameter of at least 100 µm, we used a Nikon 40X 0.75 NA air objective (CFI Plan Fluor 40x/0.75 DIC WD 0.66). For imaging of smaller structures, a Nikon 60X 1.2NA Water objective was used (Plan Apo VC 60X/1.2w WD 0.31-0.28).

The microscope was controlled using the MicroManager software. The acquisitions consisted of two stacks for each position and timepoint. The green stacks corresponded to the cell membrane (GFP) and consisted of a variable number of planes and a step between 0.8 and 3 µm. The red stacks consisted of images of the fluorescent beads necessary for TFM. All red stacks had 60 planes and a step of 0.2 µm. These stacks were acquired for every position every 30 minutes. Due to the complexity of the acquisition routine, we wrote a home-made script to perform it.

After the experiment, the cells were detached from the gel using 10X trypsin (15400-054, Life Technologies) and a stack of the beads was taken. The settings of the acquisition, such as laser power and exposure time, were the same as those used during live imaging. These images served as a reference for the computation of traction forces (see Subsection 3.6.1).

3.5.2 Multidimensional acquisition for nuclei and cell segmentation

Live imaging was performed using the same microscopy set-up from the previous subsection, and a Nikon 60X 1.2NA Water objective (Plan Apo VC 60X/1.2w WD 0.31-0.28). The microscope was controlled using the MicroManager software.

Fifteen minutes before image acquisition, the samples were placed in the microscope and Hoescht was added to the medium at a final concentration of 1:1000. The acquisitions consisted of only one timepoint with stacks of three different colors for each dome. The green stacks corresponded to the cell membrane (GFP) and consisted of a variable number of planes and a step of 0.5 µm. The blue stacks corresponded to the nuclei and had the same step and number of planes as the green ones. The red stacks consisted of images of the fluorescent beads necessary for TFM. All red stacks had 60 planes and a step of 0.2 µm. Due to the complexity of the acquisition routine, we wrote a home-made script to perform it.

After the experiment, the cells were detached from the gel using 10X trypsin (15400-054, Life Technologies) and a stack of the beads was taken as explained in the previous subsection.

3.6 Calculation of experimental tractions, pressure and stresses

3.6.1 2.5D Traction Force Microscopy

2.5D traction forces were computed using traction microscopy with finite gel thickness[141,142]. The 3D displacement field of the top layer of the gel at any given timepoint was obtained by using as a reference the image of the beads after cell trypsinization. The displacement field was computed using a home-made particle imaging velocimetry software based on an iterative algorithm with a dynamic interrogation window size and implementing criteria for

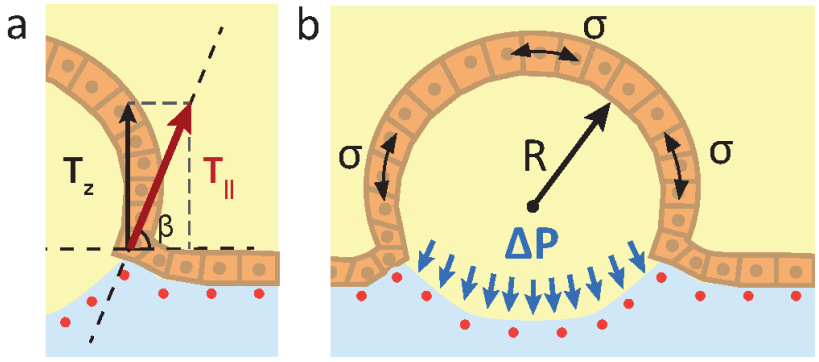

Figure 24: Pressure, traction and tension in domes. *a, Schematic showing vertical and tangential traction components at the boundary of a dome. Tangential tractions follow the direction of the contact angle, β. b, Schematic of the relevant components in Laplace's Law for spherical domes. The radius of curvature, R, and the luminal pressure, ΔP, are measured to infer the stress in the monolayer, σ.*

convergence based on image intensity as described in previous publications[54,143]. The different software and scripts used for calculation of traction forces were written for Matlab.

3.6.2 Luminal pressure and tractions of domes

Results from TFM calculations showed an indentation on the gel in the region below the lumen of the domes. This indentation corresponded to the pressure the luminal fluid exerted on the surface of the gel. Since the pressure is constant through the lumen, we could compute luminal pressure by averaging the traction values on the central region of the dome. By computing the tangential component of the tractions at the dome boundary, $T_{||}$, we can estimate the contribution of the free-standing cell sheet to the measured tractions. This contribution is computed as described in Equation 7, where T_z is the vertical component of the measured tractions and β is the contact angle between the dome and the substrate (**Figure 24**a).

$$T_{||} = T_z / sin\beta \tag{7}$$

For cases where β was very small, the resulting $T_{||}$ skyrocketed due to the inherent noise level of TFM (T_z~10 Pa). In these cases, T_z was used in the study of ellipsoidal domes.

3.6.3 Luminal pressure and surface stress of spherical domes

To represent the pressure and traction profile of spherical domes, we can take advantage of the symmetry of the system. First, we expressed the traction results in cylindrical coordinates (radial, tangential and Z components), instead of cartesian coordinates (x, y and z). Then, we divided the dome in concentrical regions and averaged the tractions radially according to the

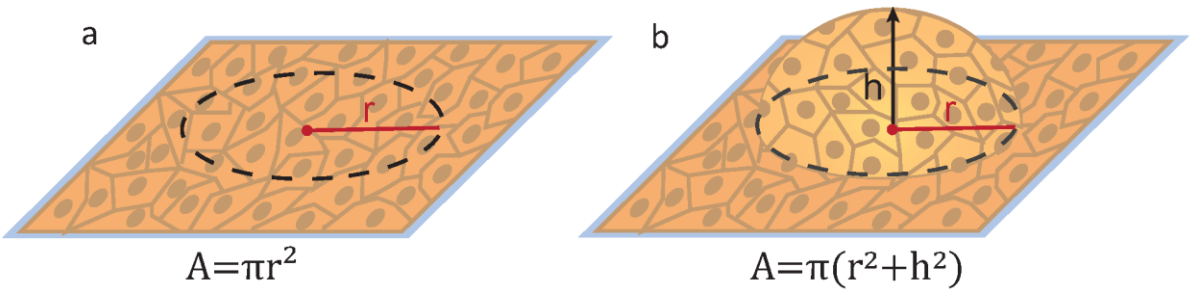

Figure 25: Schematic of area calculation. *Area calculation of (a) a flat monolayer on a circular footprint and (b) a spherical cap dome.*

distance from a point to the center of the dome. This allows us to plot the traction/pressure profile for each spherical dome.

For the specific case of spherical domes, we can compute analytically the surface stress in the monolayer enclosing the lumen. In the absence of bending stresses, we can define the stress as a 2x2 tensor $\bar{\bar{\sigma}}$. For structures with spherical symmetry such as cysts, blastocysts, or domes with circular footprints, the stress is uniform and isotropic, implying that $\bar{\bar{\sigma}}$ is diagonal and has equal diagonal elements σ. Thus, we can use Laplace's law ($\sigma = \Delta PR/2$) to compute σ from measurements of the luminal pressure and radius of curvature of the dome (**Figure 24**b, for more information see Subsection 1.3.3). To compare domes with a similar inflation level, we defined the areal strain, ε_a, as the normalized difference between the actual dome area and the area of the footprint:

$$\varepsilon_a = \frac{\pi(h^2 + a^2) - \pi a^2}{\pi a^2} = \left(\frac{h}{a}\right)^2 \quad (8)$$

, where h is the height of the dome and a is the radius of the footprint (**Figure 25**).

3.7 3D vertex model

To study the contribution of bending moments to balance luminal pressure, we used a 3D vertex model developed by Adam Ouzeri and Prof. Marino Arroyo based on a previous publication[54]. This model combines the constraints imposed by contractility of the actomyosin cortex, volume conservation of each cell, and an increase in dome lumen volume to simulate a 3D epithelial monolayer with curved surfaces.

The epithelial cells within a monolayer are assumed to be polyhedra composed of polygonal apical and basal faces, and rectangular lateral faces. To allow for curved surfaces, each face is further discretized using linear triangular elements (**Figure 26**a). Following our observations, we further assumed that throughout dome inflation, no topological rearrangements occurred within the tissue. Cells retain their original connectivity and tissue deformation is only accommodated through cell shape changes.

3.7.1 Virtual work function

We assumed that the actomyosin cortex, which lines the interior of each cell face, is the main subcellular element determining the mechanics of the epithelium. Due to the longer timescale of dome inflation compared to actomyosin dynamics[144], we assumed that all cortical dynamics are at steady-state throughout the dome inflation process and that the cortex generates a constant and isotropic active surface tension, which can be different on each cell face. Therefore, we expressed the mechanics of the actomyosin cortex on a face f of cell c using a conventional virtual work function:

$$\delta W_{f,c}(x_1, \ldots, x_{N_{f,c}}) = \gamma_{f,c}\delta A_{f,c}(x_1, \ldots, x_{N_{f,c}}) \qquad (9)$$

where x_i denotes the position of node i in the triangulation of the face, $\gamma_{f,c}$ is the active tension generated by the cortex, and $A_{f,c}$ the corresponding face surface area. We assumed that apical and basal tension are contractile, and that contractility on the lateral faces dominates over adhesion, meaning that $\gamma_f > 0$ for all faces (**Figure 26**a). To account for observed differences between apical and basal cell-cell contact angles, the apical-to-basal surface tension ratio was set to 1:9 for the simulations (higher tension in the basal faces).

3.7.2 System constraints

To avoid cell collapse due to contraction of all faces, we assume that each cell volume Ω_c is conserved. Volume conservation is imposed through a Lagrange multiplier requiring that the change in cell volume remains zero

$$\Omega_c(x_1, \ldots, x_{N_c}) - \Omega_c^0 = 0 \qquad (10)$$

where Ω_c^0 is the initial volume of cell c and N_c is the number of nodes on cell c.

To simulate dome inflation, we define a region of the basal surface as adhered to the substrate (movement of nodes is restricted) and allow for nodes in a non-adherent region to move freely (**Figure 26**b). The volume of the lumen enclosed between the non-adherent region and the substrate is then increased through a Lagrange multiplier requiring the lumen volume at each step of the dome inflation Ω_l to be equal to the imposed volume $\Omega*$.

$$\Omega_l(x_1, \ldots, x_{N_c}) = \Omega* \tag{11}$$

where N_l is the number of nodes in the lumen.

3.7.3 Lagrangian expression

After defining the virtual work function and the constraints of the system at each cell face, we can summarize the dynamics of the system using a Lagrangian function.

$$\delta\mathcal{L}_t = \sum_{c\in\langle t\rangle}\left(\sum_{f\in\langle c\rangle}\gamma_{f,c}\delta A_{f,c} - \Delta P_c\,(\delta\Omega_c - \delta\Omega_c^0)\right) + \Delta P_l(\delta\Omega_l - \delta\Omega*) \tag{12}$$

where the summation is done over all faces f forming the cell c and all cells forming the tissue. The Lagrange multiplier ΔP_c is the pressure difference across the cell interior and the exterior medium. The Lagrange multiplier ΔP_l gives a direct readout of the pressure inside the lumen of the dome.

3.7.4 Stress calculation in spherical dome simulation

For spherical domes, we again used Laplace's law to estimate tension in the monolayer as a function of dome radius R and luminal pressure ΔP_l (**Figure 26**c,d). In a scenario where we have an idealised tissue made of identical hexagonal cells subjected to equibiaxial stretch, eq. (12) can be greatly simplified and the problem can be treated analytically. In this condition, the surface stress is defined by the following cellular constitutive equation[54]:

$$\sigma = \gamma_a + \gamma_b - \gamma_l\frac{k}{(\varepsilon_c + 1)^{3/2}} \tag{13}$$

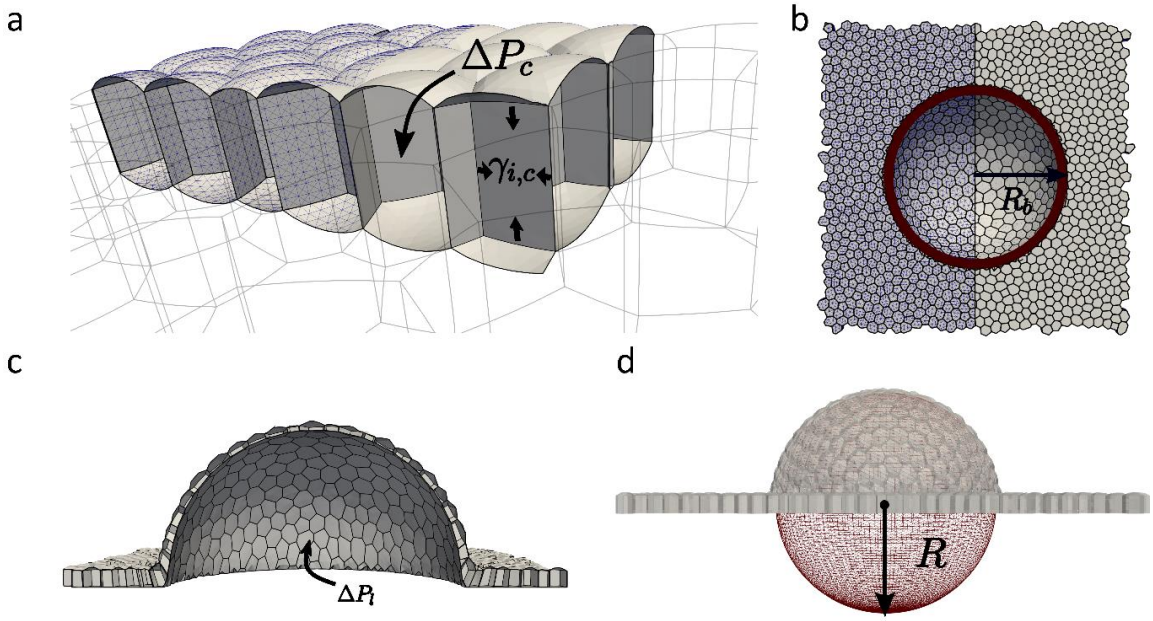

Figure 26: Dome vertex model. *a, Constant and isotropic surface tension on each face $\gamma_{i,c}$ along with cell volume conservation generate a cellular pressure that bulges non-adhered surfaces outwards. b, We defined a non-adherent region of radius R_b on the basal footprint, outside which nodes are fixed. c, We imposed an incremental volume increase in the non-adherent region through a Lagrangian multiplier, leading to a direct readout of lumen pressure ΔP_l. d, Inflated domes can be closely approximated as spherical caps. Figure by Adam Ouzeri.*

where γ_a is the apical surface tension, γ_b the basal surface tension, γ_l the lateral surface tension, ε_c is the cellular areal strain and k is a non-dimensional geometrical constant accounting for cell volume conservation. Equation (13) describes the local stress-strain (constitutive) relation of a tissue made of identical cells deforming identically. As the tissue stretches, contribution to tissue tension from the lateral faces decreases, therefore tissue tension would saturate to $\gamma_a + \gamma_b$.

3.8 Stress inference in anisotropic domes

In anisotropic shapes, such as tubes or ellipsoids, the surface stress of the free-standing sheet cannot be calculated analytically using the micro-bulge test. For this reason, we applied and validated a computational approach developed by Prof. Sohan Kale, to infer surface stresses from geometrical data of our domes.

3.8.1 Fit of a smooth surface to experimental data

To compute surface stresses, we needed to generate a smooth surface that captured the geometry of our domes. For this purpose, we used confocal stacks to segment the luminal

surface of the domes in Fiji (ref. [145]). The surface was defined in 3D by manually adding points in the x-z or y-z views and interpolating the in-between surface with the "Volume Manager" plugin (R. Haase, MPI-CBG). Then, we triangulated the 3D point cloud. We next mapped the generated open surface on a unit disc using a disc conformal map (which preserves the angle of intersection of any lines or curves unchanged). We re-meshed the part of the disc corresponding to the dome surface to improve mesh quality. Finally, we obtained a fitted smooth surface by minimizing the difference between our mesh and the point cloud, while penalizing sharp changes in the surface gradient (**Figure 27**). At the footprint boundary there is no penalization because the dome must present a sharp interface with the substrate.

3.8.2 Balance equations for inflated membranes

Our dome is represented by a thin membrane Γ embedded in $\mathbb{R}^3$. We parametrized this surface by mapping $\boldsymbol{x} = \varphi(\xi)$, where ξ belongs to $\mathbb{R}^2$ and has cartesian coordinates $\{\xi^1, \xi^2\}$. The basis vectors for this surface are defined as:

$$\boldsymbol{e}_a = \frac{\partial \boldsymbol{x}}{\partial \xi^a} \tag{14}$$

, where a ∈ {1,2}. Therefore, we can define a unit vector normal to the surface as the cross-product of these basis vectors normalized by the modulus:

$$\boldsymbol{n} = \frac{e_1 \times e_2}{|e_1 \times e_2|} \tag{15}$$

We can also define the first fundamental form of the surface:

$$g_{ab} = e_a \cdot e_b \tag{16}$$

which provides a way of measuring lengths and angles of vectors in the tangent space and will appear in the next section (Section 3.7.2).

As mentioned previously, the thinness of the membrane allows us to assume that tissue stresses are tangential to Γ. Consequently, its stress state is described by the surface tensor $\boldsymbol{\sigma} = \sigma^{ab} e_a \otimes e_b$. Since Γ is an open surface, the edge tension is given by $\boldsymbol{t} = \boldsymbol{\sigma n_l}$, where n_l is the normal to the edge. For the membrane to be in static equilibrium, the angular momentum must be balanced, meaning that $\boldsymbol{\sigma}$ has to be symmetric. The linear momentum also needs to be balanced in both the tangential and normal directions. In the absence of tangential body forces, the balance in the tangential direction is expressed as[146,147]

$$\boldsymbol{\nabla}_s \cdot \boldsymbol{\sigma} = 0 \tag{17}$$

, where $\boldsymbol{\nabla_s} \cdot ()$ is the surface divergence operator. The balance of linear momentum in the normal direction is given by the Young-Laplace relation:

$$\boldsymbol{\sigma} : \boldsymbol{\kappa} = \Delta P \tag{18}$$

, where κ is the second fundamental form of Γ, which indicates at which rate Γ curves away from its tangent plane at a given point, and ΔP is the pressure difference across the interface. If we know the deformed shape of our membrane in static equilibrium, we can compute **κ**. With κ and the ΔP obtained by a micro-bulge test, we could solve Eqs. (17) and (18) for $\boldsymbol{\sigma}$, because we have a system of 3 equations and 3 unknowns (3 components of a symmetric rank-2 tensor σ). Therefore, the system is statically determinate and we do not need to assume any constitutive relation to infer surface stresses.

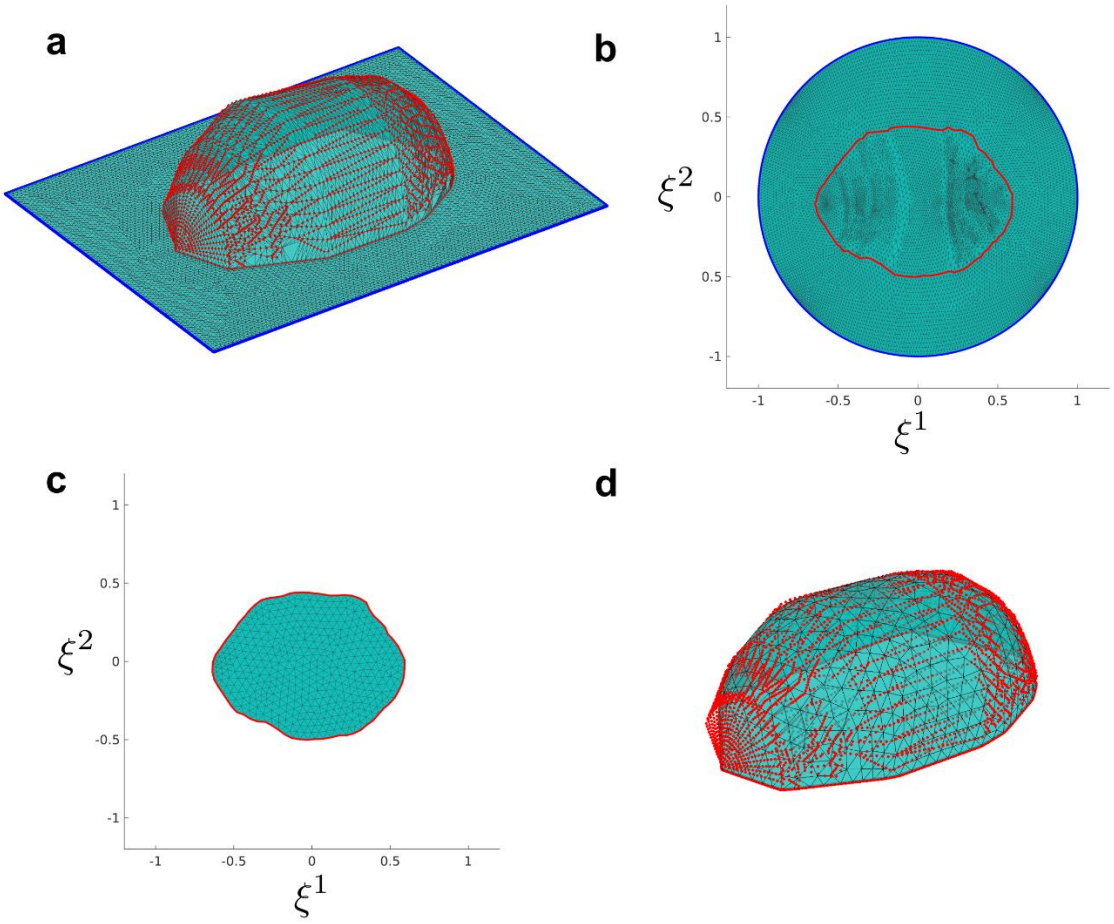

Figure 27: Steps in fitting a smooth surface to the point cloud of epithelial dome basal lumen. *a, A triangulation is generated from the point cloud (red points) to represent the dome surface. This mesh is supplemented by a substrate triangular mesh in the surrounding region. b, The open surface in (a) is mapped on a unit disk using a disc conformal map. The basal footprint of the dome is shown as a red line. c, Re-meshed dome surface in the parametric domain. d, The mesh shown in (c) is fitted to the point cloud (red points) while penalizing the surface gradients to generate a smooth surface fit to the point cloud. This mesh is then used for surface stress estimation. Figure by Sohan Kale.*

3.8.3 Inverse problem formulation for surface stress recovery

The balance Eqs. (12) and (13) can be combined and expressed in vectorial form as[146,147]

$$\frac{1}{\sqrt{g}}\left(\sqrt{g}\sigma^{ab}e_a\right)_{,b} + \Delta P \cdot \boldsymbol{n} = 0 \tag{19}$$

, where $g = det(g_{ab})$.

To obtain the linear equation system necessary for our finite element model, we first need to obtain the weak form of these equations. In weak form, the equations or conditions are not required to hold absolutely and they give a set of trial solutions that are actually closer to the underlying physics. For our system, the weak form can be expressed as:

$$\int_{\Gamma}\left[\left(\sqrt{g}\sigma^{ab}e_a\right)_{,b} + \sqrt{g}\Delta P \cdot n\right] \cdot \boldsymbol{w}\, dS = 0 \tag{20}$$

In this equation we have introduced a weight function, w. This w is an arbitrary function that must be sufficiently smooth to ensure convergence of the finite element method. To obtain the discrete form of Equation (20), we must triangulate the surface Γ to obtain finite elemental domains. For this, we can use a global parametrization to define two vectors $\sqrt{g}(\sigma^{11}e_1 + \sigma^{21}e_2)$ and $\sqrt{g}(\sigma^{12}e_1 + \sigma^{22}e_2)$ at every node of the mesh. Note that the components σ^{11}, σ^{22} and σ^{12} (or σ^{21}, since σ is symmetric) are the 3 unknowns of our system.

First, we use the global parametrization and eqns. (14), (15) and (16) to define e_{I1}, e_{I2}, n_I and g_I at a node I. The surface stresses at this node are denoted as $\{\sigma_I^{11}, \sigma_I^{22}, \sigma_I^{12}\}$. Then, the terms in Eq. (20) can be interpolated as

$$\sqrt{g}\sigma^{ab}e_a(\boldsymbol{x}) = \sum_{I\in E}\left(\sqrt{g}\sigma^{ab}e_a\right)_I N_I \circ \psi^{-1}(\boldsymbol{x}) \tag{21}$$

$$\boldsymbol{n}(\boldsymbol{x}) = \sum_{I\in E} n_I\, N_I \circ \psi^{-1}(\boldsymbol{x}) \tag{22}$$

, where $x = \psi(\chi)$ is the isoparametric mapping for the triangular element and $N_I(\chi)$ are the shape functions for the node I of element E (ref. [148]). These shape functions are used to interpolate the stresses within each element.

In this case (and due to oscillations in the solutions given by the Galerkin approach), we chose a weight function w is constant over each element E as $w = w_e$ (ref. [135]). We can re-write Eq. (18) for every E as

$$\int_{\Gamma_e} \left[\left(\sqrt{g} \sigma^{ab} e_a \right)_{,b} + \sqrt{g} \Delta P \cdot \boldsymbol{n} \right] dS = 0 \tag{23}$$

, where the integration is performed over the element area Γ_e. Using Eqns. (15), (16) and (17) together with the uniform weight function w_e, we obtain a system with 3 equations per element, while every triangular element has 3 nodes. This results in an overdetermined system, which is generally beneficial for ill-conditioned inverse problems, that are sensitive to experimental noise[135].

We perform the integration over each $\Gamma_e$numerically using Gaussian quadrature (using isoparametric mapping of every E). Therefore, the first term of eq. (18) is evaluated as

$$\left(\sqrt{g} \sigma^{ab} e_a \right)_{,b} (\boldsymbol{x}) = \sum_{I \in E} \left(\sqrt{g} \sigma^{ab} e_a \right)_I \frac{\partial N_I}{\partial \boldsymbol{\chi}} \frac{\partial \boldsymbol{\chi}}{\partial \xi^b} \circ \psi^{-1}(\boldsymbol{x}) \tag{24}$$

We combine the unknown stress components into nodal arrays of unknowns $u_I = [\sigma_I^{11}, \sigma_I^{22}, \sigma_I^{12}]^T$, which are then collected in an array $u = [u_1, u_2, \ldots, u_N]^T$, where N is the total number of nodes. We express the overdetermined system of linear equations as $Au = b$, where b is a column vector of size $3N_e \times 1$ (with $N_e$as the total number of triangular elements) and A is a rectangular matrix of size $3N_e \times 3N$.

3.8.4 Regularization

In the membrane tension inference problem, the out-of-plane balance relation in Equation (18) renders the system statically determinate and allows one to directly solve for surface stresses. However, the inverse problem can become ill-posed if the given surface shape cannot support a pressure through a membrane stress (if it is locally planar, for example). Additionally, the solution can be very sensitive to small shape variations, which are inherent to the shape acquisition method. Indeed, we observe that $Au = b$ is ill-conditioned even for simple axisymmetric shapes such as a spherical cap (Figure 28a). Regularization is therefore necessary to solve this inverse problem. This amounts to minimizing the following function with respect to *u*:

$$E(u) = \frac{1}{2}\|Au = b\|^2 + L(u) \tag{25}$$

where $L(u)$ is the discretized regularization contribution that penalizes any undesirable characteristics in the unknown tension field. We considered a first-order regularization of the form:

$$L_{1t}(\boldsymbol{\sigma}) = \frac{\lambda_t^2}{2}\int_\Gamma \boldsymbol{\nabla} trace(\boldsymbol{\sigma}) \cdot \boldsymbol{\nabla} trace(\boldsymbol{\sigma})\, dS = \frac{\lambda_t^2}{2}\int_\Gamma \sigma^a_{a|e}\sigma^b_{b|f} g^{ef}\, dS \tag{26}$$

where the regularization parameter λ_t provides a length scale to penalize tension gradients. Here g^{ef} are the components of the inverse of the metric tensor and $\sigma^a_{a|e}, \sigma^b_{b|f}$ denote the components of covariant derivative of *trace(**σ**)* [147]. This regularization penalizes gradients in the mean surface tension, but it does not necessarily restrain sharp rotations (swirl) in the surface tension field. To regularize such features the following term penalizing the curl of surface tension is introduced:

$$L_{1c}(\boldsymbol{\sigma}) = \frac{\lambda_c^2}{2}\int_\Gamma curl\ \boldsymbol{\sigma} : curl\ \boldsymbol{\sigma}\, dS = \frac{\lambda_c^2}{2}\int_\Gamma \epsilon^{ge}\sigma^{ab}_{|e}\epsilon^{hf}\sigma^{cd}_{|f} g_{ac} g_{bd} g_{gh}\, dS \tag{27}$$

where ϵ is the Levi-Civita tensor[149]. We obtained the discrete version of the regularization terms by using linear elements to interpolate nodal values of surface tension σ_I^{ab} and covariant basis vectors $\boldsymbol{e}_{I1}$ and $\boldsymbol{e}_{I2}$:

$$L(u) = \frac{1}{2}u^T(\lambda_t^2 Q_t + \lambda_c^2 Q_c)u = \frac{\lambda_t^2}{\lambda_c^2}Qu \tag{28}$$

where Q_t and Q_c are the regularization matrices resulting from discretizing $L_{1t}(\boldsymbol{\sigma})$ and $L_{1c}(\boldsymbol{\sigma})$, and $Q = Q_t + \frac{\lambda_t^2}{\lambda_c^2}Q_c$.

The surfaces fit to the experimental point clouds may have regions that are flat (zero Gaussian curvature) or concave (negative Gaussian curvature). Such regions exhibit negative principal tensions that are not compatible with a stable membrane state of stress. The regularization terms considered above do not restrict negative principal tensions. Therefore, to analyse experimental data we additionally impose the following inequality constraint:

$$det\boldsymbol{\sigma}_J = \sigma_J^{11}\sigma_J^{22} - (\sigma_J^{12})^2 > 0$$

for each node *J* when minimizing Equation (25). The minimization problem becomes nonlinear after introducing the inequality constraint and we solved it using the constrained minimization function (*fmincon*) in Matlab.

3.8.5 Validation of the approach with axisymmetric shapes

We tested our method by reconstructing surface stresses on axisymmetric shapes (ellipsoidal caps with a circular boundary). The governing balance equations of these shapes consist of a single ordinary differential equation and, thus, we can compare the results from our model to closed-form solutions. For axisymmetric surfaces, the balance equations (12) and (13) are expressed in the cylindrical coordinate system $r - z$ as:

$$\frac{d\sigma_1^1}{dr} = \frac{1}{r}(\sigma_2^2 - \sigma_1^1) \tag{29}$$

$$\kappa_1^1\sigma_1^1 + \kappa_2^2\sigma_2^2 = \Delta P \tag{30}$$

, where σ_1^1 and σ_2^2 are the principal stress components in the meridian and azimuthal directions, and κ_1^1 and κ_2^2 are principal curvatures in the meridian and azimuthal directions. We quantified the difference between the inferred tension σ and the closed-form solution σ_{CF} at all nodes using the relative error given as $\frac{||\sigma - \sigma_{CF}||}{||\sigma_{CF}||}$. We analysed ellipsoidal caps with an aspect ratio given as $\alpha = r_a/r_b$, where r_a and r_b are the principal radii. For each case, the inverse problem is solved for a wide range of the parameter λ_t, controlling the gradients in tension. Regularisation in the curl of surface tension is also introduced and controlled by the parameter λ_c. This analysis provides guidance to choose the regularization parameters when analysing the membrane shapes obtained in the experiments.

Surface tension recovery for a spherical cap (α = 1) with and without regularisation is shown in (**Figure 28**a,d). The symmetric stress tensor is represented graphically in terms of its mutually orthogonal principal directions of stress (eigenvectors) and principal stresses along these directions (eigenvalues), orthogonal pairs of arrows whose length is proportional to the magnitude of the corresponding principal tensions. In this representation, an isotropic state of stress is represented by two mutually orthogonal pairs of arrows of the same length. The inverse problem is solved for fixed λ_c values and a range of λ_t values. The tension obtained at every node is compared with the expected closed-form solution to quantify the error (**Figure**

28b). With λ_c = 0, the relative error is within 1% for λ_t roughly between 0.002 and 0.1. For λ_t below this range, the problem is under-regularised and, for λ_t above this range, the problem is over-regularized; both cases lead to larger errors. Introducing the curl-based regularization with λ_c is observed to further improve the overall recovery of surface tensions (**Figure 28**b). For each λ_c, the λ_t value corresponding to the minimum error can be associated with the corner in the L-curve, where the regularization term is plotted against the residual forces (**Figure 28**c).

In spherical caps, the curvature is constant. However, other axisymmetric shapes, such as ellipsoidal caps, present significant curvature gradients. This curvature gradients imply the

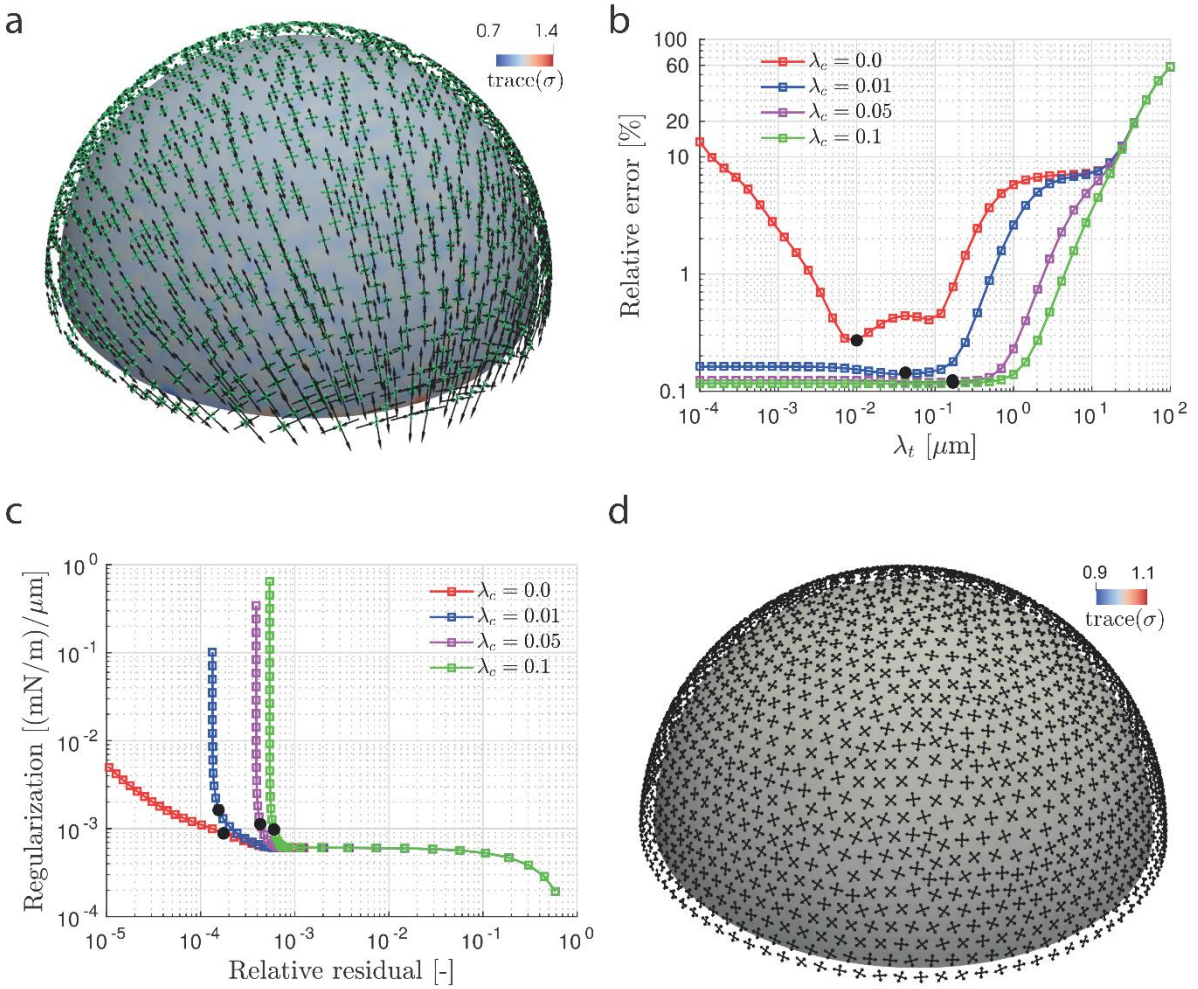

***Figure 28: Effect of regularization on surface tension inference on a spherical cap**. a, Membrane stress inference on a spherical cap without any regularization. The black arrows represent the inferred membrane stresses and green arrows represent the expected solution for a spherical cap. b, The inverse problem solution is analysed as a function of the regularization parameter λ_t for λ_c = {0.0,0.01,0.05,0.1}. The relative error between the inferred tension and the closed-form solution is sufficiently low (<1%) for a wide range of λ_t values that depend on the choice of λ_c. c, Regularization functional plotted against the residual, in the so-called L-curve. The corner in the L-curve corresponds to the optimal regularization parameter λ_t for a given λ_c. d, Representation of the surface stress obtained for λ_c = 0.1, where the stress tensor is represented in terms of its mutually orthogonal principal directions of stress and principal stresses as discussed in the text. The colour map represents the trace of the surface stress. Figure by Sohan Kale.*

existence of tension gradients. Using a high value of λ_c in such a case might overly-penalize the tension gradients leading to larger errors. Therefore, the choice of λ_c is dependent on the surface, and a smaller value should be used when significant tension gradients are expected in the solution. This is also the case of our experimental data, where we estimate the optimal λ_c parameter based on curves such as the one depicted in (**Figure 28**c).

3.9 Dome segmentation

3.9.1 Nuclei segmentation and analysis

The segmentation of nuclei was performed using Imaris 9.7 (Oxford Instruments). We imported the z-stacks containing the nuclei fluorescence into Imaris and we obtained the nuclei surfaces by using the "Surfaces" algorithm "with "Surface Grain Size" = 0.5 µm and "Region Growing Estimated Diameter" = 5.8 µm. The resulting 3D point clouds were exported in ".wrl" format and read in Matlab. Then, we fitted an ellipsoid to each nucleus point cloud using the function "ellipsoid_fit"(ref. [150]). Using Matlab home-made analysis software, we extracted the relevant geometrical information from each ellipsoid: centroid coordinates and length and direction of the 3 radii.

To analyze the effect of stress on nuclear shape, we plotted the ellipsoids on top of the stress field computed using the theoretical model. We compared the main direction of the stress field with that of the longest radii of the nuclei.

3.9.2 Cell segmentation and analysis

Cellular segmentation was carried out with Cellpose, a Python-based cell segmentation plugin[151]. For each dome, the z-resolution was downsampled to 1.5 µm and the cells in each 2D confocal slice were automatically segmented using an estimated diameter of 100 pixels (**Figure 29**a). We then corrected the segmentation manually. Corrections were essentially needed in the middle planes of the dome, due to the cells being very elongated and thin, making detection by the algorithm very difficult.

Afterwards, we stored the 2D segmentations as ".png" images and we processed them in Matlab using home-made analysis software. We re-labelled the cells in each plane to create

a 3D reconstruction. For this purpose, we created an algorithm that computed the intersection over union (iou) of cells in consecutive z planes and labelled them as the same cell if the iou was greater than a given threshold (0.5 in the lower planes and 0.3 in the upper ones, **Figure 29**b). We then fitted an ellipsoid to the resulting cell masks and extracted the radii lengths and directions. To analyze the effect of stress on cellular shape, we projected the ellipsoids on top of the stress field computed using the theoretical model (**Figure 29**c). We compared the main direction of the stress field with that of the longest cell radius.

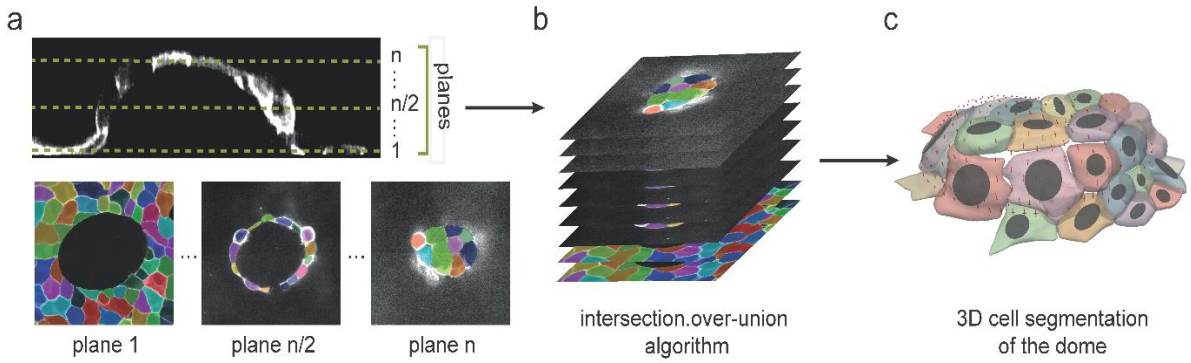

Figure 29: Cell segmentation. *a, Confocal images from elliptical domes with 1.5 µm vertical spacing were independently segmented using Cellpose (ref.[151]). Segmentations were manually curated. b, All segmentation planes were stitched using a custom intersection-over-union (iou) algorithm to obtain 3D cell segmentations. c, We fitted ellipsoids to the cells and projected them on the dome surface (grey ellipses). We compared the longest cell axis with the maximal stress direction in the free-standing monolayer (red arrows).*

3.10 Statistical analysis

For rectangular domes (results in Section 4.3), comparisons between each group of unpaired samples were computed using the unpaired two-sided Wilcoxon rank sum test in R ("wilcox.test" function). Comparisons between groups of paired samples (long vs short sides in rectangular domes) were computed using the paired two-sided Wilcoxon rank sum test.

For cell and nuclei orientation data (results in Section 4.4), the median of α distributions was compared to that of 10000 uniform MATLAB-generated distributions with the same size as the data. P-value was calculated as the number of times the median of a random uniform distribution was below that of our distribution. Eccentricity data was compared using the unpaired two-sided Wilcoxon rank sum test in R.

95% confidence intervals of the median were computed using bootstrap (package *boot* in R).

4 RESULTS

4.1 New protocol to generate curved epithelia of controlled size and shape

In this project, we aimed to measure the mechanical properties of curved MDCK epithelia of controlled shape, and sizes ranging between 25 and 200 µm diameter. These curved epithelia, that I will hereafter refer to as domes, form after seeding of MDCK cells on a 3 kPa PDMS impermeable substrate, which is compatible with TFM experiments. In our previous protocol, the cells attached to the substrate, that was coated with fibronectin except for micropatterned non-adhesive areas with our desired geometry, and invaded the non-adherent areas a few hours after seeding[54]. However, this invasion was limited to small regions with a diameter smaller than 150 µm and specific geometries (we could not generate tubes or toroids, for example). Therefore, we decided to create a new method to generate domes with a broader range of sizes and shapes.

The protocol is detailed in the Methods chapter (Sections 3.2 and 3.3). Briefly, after coating our soft PDMS with fluorescent beads that allow TFM, we incubated the substrates with PLL and mPEG-SVA, successively. These incubations led to a layer of PEG chains that avoided cell attachment to the substrate. Next, we photopatterned the substrate to create low fibronectin motifs surrounded by high fibronectin areas. This process was performed by adding the

photoinitiator molecule, which cut the PEG chains upon UV stimulation with the PRIMO system (Alvéole)[139], and subsequently incubating the samples with fibronectin. MDCK cells attached to low and high fibronectin areas and formed a flat monolayer. After several hours, the monolayer started to delaminate on the low-adhesion areas and formed pressurized fluid-filled lumens, due to MDCK cells pumping osmolytes in the apicobasal direction (**Figure 30**).

We optimized the protocol to increase the number of successful domes. To do so, we identified two key parameters that greatly influenced dome formation: photopatterning illumination level and incubation time after seeding. This illumination level (represented by the brightness of the input ".pdf" patterns) affects dome formation, because too much illumination leads to indiscriminate delamination through the sample, and too little illumination leads to no invasion of the low-adhesion areas. The incubation time of the cells after seeding affects the state of the domes we image. For the smallest domes (25 µm-diameter), 16 hours of incubation sufficed to generate the structures, and, after 24 hours, domes already started to delaminate outside of the pattern. However, the largest domes (200 µm-diameter) required around 48 hours to form a cohesive monolayer on the low-adhesion area and start inflating.

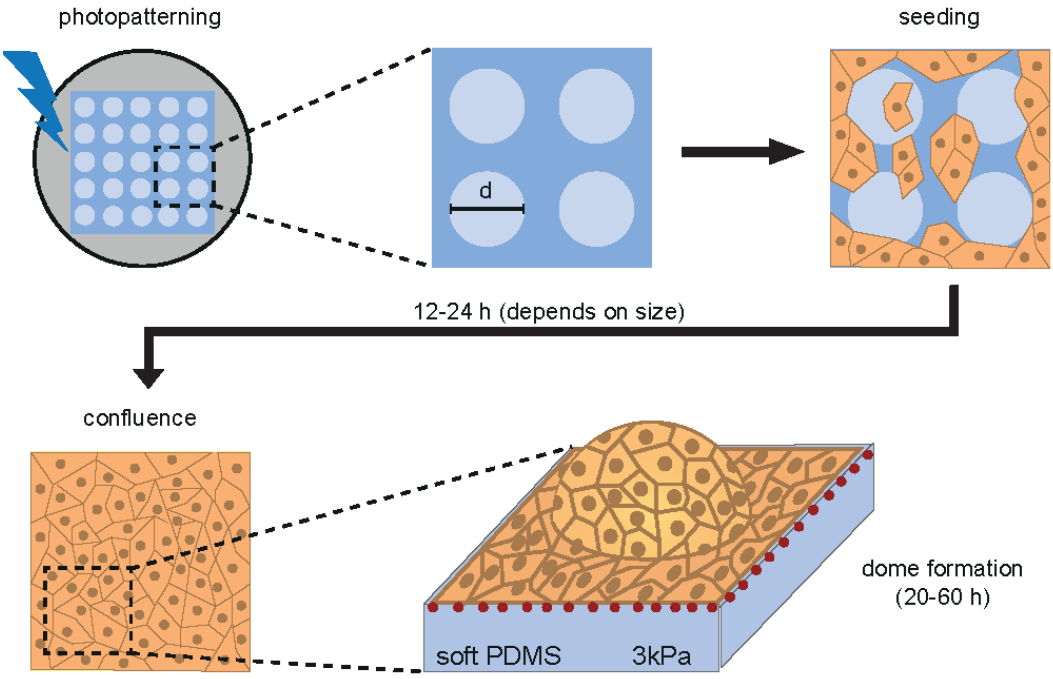

Figure 30: Protocol to generate curved epithelia of controlled size and shape. *Passivated soft PDMS gels are photopatterned using the PRIMO system in the presence of a photoinitiator molecule. The gel is differentially illuminated to create low adhesion motifs with diameter* d *(light blue circles) surrounded by high adhesion areas (dark blue). Cells are then seeded on the substrate, and they attach to both low- and high-adhesion areas. After 12-24h, the cells form a confluent monolayer. Between 20 and 60h post-seeding, domes form in the low-adhesion regions. The incubation time needed for cell confluence and dome formation depends on* d*.*

4.2 Size effect on mechanics of pressurized spherical domes

Upon optimization of the protocol, we first studied the effect of size on the mechanics of domes with circular footprints (micropatterned motifs) of 25, 50, 100 and 200 µm-diameters. We would like to remark that, except a few 25 µm domes, all other domes presented a perfectly circular basal area and a spherical cap morphology. The 25 µm domes that presented irregular geometry were excluded from the analysis. Domes displayed a similar cell density across all sizes (**Figure 31**), which remained constant through the experiment (division rarely occurs in inflated domes).

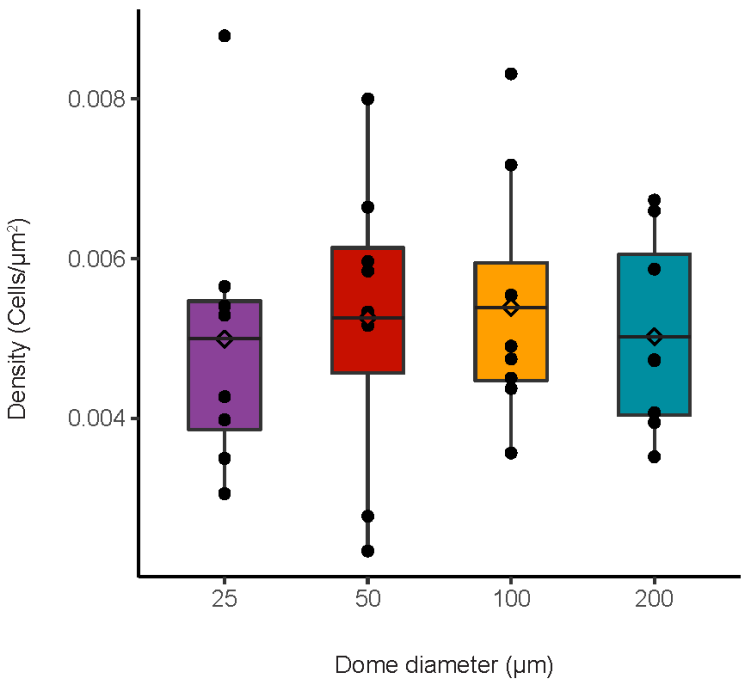

Figure 31: Cell density in domes of different sizes. *Density of cells in MDCK domes with 200, 100, 50 and 25 µm pattern diameter. Data are shown as median ± std of n=8 (for all cases).*

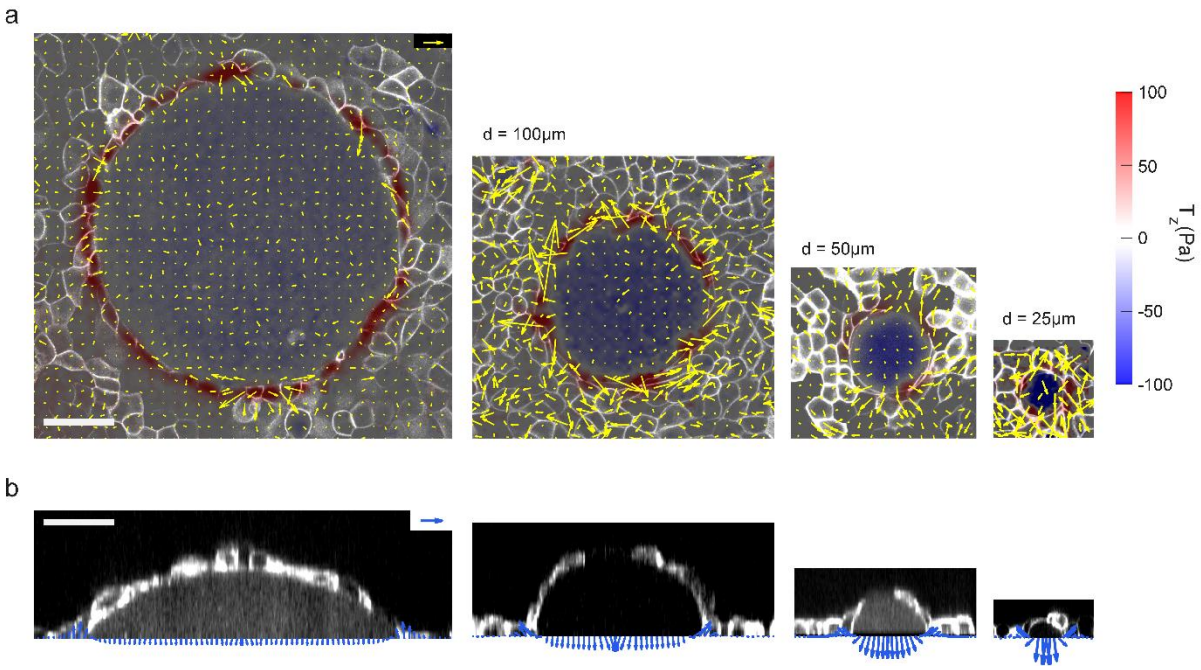

Figure 32: Scaling of tension and pressure in spherical domes. *a, 3D traction maps overlaid on top views of representative MDCK domes of 200 µm, 100 µm, 50 µm and 25 µm pattern diameters (from left to right). Yellow vectors represent in-plane horizontal components T_x and T_y and the colour map represents the vertical component T_z. b, Tractions overlaid on lateral*

views of the domes shown in (a). Tractions were averaged circumferentially for plotting. Scale bars: 50 µm. Scale vectors: 100 Pa.

Using traction force microscopy (TFM), we mapped the 3D forces exerted by the dome on the substrate, both below the lumen and at the dome-substrate boundary. Below the lumen, the traction vectors pointed uniformly downwards, indicating that the lumen was pressurized. The magnitude of these vectors is a direct measure of luminal pressure (ΔP). This pressure was balanced at the dome-substrate boundary, below the first row of cells adhered to the gel, where the vectors pointed upwards. The direction of the vectors was not tangential to the dome, as we would expect if the dome was the only structure exerting forces, thus suggesting that the surrounding adhered monolayer contributes to the mechanical equilibrium at this point (**Figure 32**).

Domes are dynamic structures, and they inflate and deflate spontaneously (**Figure 33**). These processes are usually progressive, and noticeable changes in volume may take a few hours, but deflation can also occur swiftly due to loss of local cell-cell adhesion (for example, when a cell enters mitosis). This dynamic nature of domes allowed us to measure luminal pressure for epithelial curvatures encompassing more than one order of magnitude (**Figure 34**a). For lower curvatures (that correspond to the bigger domes), pressure increased linearly with curvature. However, it tended to plateau at high curvatures, suggesting a limit to the pressure that MDCK can spontaneously build up.

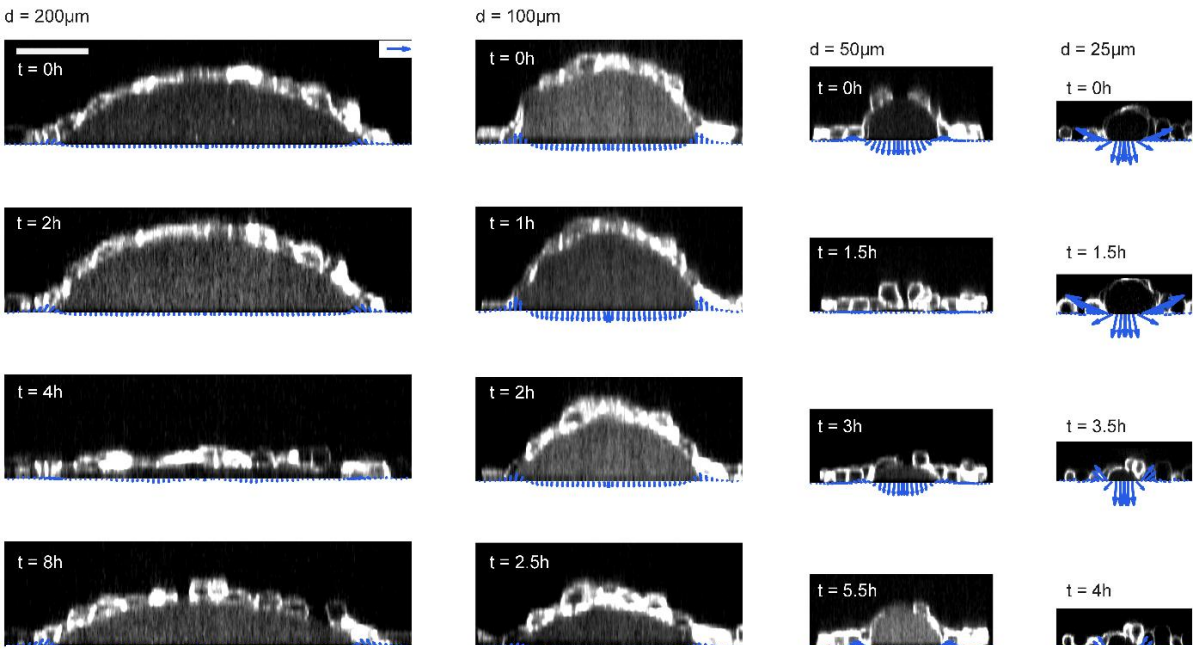

Figure 33: Time evolution of domes of different sizes. *Time evolution of radially-averaged tractions on lateral views of domes of 200, 100, 50 and 25 µm diameter patterns. Blue arrows represent the radial and vertical components of the tractions. Scale bar: 50 µm. Scale arrows: 100 Pa.*

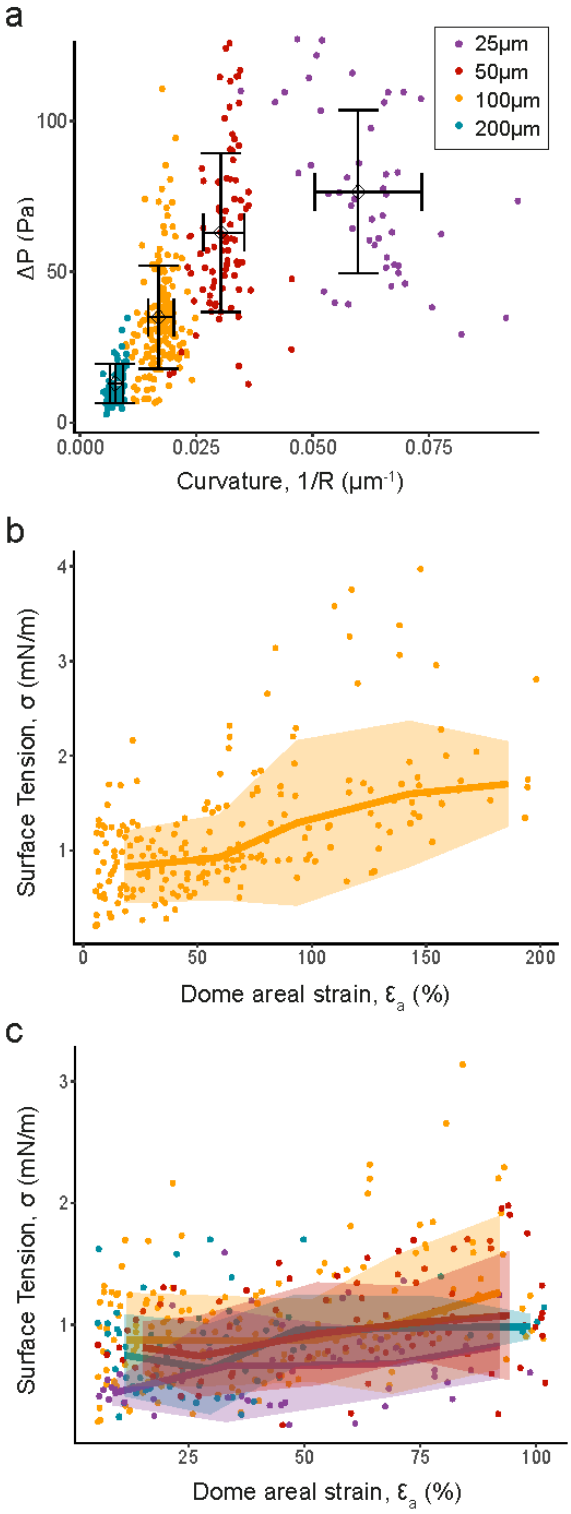

***Figure 34: Pressure and tension in spherical domes**. a, Dome pressure as a function of dome curvature. Data shown as mean ± std of n=12 domes (25 µm), 11 domes (50 µm), 17 domes (100 µm) and 13 domes (200 µm) at different levels of inflation. Colour coding indicates the footprint diameter. b, Surface tension in the free-standing sheet as a function of nominal areal strain of 100 µm-diameter footprint domes. c, Surface tension in the free-standing sheet as a function of nominal areal strain of the dome. Number of domes is the same as in (a). The line and shaded area indicate median and std by binning the data (equally spaced bins with n ≥ 3 points per bin).*

Afterwards, we inferred the stress on the dome. To do so, we used the Young-Laplace equation $\sigma = \Delta P \cdot R/2$, where R is the radius of the dome at half-thickness of the monolayer. We then studied how σ changes with the inflation level of the dome, which we quantified using the areal strain, ε_a. We first observed the behaviour of domes with a 100 µm-diameter footprint, and we found that the results were consistent with the superelastic behaviour previously observed in Latorre *et al*[54]. σ increased with ε_a at low strains and plateaud at high strains (**Figure 34**b). Due to limitations in the inflation of the largest domes, we focused the study of size effects on the range ε_a < 100% (**Figure 34**c). The data was highly scattered, with values for median and standard deviation on the same order of magnitude. Upon averaging of the data, we observed that the stress-strain curve presented a behaviour consistent with superelasticity at low ε_a independently of footprint size. This suggests that, within the range studied here, curvature does not trigger mechanosensing feedback loops that affect the magnitude of epithelial tension.

Upon close examination of dome fluorescence images, we noticed that the apical cell-cell contact angles were substantially smaller than the basal ones, indicating higher basal than apical surface tension (**Figure 35**a). This difference could generate a bending moment that could contribute to the mechanical balance of luminal pressure and lead to inapplicability of

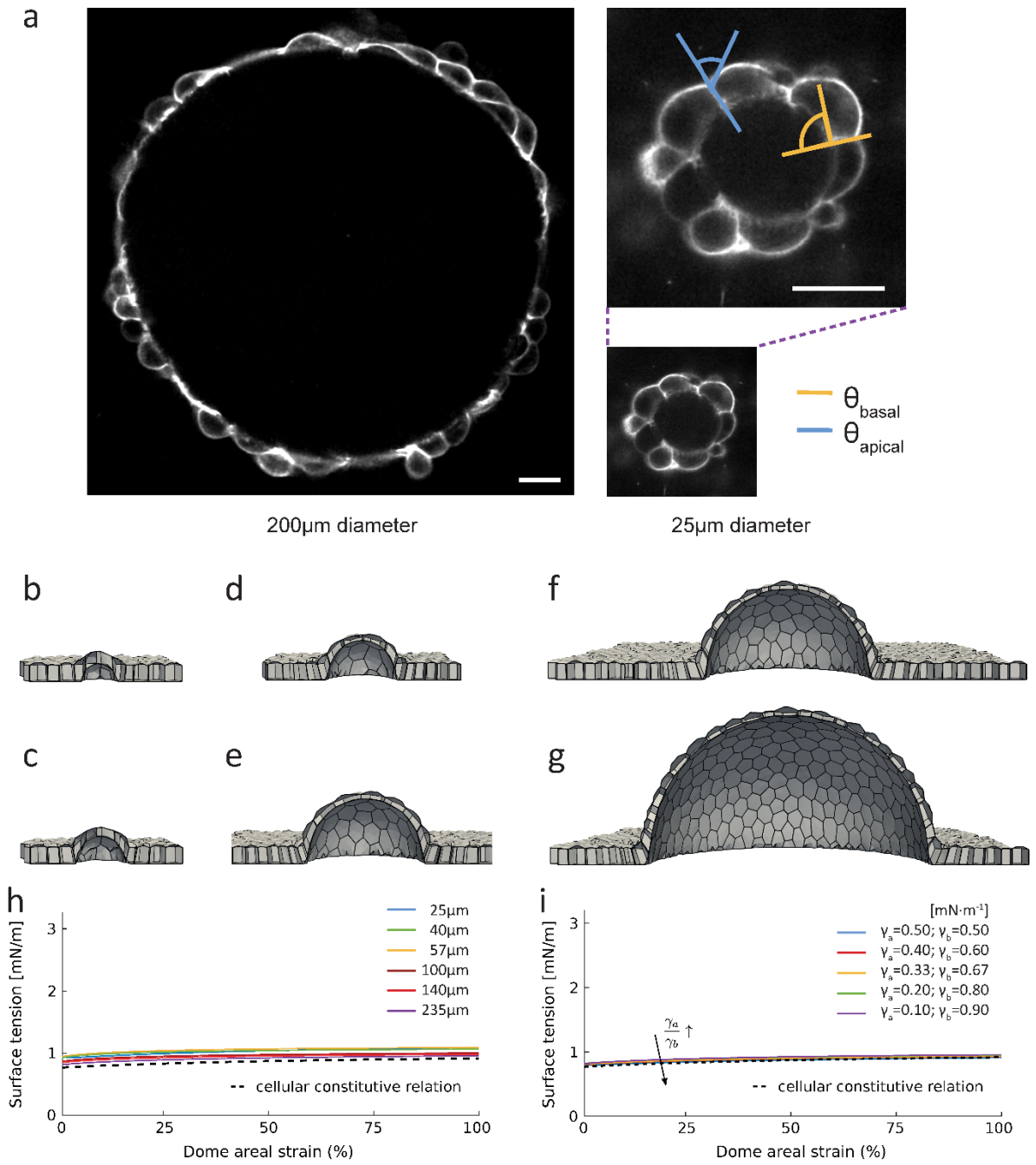

Figure 35: Surface tension measured in computational vertex model simulations shows negligible differences between different dome sizes*. a, Confocal slices of 200 and 25 µm footprint domes showing the apical and basal contact angles between cells. b-g, Cross-sections of domes with different basal footprint sizes at 100% areal strain ε_a and 1:9 apical-to-basal surface tension ratio. h, Surface tension as function of ε_a for the different dome basal footprint diameters. The black curve shows the cellular constitutive equation in Eq. (13). i, Surface tension as a function of strain at different apical-to-basal surface tension ratios for the dome shown in (g).γ_l = 0.1 mN/m for all curves. Scale bar: 20 µm. Panels (b-i) courtesy of A. Ouzeri.*

Laplace's law. To discard this possibility, our collaborators Adam Ouzeri and Prof. Marino Arroyo simulated domes with different sizes and apical-to-basal tension ratios using a 3D vertex model (see Section 3.7). For domes with footprint diameters ranging between 25 and 235 µm, and an apical-to-basal surface tension ratio of 1:9, all domes presented very similar surface stresses regardless of size (**Figure 35**b-h). To further confirm that the differential apico-basal tension did not affect tissue stress significantly, we simulated large domes with different apical-to-basal tension ratios, ranging between 1:9 and 1:1 (**Figure 35**i). The results showed that the contribution of this tension ratio was negligible, with the stress curve collapsing to the cellular constitutive equation for the symmetric (1:1) case. These computations highly resembled the experimental results, thus supporting that the stress of the free-standing monolayer was mostly unaffected by size and bending moments.

4.3 Stress in anisotropic domes

Even though there are remarkable examples of spherical lumens, such as the blastocyst, most physiologically relevant lumens present an asymmetric geometry. Consequently, after examining the effect of size on the mechanics of luminal epithelia, we wanted to assess the effect of shape. Given that the Young-Laplace's equation cannot be applied to non-axisymmetric structures, we sought to develop a method to map the stress tensor in a monolayer of arbitrary geometry.

For this purpose, our collaborator Prof. Sohan Kale developed a surface stress recovery method based on membrane theory that infers stresses from dome shape and luminal pressure, without assumptions of material properties. For this model, we profited from one of the main characteristics of our domes: the thickness of the cell layer is more than one order of magnitude smaller than the width and length of the dome. Since the thickness of the sheet is sufficiently small in comparison with the other dimensions, it can be modelled as an inflated membrane and stresses can be inferred from monolayer shape and luminal pressure measurements (see Section 3.8 for detailed information).

Afterwards, we applied this inference method to domes with anisotropic geometries, specifically domes with rectangular and elliptical footprints.

4.3.1 Stress in domes with rectangular cross-sections

First, we photopatterned substrates with rectangular footprints of the same area, but different aspect ratios: 1:1 (square), 1:2 and 1:4. These epithelia delaminated from the substrate in the same way as spherical domes, and formed tubes and caps with fluctuating inflation levels (**Figure 36**a). We then inferred the principal stresses in the dome. For square footprints, the stress was isotropic and uniform at the upper part of the dome (that resembled a spherical cap) and became anisotropic close to the dome-substrate interface, particularly at the corners. For rectangular footprints, the principal stresses were anisotropic. Their directions generally coincided with the axes of the rectangle, and the component parallel to the short axis was larger than the one parallel to the long axis (**Figure 36**b).

To validate the computational predictions, we compared them to the experimental tractions at the dome-substrate contact. We reasoned that the component tangential to the monolayer, $T_{//}$ (**Figure 36**c), should match the predicted stresses at this point. We examined the experimental values of $T_{//}$ as a function of footprint aspect ratio and dome inflation. As anticipated, the tractions were similar in all sides of a square, and they increased with inflation. For rectangles, $T_{//}$ still increased with inflation, but it was higher at the long sides with respect to the short ones (**Figure 36**d). To compare the experimental results with the predicted stresses, we converted stresses to tractions using a length-scale of 17 µm. This length-scale was approximated by choosing the factor that minimized the difference between experimental and theoretical data. Inferred data from squares was again symmetrical, and rectangles presented higher $T_{//}$ along the long sides (**Figure 36**e). These data show a close agreement between the inferred and measured stresses at the boundary between the dome and the flat monolayer, thus supporting the validity of this stress inference method.

Figure 36: Stress in domes with squared and rectangular cross-section*. a, Traction maps of rectangular domes with different aspect ratios (from left to right, 1:1, 1:2 and 1:4 aspect ratios) and inflation levels (low inflation, top row; high inflation, bottom row). Each one of the six panels comprises a top view (left) and two lateral views (right and bottom). The top view shows a 3D traction map, where yellow vectors represent the in plane (*Tx, Ty*) components and the colour map represents the vertical component* Tz*. The lateral views show the tractions averaged over the central segment of the vertical and horizontal sections of the dome. Scale bar: 50 µm. Scale vectors: 100 Pa. b, Inferred stress tensor across the free-standing cell layer of the domes shown in (a). c, Scheme illustrating the definition and calculation of the tangential component to the dome, $T_{//}$. d, Experimental tangential tractions at the short and long sides of domes with low and high inflation levels. The tractions have been averaged along the central 50% of the dome sides. Data are shown as median ± std of n=53 (square low), 35 (square high), 50 (rect. 1:2 low), 30 (rect. 1:2 high), 69 (rect. 1:4 low), 29 (rect. 1:4 high). e, Predicted tangential tractions at the short and long sides of domes with low and high inflation levels obtained with our stress inference method. The tractions have been averaged along the central 50% of the dome sides. Data are shown as median ± std of n=11 (square low), 12 (square high), 14 (rect. 1:2 low), 12 (rect. 1:2 high), 9 (rect. 1:4 low), 15 (rect. 1:4 high). Statistical significance was determined using the Wilcoxon rank sum test for paired and unpaired samples. Only statistically different pairwise comparisons are indicated. d, Left: P = 0.003 (vertical) and P = 0.014 (horizontal). Middle: P = 0.011 (low-short vs high-short), P = 1.5e-08 (low-*

*short vs low-long), P = 4.7e-08 (high-short vs high-long) and P = 0.002 (low-long vs high-long). Right: P = 5.9e-07 (low-short vs high-short), P = 4.7e-10 (low-short vs low-long), P = 2.6e-07 (high-short vs high-long) and P = 1.4e-04 (low-long vs high-long). e, Left: P = 0.032 (vertical). Middle: P = 2.4e-04 (low-short vs low-long) and P = 4.9e-04 (low-long vs high-long). Right: P = 3.9e-03 (low-short vs low-long) and P = 5.4e-03 (low-long vs high-long). *P < 0.05, **P < 0.01 and ***P < 0.001.*

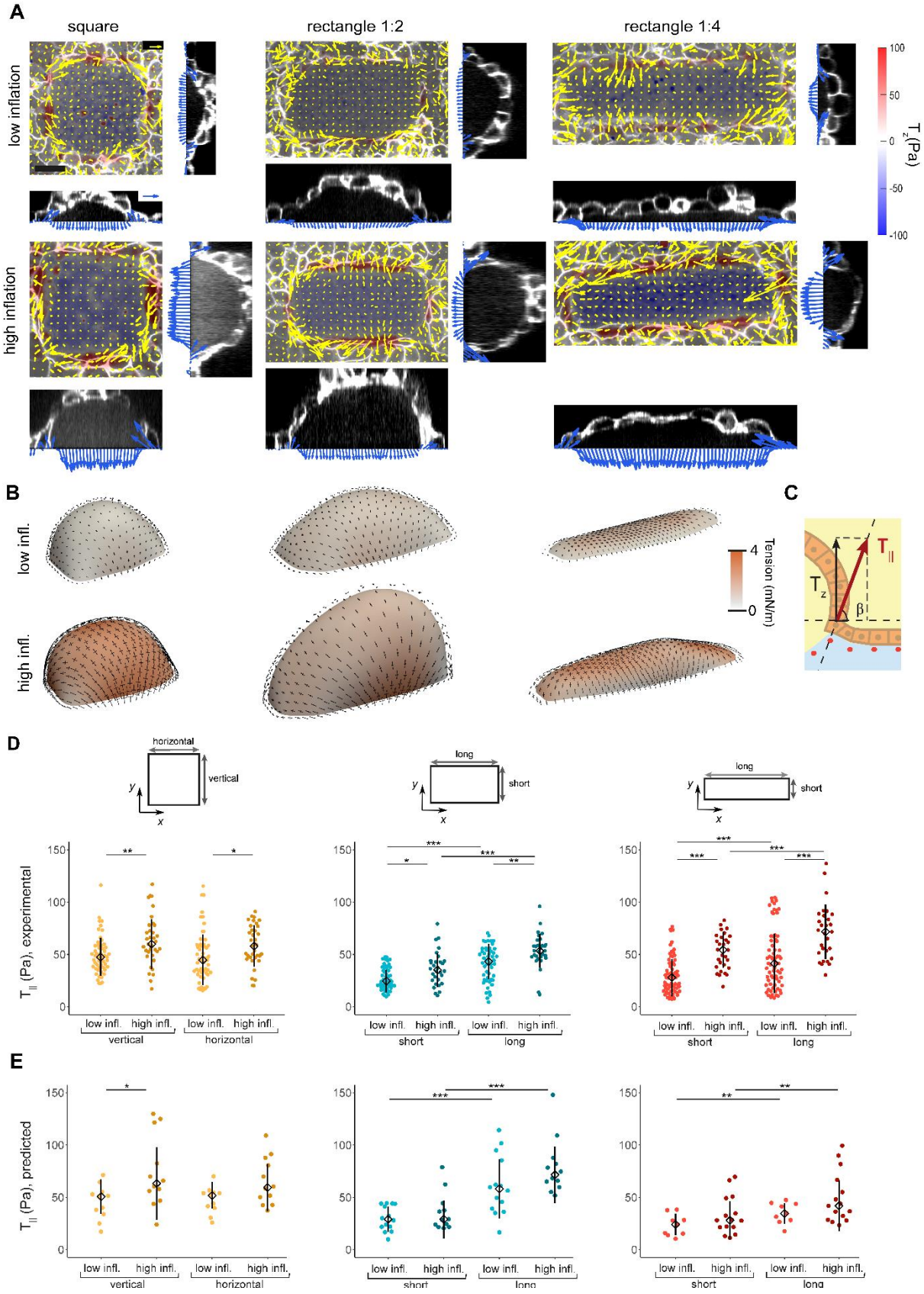

4.3.2 Stress in ellipsoidal domes

We then sought to study the effect of curvature on stress. For this purpose, we generated domes with an elliptical footprint and two different aspect ratios (1:2 and 1:3) and inferred the surface stresses with our model (**Figure 37**a,b). Again, we observed that the principal

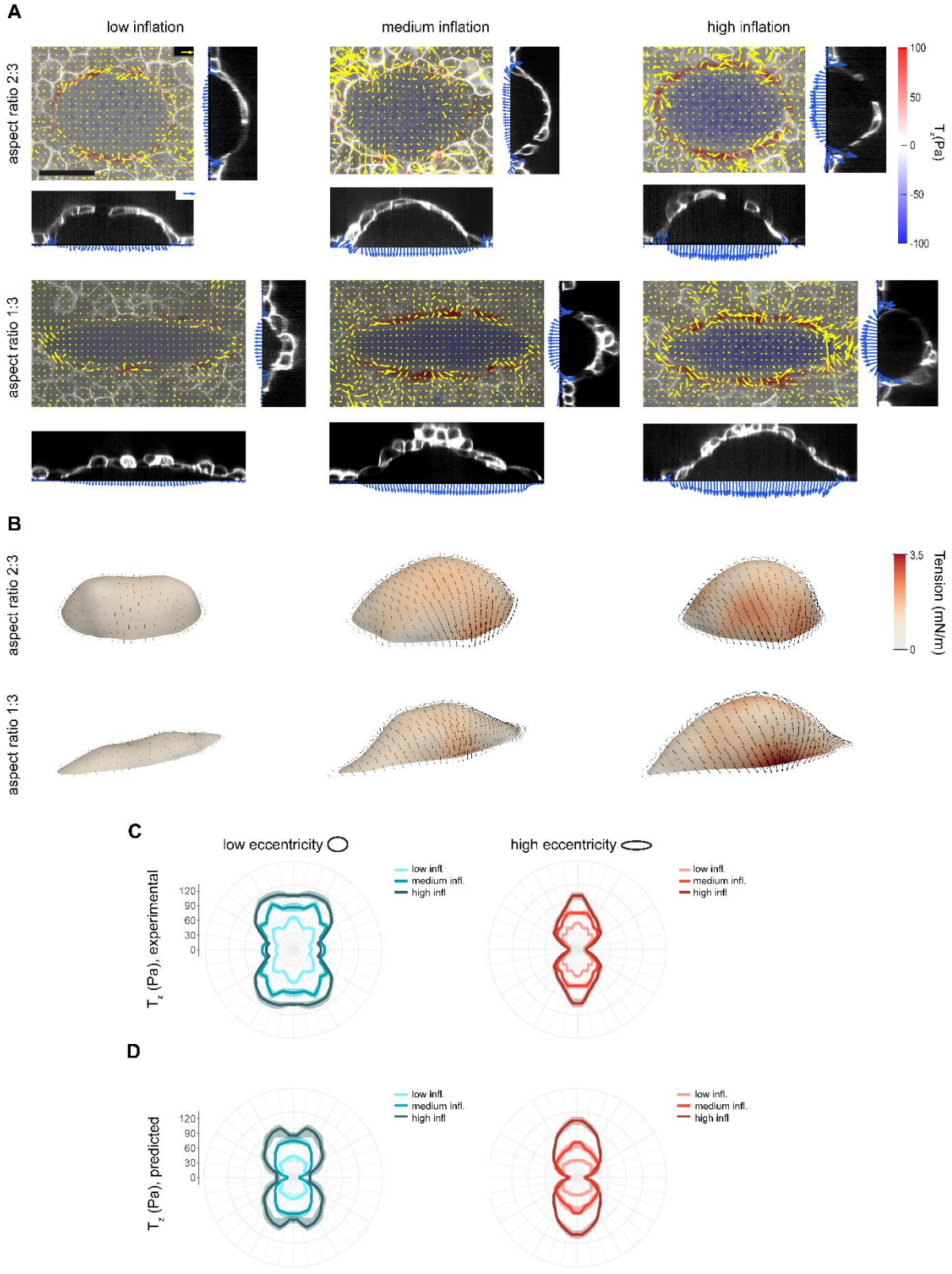

Figure 37: Stress in ellipsoidal domes. *a, Traction maps of ellipsoidal domes with different aspect ratio (2:3 top and 1:3 bottom) and inflation levels (from left to right). Each one of the six panels comprises a top view (center) and two lateral views (right and bottom). The top view shows a 3D traction map, where yellow vectors represent the in plane (T_x, T_y) components and the color map represents the vertical component T_z. The lateral views show the tractions averaged over the central segment of the vertical and horizontal sections of the dome. Scale bar: 50 µm. Scale arrows: 100 Pa. b, Inferred stresses across the free-standing cell layer of domes shown in (a). c, Experimental vertical tractions at the dome-substrate interface for low, medium and high inflation levels. Left: low eccentricity. n=15 (low), 30 (medium), 16 (high). Right: high eccentricity. n=11 (low), 16 (medium), 23 (high). The tractions have been averaged in the four quadrants using the symmetry of the system (methods). d, Predicted vertical tractions at the dome-substrate interface for low, medium and high inflation levels obtained with our surface stress inference method. Left: low eccentricity. n=7 (low), 9 (medium), 8 (high). Right: high eccentricity. n=7 (low), 8 (medium), 8 (high). The tractions have been averaged using the symmetry of the system. The line and shaded area indicate median and 95% CI of the median by bootstrapping the data.*

stresses were anisotropic, and their directions coincided with the axes of the ellipse, with the component parallel to the short axis being larger. We then studied the values of the tractions at the dome-substrate contact as a function of the polar angle along the ellipse. Since the calculation of $T_{//}$ for very small angles (<10 degrees) was inaccurate due to the noise inherent to TFM ([a]), we analyzed T_z, the component vertical to the substrate.

For domes with low inflation level, T_z was low and mildly anisotropic, with higher tractions at the low curvature regions. With increasing inflation levels, the tractions increased and became more anisotropic. This behavior was more pronounced in more eccentric domes (**Figure 37**c). Next, we compared the experimental tractions with the predictions of our model (using again a length-scale of 17 µm). The inferred T_z matched qualitatively the experimental results, with more pronounced anisotropy in high inflation levels and high eccentricity **(Figure 37**d).

4.4 Effect of stress on geometry and orientation of cells and nuclei

Finally, we asked whether the inferred local stress was predictive of the shape and orientation of cells and nuclei.

4.4.1 Cellular orientation and shape

We started with the analysis of cellular orientation. We first created three-dimensional masks of the cells in ellipsoidal domes with the aforementioned aspect ratios (**Figure 38**a). We then

[a] Tangential traction data, $T_{||}$, for ellipsoidal domes is available on 8.1Appendix 1.

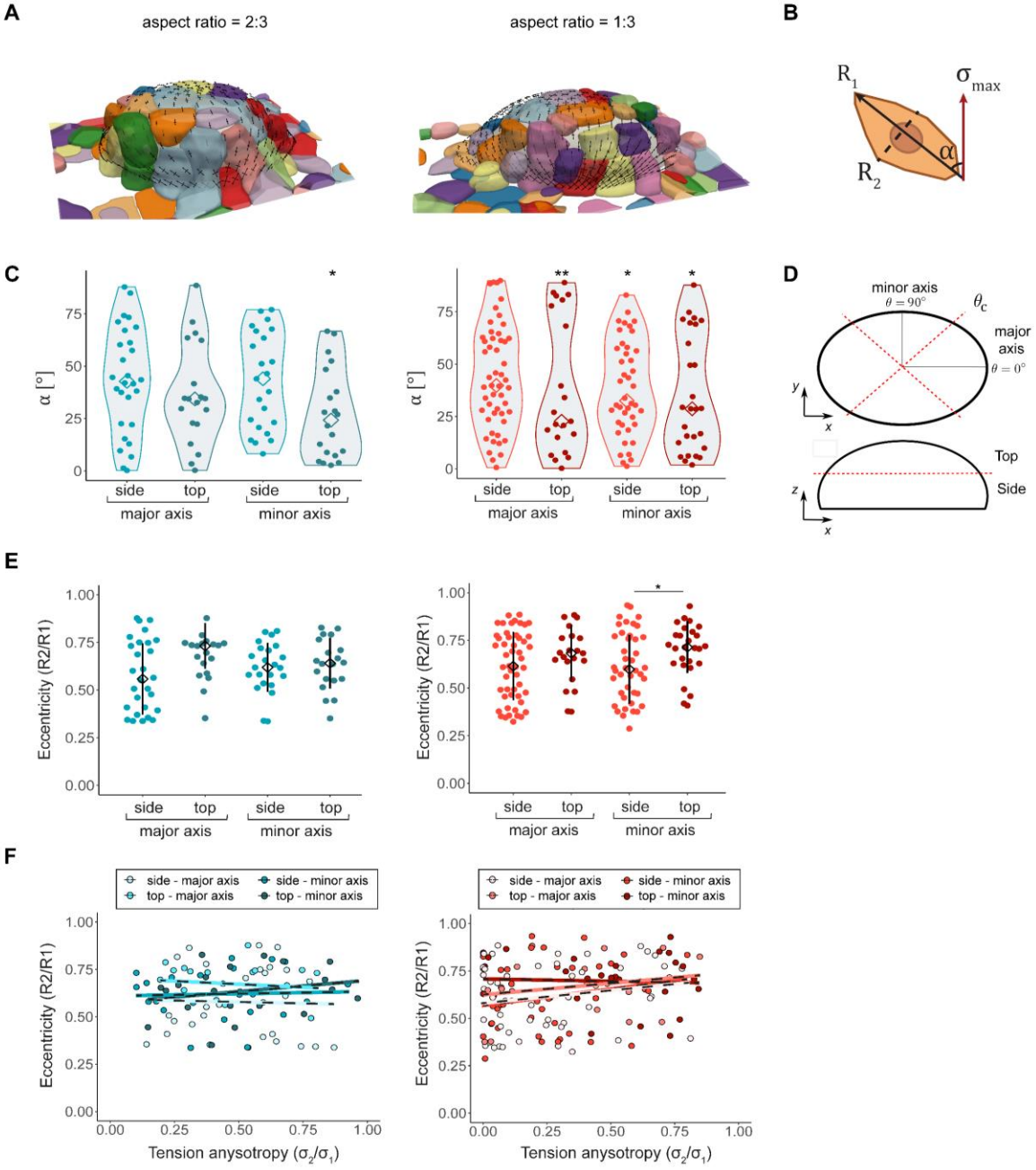

Figure 38: Relationship between stress and cell geometry in anisotropic domes*. a, Segmented cells on top of high inflation ellipsoidal domes with 2:3 (left) and 1:3 (right) aspect ratio. The red arrows represent the principal components of the inferred stress. b, Schematic showing the calculation of angle* α *between the longest cell axis (*R_1*) and the direction of the maximum principal stress (*σ_{max}*). c, Distribution of angles* α *for the different regions of highly inflated domes. Statistical significance was determined by comparing the median between each distribution and 10000 randomly generated uniform distributions with the same n. d, Schematic indicating the different dome regions in which cells were classified. e, Cell eccentricity computed as the ratio between the second longest axis (*R_2*) and the longest axis (*R_1*) of the cells shown in (c). Data are shown as median ± sd. f, Relationship between cell eccentricity and tension anisotropy of the cells shown in (c). Lines represent a linear fit of the data. n=28 (major side, left), 19 (major top, left), 23 (minor side, left), 20 (minor top, left), 51 (major side, right), 45 (major top, right), 42 (minor side, right), 33 (minor top, right). c, Left: P = 0.011. Right: P = 6.2e-03 (top-major axis), 0.034 (side-minor axis), 0.022 (top-major axis). e, Statistical significance was determined using the Wilcoxon rank sum test for unpaired samples. Only statistically different pairwise comparisons are indicated. P = 0.04. *P < 0.05 and **P < 0.01.*

fitted the shape of each cell to an ellipsoid and projected it on the surface of the segmented dome. We computed the angle α between the longest cell axis and the direction of the local principal maximum stress (**Figure 38**b). We plotted the distribution of α for low and high eccentricity domes with high inflation level. Data was binned according to the position of the cell in the dome (top vs side, and major vs minor regions, **Figure 38**c,d). Analysis of these distributions showed that cell alignment increased with dome eccentricity. Cells located on the side-minor axis and the top regions were strongly aligned with the maximum principal stress in more eccentric domes, while only cells on the top-minor region were aligned in the less eccentric cases. Higher dome eccentricity resulted in higher anisotropy of the stress field, so we hypothesized that there may be a dependence between cell alignment and local stress anisotropy. However, the results did not show any correlation ([b]). In less inflated domes, the alignment was not significant in any of the regions ([c]).

We next analyzed cellular shape. To do so, we computed the ratio of the shorter and longer diameters of the projected ellipses (R_2/R_1) for the four previously mentioned regions (**Figure 38**e). We found that this ratio oscillated between 0.3 and 0.85, which indicated a coexistence of very elongated cells with regular-shaped ones. Generally, cells were more elongated (lower ratio value) at the side regions of the dome than at the top regions. However, these differences were mostly not significant. To check whether local anisotropies on the stress field could explain this diversity of cell shapes, we plotted the cell shape ratio R_2/R_1 with respect to the local stress anisotropy, computed as the ratio between the second and first largest components of the maximum principal stress (σ_2/σ_{max}). These differences in cell morphology, did not correlate with a higher anisotropy of the stress field (**Figure 38**f).

4.4.2 Nuclei orientation and shape

Finally, we analyzed the orientation and morphology of cellular nuclei. We first generated three-dimensional masks of nuclei in elliptical domes (**Figure 39**a). We projected the masks onto 2D ellipses on top of the dome segmentation to estimate the local principal stresses at the position of the nuclei. We then computed the angle α between the longest nucleus axis

[b] Data on "Cell alignment versus local stress anisotropy" can be found on **Appendix 2**.
[c] Data on "Relationship between stress and cell geometry" for low inflation domes can be found on **Appendix 3.**

and the direction of the local principal maximum stress for highly inflated domes (**Figure 39**b,c). As we did for cellular analysis, we binned this data according to position in the dome (top vs side, and major vs minor regions, **Figure 39**d). In contrast with cells, nuclei did not present a clear alignment with the stress field. The only region that presented significant alignment is the side-minor axis region of the more eccentric domes. This may suggest that alignment increases with dome eccentricity, but the results are not conclusive.

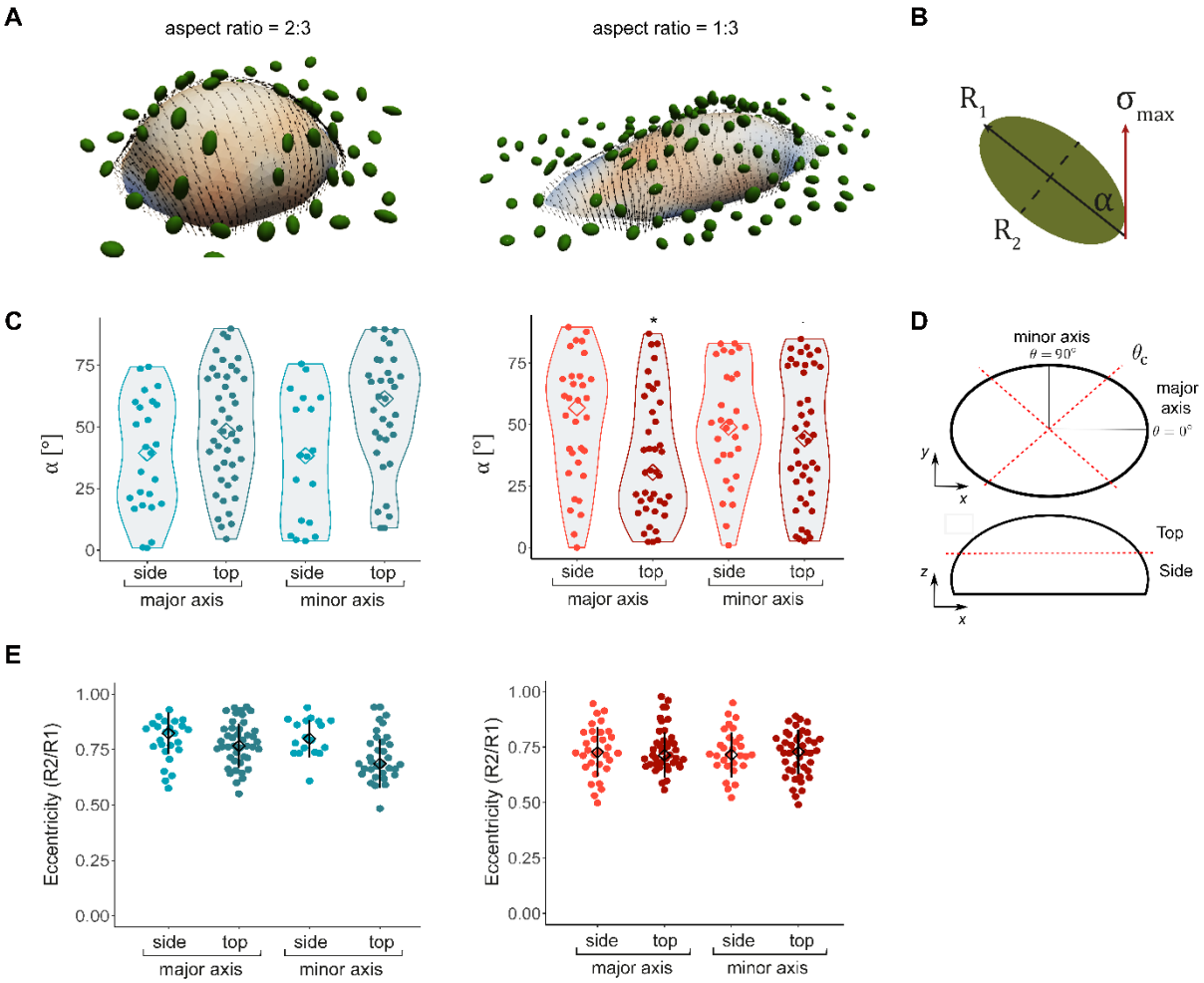

Figure 39: Nuclear alignment and geometry in anisotropic domes. *a, 3D nuclear masks plotted on top of high inflation ellipsoidal domes with 2:3 (left) and 1:3 (right) aspect ratio. The black arrows represent the principal components of the inferred stress. b, Schematic showing the calculation of angle* α *between the longest nuclear axis (*R_1*) and the direction of the maximum principal stress (*σ_{max}*). c, Distribution of angles* α *for the different regions of highly inflated domes. Statistical significance was determined by comparing the median between each distribution and 10000 randomly generated uniform distributions with the same n. d, Schematic indicating the different dome regions in which nuclei were classified. e, Nuclear eccentricity computed as the ratio between the second longest axis (*R_2*) and the longest axis (*R_1*) of the nuclei shown in (c). Data are shown as median ± std of n=25 (major side, left), 43 (major top, left), 18 (minor side, left), 33 (minor top, left), 32 (major side, right), 40 (major top, right), 29 (minor side, right), 42 (minor top, right). c, P = 0.019. *P < 0.05.*

We also tested the eccentricity of the nuclei. To do so, we computed the ratio between the shortest and longest axes of the projected ellipses (R_2/R_1). Nuclei presented aspect ratios ranging from 0.5 to 1. We observed no significant differences in shape between nuclei in different regions (**Figure 39**e). Closer inspection of local anisotropy of the stress field did not reveal any relationship with nuclear alignment or nuclei eccentricity ([d]).

[d] Data on the relationship between the stress field anisotropy, and nuclei alignment and eccentricity can be found on **Appendix 4**.

5 DISCUSSION

In this thesis, we examined systematically the interplay between stress and geometry in epithelia. We combined experimental and theoretical approaches to design MDCK luminal epithelia of arbitrary size and shape, and to map their luminal pressure and stress tensor.

5.1 Size effect on mechanics of domes

We showed that the stress - strain relationship of spherical domes is independent of curvature and differences between apical and basal surface tension. These results suggest that, for the range of sizes studied, curvature is not mechanotransduced into changes in stress. This suggestion is supported by the literature. Even though it is widely known that curvature triggers mechanotransduction at the nanoscale through BAR proteins and amphipatic helix domains[152,153], and at the microscale through proteins such as septins, our experimental results lay beyond this range. Septins can detect curvatures down to 0.7 μm^{-1} (radii smaller than 3 µm)[154] whereas our domes present curvatures between 0.008 and 0.1 μm^{-1}. Our results also indicate that the contribution of bending moments to balance luminal pressure is negligible. Rather, epithelial tension appears to be well captured by a 2D membrane approximation in which stress arises from surface tensions at the actomyosin cortex.

Most circular-footprint domes presented a morphology that closely resembled a spherical cap. However, some of the smallest domes (25 µm-diameter) presented morphologies that

deviated from this ideal shape (**Figure 40**a). We found that luminal pressure tended to plateau for the largest curvatures, which correspond to 25 µm domes (refer to Figure 34a). This tendency to plateau and the deviation from a spherical morphology suggest a change in the behaviour of domes at this scale. We could relate this phenomenon to the recent results from Vasquez *et al* [8]. They showed that small MDCK lumens can expand via a pressure-independent method, where lumen growth occurs by maintaining a constant amount of lumen-facing membrane per cell and sufficient fluid transport to allow luminal growth (**Figure 40**b-d). In Vasquez *et al*, MDCK form spheroids with apical lumens, whose sphericity increases with lumen radius. For large spheroids (around 20 µm-diameter), the lumen becomes more spherical, indicating a transition to pressure-driven inflation. Despite the differences between this system and our domes (notably, the difference in polarity), this transition could explain the heterogeneity of shapes and the low pressures observed in 25 µm domes.

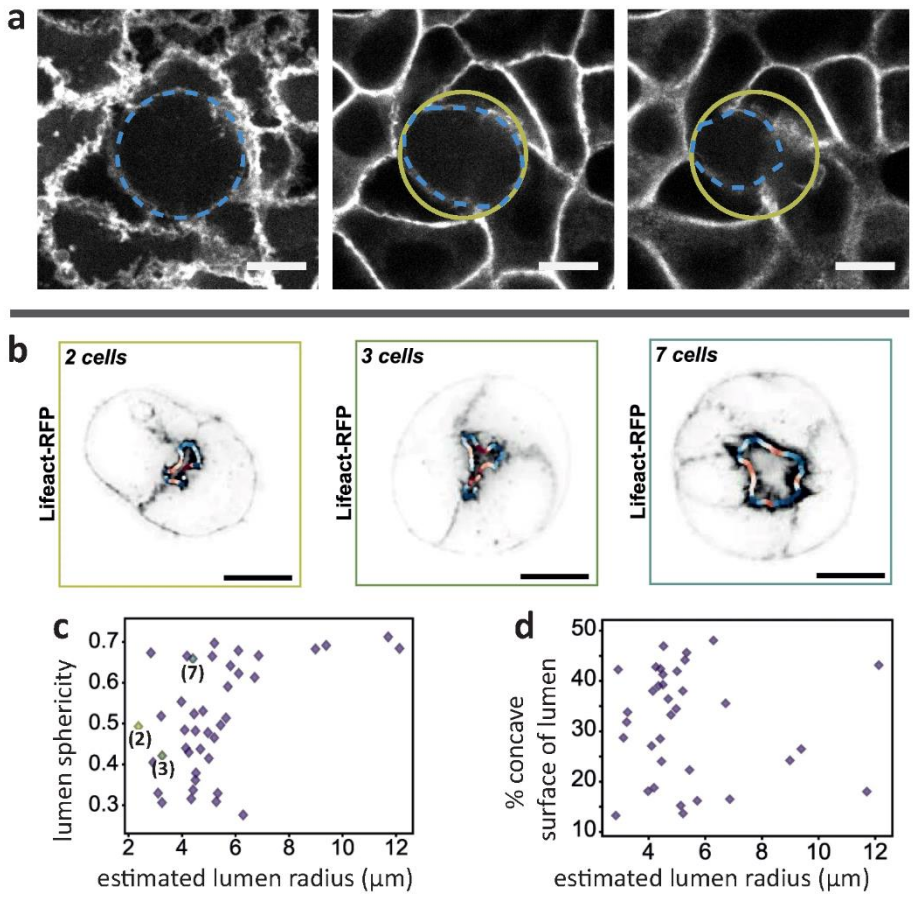

Figure 40: Geometry of 25 µm domes and small MDCK spheroids. *a, Confocal slices of a dome at different heights. Blue indicates the outline of the lumen in each slice. Green indicates the basal lumen outline. b, Single-plane images of MDCK spheroids expressing Lifeact-RFP (gray). The mean lumen curvature is superimposed as a red-blue outline, where red is concave, and blue is convex. c, Lumen sphericities as a function of estimated lumen radius. Values for representative spheroids from (b) labelled by number of cells. d, Percent of lumen surface that is concave (negative curvature) as a function of estimated lumen radius. (b-d) Adapted from ref.* 8

5.2 Anisotropy effect on mechanics of domes

When monolayer shape deviates from a spherical cap, the stresses become anisotropic. To map these stresses, we applied a force inference method based exclusively on epithelium geometry and luminal pressure measurements, without assuming any constitutive behaviour for the membrane material. This property of the method constitutes a great advantage with respect to many models that require the estimation of parameters, because these parameters represent some mechanical characteristics of the materials, and have to be computed from experimental data[155,156].

In elliptical caps and tubes, we found higher stresses along the regions with lower local curvature, consistent with the finding of higher tractions at these points. It is interesting to note that the examination of actin in basal regions of highly anisotropic domes (1:3 ellipses and 1:4 rectangles) reveals the formation of lamellipodia at the regions of low curvature, and

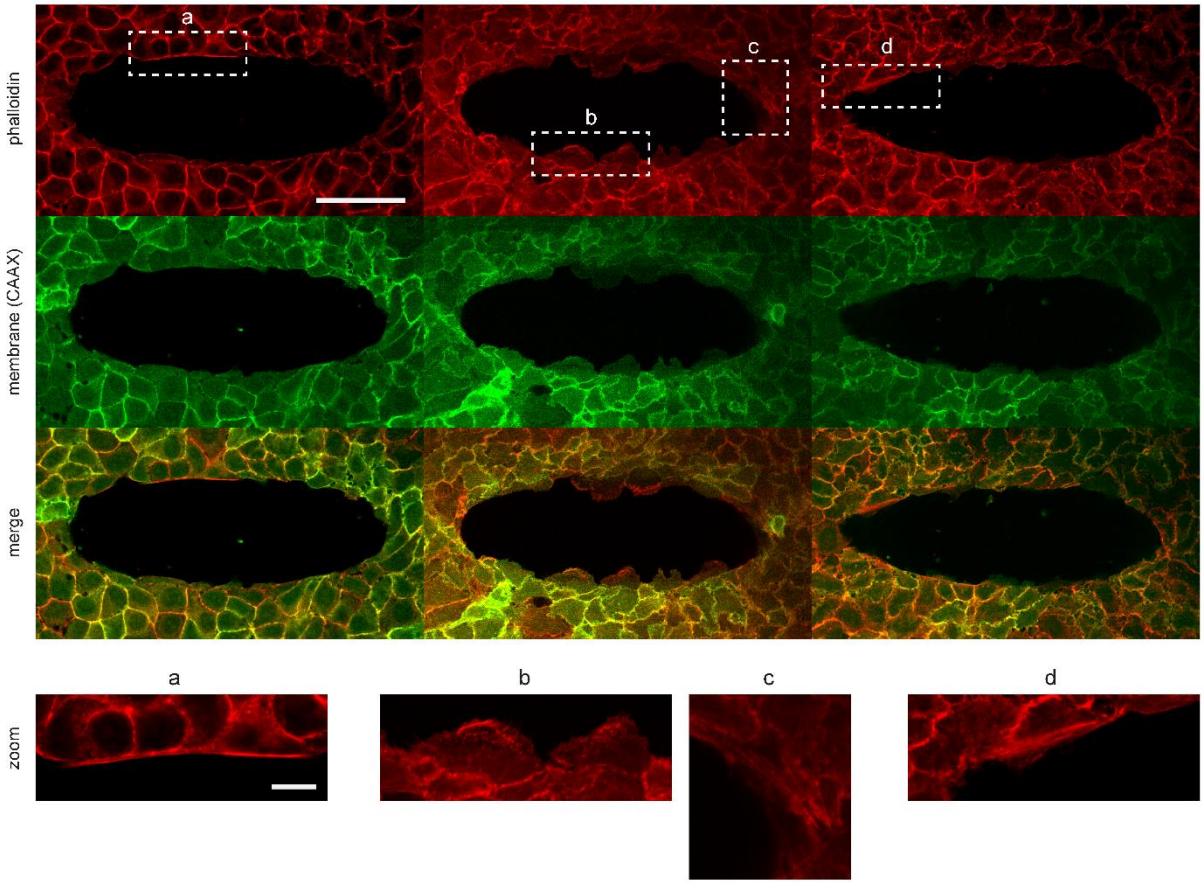

Figure 41: Actin distribution at the dome-substrate interface. *Representative confocal images of the cellular membrane (GFP-CAAX) and actin distribution (phalloidin staining) at the base of ellipsoidal domes with 1:3 aspect ratio. Scale bar: 50 µm. Below: Magnification images of marked regions (a-d). Scale bar: 10 µm.*

the presence of actin cables (**Figure 41**). These features are not contemplated by the model and, therefore, the lowest dome regions are excluded from the analysis.

The shape of epithelia *in vivo* is often influenced by the presence of a basement membrane and by adjacent mesenchymal cells and smooth muscle. This surrounding ECM and tissues drive the emergence of bending moments and buckling instabilities[61,65,71]. In this project, we designed an approach that purposely ignores these confounding factors to be able to study the behaviour of isolated free-standing monolayers under tight mechanical control. However, to explore the contribution of these phenomena in our system, we can modify the geometry of the curved monolayer through optogenetic approaches, such as local modification of contractility[137] or apical constriction[157], or controlled deposition of extracellular matrix[158].

5.3 Cellular and nuclear shape

In anisotropic domes, cells tend to align with the direction of maximal local stress. This alignment is not global, but it increases with dome eccentricity. Cells present a diversity of geometries, ranging from fairly regular cells to very elongated ones. We found no correlation between cell elongation and local stress anisotropy.

Through the approach presented in this thesis, fundamental questions of how epithelial geometry and stress anisotropies influence cellular processes like division[84,159–161], extrusion[162,163] and intercalation[164] can be approached quantitatively. Although these processes are not abundant in the free-standing monolayer, they often occur when the lumen deflates between inflation cycles. This system could therefore be a useful tool to study how the past geometry and mechanical state of the monolayer affect these processes.

It is also interesting to study how inflation-deflation cycles modify density, shape and orientation of cells within the dome. The methodology used in this thesis does not take into account the number of stretch – de-stretch cycles that the domes have been subjected to. This number of cycles may have an impact on the final shape and orientation of cells and, consequently, controlling it may give us an insight into the stress dissipation process carried out by cells. To approach this question (and other questions derived from the study of domes), colleagues in the lab are creating a device to artificially inflate and deflate MDCK monolayers.

This device, coupled with the inference method developed by our collaborators, will allow us to establish a tighter control of the length and magnitude of these stretch – de-stretch cycles and to study the effect of different loading configurations on dome tension and cellular conformation.

Oppositely to cells, nuclei do not seem to align with the direction of the local principal stress. Additionally, they do not appear to deform in the monolayer plane in response to dome inflation and stretching. These results hint to the absence of mechanotransduction linked to nuclear deformation in our experiments[165]. However, we need to carry out further experiments to rule out this hypothesis, such as imaging the location of mechanosensitive transcription activators[165], such as YAP, or studying the conformation of chromatin[166].

5.4 Future Perspectives

The experimental and computational approach developed in this thesis can be applied to the study of the interplay between size, shape, pressure and stress in dome-forming cell types. Dome formation has been reported in many epithelial cell lines in culture, including pulmonary cells, mammary cells, stomach cells, and many types of carcinomas[167]. The geometry and alignment patterns resulting from dome formation in these cells can provide information on their mechanical properties in a controlled lumen formation process.

The relations between the geometry of epithelia, luminal pressure and stress distribution identified in this work can be used for the rational design of organoids and biohybrid devices based on epithelial layers[168].

6 CONCLUSIONS

The main conclusions of this thesis are:

1. We developed a new TFM-compatible protocol to generate curved epithelial monolayers with any desired size and shape.
2. The relationship between stress and strain in epithelial monolayers is largely independent of size and curvature, and insensitive to differences between apical and basal surface tensions.
3. We validated an inference method to map the stress tensor anywhere in a monolayer without assumptions of mechanical properties.
4. In anisotropic luminal epithelia, the stresses are anisotropic, and the maximum principal stress follows the direction of the minor axis of the dome. Tractions and stresses are higher along the regions of less curvature.
5. In ellipsoidal epithelia, cells tend to align with the direction of maximum principal stress. This alignment is non-universal and increases with anisotropy of the epithelium. There is no correlation between alignment or cell eccentricity, and local stress anisotropy.
6. In ellipsoidal epithelia, nuclei are not aligned with the direction of maximum principal stress. There is no correlation between alignment or nuclei eccentricity, and local stress anisotropy.

7 BIBLIOGRAPHY

1. Thompson, D. W. *On Growth and Form*. (Cambridge University Press, 1917).
2. Ross, M. & Pawlina, W. *Histology: A Text and Atlas: With Correlated Cell and Molecular Biology*. (Lippincott Williams & Wilkins., 2015).
3. Chan, C. J. *et al.* Hydraulic control of mammalian embryo size and cell fate. *Nature* **571**, 112–116 (2019).
4. Vasilyev, A. *et al.* Collective cell migration drives morphogenesis of the kidney nephron. *PLoS Biol.* **7**, (2009).
5. Risau, W. Mechanisms of angiogenesis. *Nature* **386**, 671–674 (1997).
6. Hoijman, E., Rubbini, D., Colombelli, J. & Alsina, B. Mitotic cell rounding and epithelial thinning regulate lumen growth and shape. *Nat. Commun.* **6**, (2015).
7. Mosaliganti, K. R. *et al.* Size control of the inner ear via hydraulic feedback. *Elife* **8**, 1–30 (2019).
8. Vasquez, C. G., Vachharajani, V. T., Garzon-Coral, C. & Dunn, A. R. Physical basis for the determination of lumen shape in a simple epithelium. *Nat. Commun.* **12**, 1–12 (2021).
9. Dumortier, J. G. *et al.* Hydraulic fracturing and active coarsening position the lumen of the mouse blastocyst. *Science (80-.).* **365**, 465–468 (2019).
10. Lowery, L. A. & Sive, H. Totally tubular: The mystery behind function and origin of the brain ventricular system. *BioEssays* **31**, 446–458 (2009).
11. Herwig, L. *et al.* Distinct cellular mechanisms of blood vessel fusion in the zebrafish embryo. *Curr. Biol.* **21**, 1942–1948 (2011).
12. Biga LM, Dawson S, Harwell A, Hopkins R, Kaufmann j, LeMaster M, Matern P, Morrison-Graham K, Quick D, and R. J. *Anatomy & Physiology*. (Oregon State University, Creative Commons License).
13. Alberts B. , Johnson A., Lewis J., Morgan D., Raff M., Roberts K. *Molecular Biology of the Cell*. (Garland Science, Taylor & Francis Group, 2015).
14. Kollman, J. M., Merdes, A., Mourey, L. & Agard, D. A. Microtubule nucleation by γ-tubulin complexes. *Nat. Rev. Mol. Cell Biol.* **12**, 709–721 (2011).
15. Jacob, J. T., Coulombe, P. A., Kwan, R. & Omary, M. B. Types I and II keratin intermediate filaments. *Cold Spring Harb. Perspect. Biol.* **10**, (2018).
16. Hardin Jeff, Bertoni Gregory, K. L. J. . *Becker's world of the cell*. (Pearson Benjamin Cummings, 2012).
17. Fletcher, D. A. & Mullins, R. D. Cell mechanics and the cytoskeleton. *Nature* **463**, 485–492 (2010).
18. National University of Singapore. What is the cytoskeleton? (2018). Available at: https://www.mechanobio.info/cytoskeleton-dynamics/what-is-the-cytoskeleton/.
19. Chugh, P. & Paluch, E. K. The actin cortex at a glance. *J. Cell Sci.* **131**, (2018).
20. Prost, J., Jülicher, F. & Joanny, J. F. Active gel physics. *Nat. Phys.* **11**, 111–117 (2015).

21. Kelkar, M., Bohec, P. & Charras, G. Mechanics of the cellular actin cortex: From signalling to shape change. *Curr. Opin. Cell Biol.* **66**, 69–78 (2020).

22. Kechagia, J. Z., Ivaska, J. & Roca-Cusachs, P. Integrins as biomechanical sensors of the microenvironment. *Nat. Rev. Mol. Cell Biol.* **20**, 457–473 (2019).

23. Sun, Z., Costell, M. & Fässler, R. Integrin activation by talin, kindlin and mechanical forces. *Nat. Cell Biol.* **21**, 25–31 (2019).

24. Dufort, C. C., Paszek, M. J. & Weaver, V. M. Balancing forces: Architectural control of mechanotransduction. *Nat. Rev. Mol. Cell Biol.* **12**, 308–319 (2011).

25. Niessen, C. M. Tight junctions/adherens junctions: Basic structure and function. *J. Invest. Dermatol.* **127**, 2525–2532 (2007).

26. Collinet, C. & Lecuit, T. *Stability and dynamics of cell-cell junctions*. *Progress in Molecular Biology and Translational Science* **116**, (Elsevier Inc., 2013).

27. Hatzfeld, M., Keil, R. & Magin, T. M. Desmosomes and intermediate filaments: Their consequences for tissue mechanics. *Cold Spring Harb. Perspect. Biol.* **9**, (2017).

28. Chien, S. *et al.* Rheology of Leukocytes. *Ann. N. Y. Acad. Sci.* **516**, 333–347 (1987).

29. Kollmannsberger, P. & Fabry, B. Linear and nonlinear rheology of living cells. *Annu. Rev. Mater. Res.* **41**, 75–97 (2011).

30. Hoffman, B. D. & Crocker, J. C. Cell mechanics: Dissecting the physical responses of cells to force. *Annu. Rev. Biomed. Eng.* **11**, 259–288 (2009).

31. Barnes, H. A. Rheology: Principles, Measurements and Applications. *Powder Technology* **86**, (1996).

32. Ladoux, B., Mège, R. M. & Trepat, X. Front-Rear Polarization by Mechanical Cues: From Single Cells to Tissues. *Trends Cell Biol.* **26**, 420–433 (2016).

33. Storm, C., Pastore, J. J., MacKintosh, F. C., Lubensky, T. C. & Janmey, P. A. Nonlinear elasticity in biological gels. *Nature* **435**, 191–194 (2005).

34. Gardel, M. L. *et al.* Prestressed F-actin networks cross-linked by hinged filamins replicate mechanical properties of cells. *Proc. Natl. Acad. Sci. U. S. A.* **103**, 1762–1767 (2006).

35. Fernández, P., Pullarkat, P. A. & Ott, A. A master relation defines the nonlinear viscoelasticity of single fibroblasts. *Biophys. J.* **90**, 3796–3805 (2006).

36. Gardel, M. L. *et al.* Elastic behavior of cross-linked and bundled actin networks. *Science (80-.).* **304**, 1301–1305 (2004).

37. Lin, Y. C., Koenderink, G. H., MacKintosh, F. C. & Weitz, D. A. Viscoelastic properties of microtubule networks. *Macromolecules* **40**, 7714–7720 (2007).

38. Trepat, X. *et al.* Universal physical responses to stretch in the living cell. *Nature* **447**, 592–595 (2007).

39. Fabry, B. *et al.* Scaling the microrheology of living cells. *Phys. Rev. Lett.* **87**, 1–4 (2001).

40. Zhang, X. *et al.* Talin depletion reveals independence of initial cell spreading from integrin activation and traction. *Nat. Cell Biol.* **10**, 1062–1068 (2008).

41. Roca-Cusachs, P. *et al.* Integrin-dependent force transmission to the extracellular matrix by α-actinin triggers adhesion maturation. *Proc. Natl. Acad. Sci. U. S. A.* **110**, (2013).

42. Kruse, K., Joanny, J. F., Jülicher, F., Prost, J. & Sekimoto, K. Generic theory of active polar gels: A paradigm for cytoskeletal dynamics. *Eur. Phys. J. E* **16**, 5–16 (2005).

43. Janmey, P. A. *et al.* The mechanical properties of actin gels: Elastic modulus and filament motions. *J. Biol. Chem.* **269**, 32503–32513 (1994).

44. Kruse, K., Joanny, J. F., Jülicher, F. & Prost, J. Contractility and retrograde flow in lamellipodium motion. *Phys. Biol.* **3**, 130–137 (2006).

45. Lecuit, T., Lenne, P. F. & Munro, E. Force generation, transmission, and integration during cell and tissue morphogenesis. *Annu. Rev. Cell Dev. Biol.* **27**, 157–184 (2011).

46. Mertz, A. F. *et al.* Cadherin-based intercellular adhesions organize epithelial cell-matrix traction forces. *Proc. Natl. Acad. Sci. U. S. A.* **110**, 842–847 (2013).

47. Maruthamuthu, V., Sabass, B., Schwarz, U. S. & Gardel, M. L. Cell-ECM traction force modulates endogenous tension at cell-cell contacts. *Proc. Natl. Acad. Sci. U. S. A.* **108**, 4708–4713 (2011).

48. Banerjee, S. & Marchetti, M. C. Continuum Models of Collective Cell Migration. *Adv. Exp. Med. Biol.* **1146**, 45–66 (2019).

49. Fletcher, A. G., Osterfield, M., Baker, R. E. & Shvartsman, S. Y. Vertex models of epithelial morphogenesis. *Biophys. J.* **106**, 2291–2304 (2014).

50. Bi, D., Lopez, J. H., Schwarz, J. M. & Manning, M. L. A density-independent rigidity transition in biological tissues. *Nat. Phys.* **11**, 1074–1079 (2015).

51. Park, J. A., Atia, L., Mitchel, J. A., Fredberg, J. J. & Butler, J. P. Collective migration and cell jamming in asthma, cancer and development. *J. Cell Sci.* **129**, 3375–3383 (2016).

52. Park, J. A. *et al.* Unjamming and cell shape in the asthmatic airway epithelium. *Nat. Mater.* **14**, 1040–1048 (2015).

53. Hannezo, E., Prost, J. & Joanny, J. F. Theory of epithelial sheet morphology in three dimensions. *Proc. Natl. Acad. Sci. U. S. A.* **111**, 27–32 (2014).

54. Latorre, E. *et al.* Active superelasticity in three-dimensional epithelia of controlled shape. *Nature* **563**, 203–208 (2018).

55. Fletcher, A. G., Cooper, F. & Baker, R. E. Mechanocellular models of epithelial morphogenesis. *Philos. Trans. R. Soc. B Biol. Sci.* **372**, (2017).

56. Strutt, D. Organ shape: Controlling oriented cell division. *Curr. Biol.* **15**, 758–759 (2005).

57. LeGoff, L., Rouault, H. & Lecuit, T. A global pattern of mechanical stress polarizes cell divisions and cell shape in the growing Drosophila wing disc. *Dev.* **140**, 4051–4059 (2013).

58. Martin, A. C. & Goldstein, B. Apical constriction: Themes and variations on a cellular mechanism driving morphogenesis. *Dev.* **141**, 1987–1998 (2014).

59. Haigo, S. L., Hildebrand, J. D., Harland, R. M. & Wallingford, J. B. Shroom Induces Apical Constriction and Is Required for Hingepoint Formation during Neural Tube Closure. *Curr. Biol.* **13**, 2125–2137 (2003).

60. Coravos, J. S., Mason, F. M. & Martin, A. C. Actomyosin Pulsing in Tissue Integrity Maintenance during Morphogenesis. *Trends Cell Biol.* **27**, 276–283 (2017).

61. Lecuit, T. & Lenne, P. F. Cell surface mechanics and the control of cell shape, tissue patterns and morphogenesis. *Nat. Rev. Mol. Cell Biol.* **8**, 633–644 (2007).

62. Williams, M., Burdsal, C., Periasamy, A., Lewandoski, M. & Sutherland, A. Mouse primitive streak forms in situ by initiation of epithelial to mesenchymal transition without migration of a cell population. *Dev. Dyn.* **241**, 270–283 (2012).

63. Costa, M., Wilson, E. T. & Wieschaus, E. A putative cell signal encoded by the folded gastrulation gene coordinates cell shape changes during Drosophila gastrulation. *Cell* **76**, 1075–1089 (1994).

64. Burnside, B. Microtubules and Microfilaments in Amphibian Neurulation. **1006**, 989–1006 (1973).

65. Nelson, C. M. On buckling morphogenesis. *J. Biomech. Eng.* **138**, 1–6 (2016).

66. Cerda, E. & Mahadevan, L. Geometry and Physics of Wrinkling. *Phys. Rev. Lett.* **90**, 4 (2003).

67. Soufan, A. T. *et al.* Regionalized sequence of myocardial cell growth and proliferation characterizes early chamber formation. *Circ. Res.* **99**, 545–552 (2006).

68. Richman, D. P., Stewart, R. M., Hutchinson, J. W. & Caviness, V. S. Mechanical Model of Brain Convolutional Development: Pathologic and experimental data suggest a model based on differential growth within the cerebral cortex. *Science (80-.).* **189**, (1975).

69. Tallinen, T., Chung, J. Y., Biggins, J. S. & Mahadevan, L. Gyrification from constrained cortical expansion. *Proc. Natl. Acad. Sci. U. S. A.* **111**, 12667–12672 (2014).

70. Reillo, I., De Juan Romero, C., García-Cabezas, M. Á. & Borrell, V. A Role for intermediate radial glia in the tangential expansion of the mammalian cerebral cortex. *Cereb. Cortex* **21**, 1674–1694 (2011).

71. Shyer, A. E. *et al.* Villification: How the gut gets its villi. *Science.* **342**, 212–218 (2013).

72. Taylor, J. & Adler, P. N. Cell rearrangement and cell division during the tissue level morphogenesis of evaginating Drosophila imaginal discs. *Dev. Biol.* **313**, 739–751 (2008).

73. Butler, M. T. & Wallingford, J. B. Planar cell polarity in development and disease. *Nat. Rev. Mol. Cell Biol.* **18**, 375–388 (2017).

74. Guillot, C. & Lecuit, T. Mechanics of epithelial tissue homeostasis and morphogenesis. *Science (80-.).* **340**, 1185–1189 (2013).

75. Diaz-de-la-Loza, M. del C. *et al.* Apical and Basal Matrix Remodeling Control Epithelial Morphogenesis. *Dev. Cell* **46**, 23-39.e5 (2018).

76. Aigouy, B. *et al.* Cell Flow Reorients the Axis of Planar Polarity in the Wing Epithelium of Drosophila. *Cell* **142**, 773–786 (2010).

77. Nishimura, T., Honda, H. & Takeichi, M. Planar cell polarity links axes of spatial dynamics in neural-tube closure. *Cell* **149**, 1084–1097 (2012).

78. Juriloff, D. M. & Harris, M. J. A consideration of the evidence that genetic defects in planar cell polarity contribute to the etiology of human neural tube defects. *Birth Defects Res. Part A - Clin. Mol. Teratol.* **94**, 824–840 (2012).

79. Godard, B. G. & Heisenberg, C. P. Cell division and tissue mechanics. *Curr. Opin. Cell Biol.* **60**, 114–120 (2019).

80. Petridou, N. I., Grigolon, S., Salbreux, G., Hannezo, E. & Heisenberg, C. P. Fluidization-mediated tissue spreading by mitotic cell rounding and non-canonical Wnt signalling. *Nat. Cell Biol.* **21**, 169–178 (2019).

81. Mao, Y. *et al.* Differential proliferation rates generate patterns of mechanical tension that orient tissue growth. *EMBO J.* **32**, 2790–2803 (2013).

82. Scarpa, E., Finet, C., Blanchard, G. B. & Sanson, B. Actomyosin-Driven Tension at Compartmental Boundaries Orients Cell Division Independently of Cell Geometry In Vivo. *Dev. Cell* **47**, 727-740.e6 (2018).

83. Hertwig, O. Das Problem der Befruchtung und der Isotropie des Eies, eine Theorie der Vererbung. *Jenaische Zeitschrift für Naturwiss.* **11**, 276–318 (1885).

84. Nestor-Bergmann, A. *et al.* Decoupling the Roles of Cell Shape and Mechanical Stress in Orienting and Cueing Epithelial Mitosis. *Cell Rep.* **26**, 2088-2100.e4 (2019).

85. Finegan, T. M. *et al.* Tissue tension and not interphase cell shape determines cell division orientation in the Drosophila follicular epithelium . *EMBO J.* **38**, 1–18 (2019).

86. Wyatt, T. P. J. *et al.* Emergence of homeostatic epithelial packing and stress dissipation through divisions oriented along the long cell axis. *Proc. Natl. Acad. Sci. U. S. A.* **112**, 5726–5731 (2015).

87. Campinho, P. *et al.* Tension-oriented cell divisions limit anisotropic tissue tension in epithelial spreading during zebrafish epiboly. *Nat. Cell Biol.* **15**, 1405–1414 (2013).

88. Schliffka, M. F. & Maître, J.-L. Stay hydrated : basolateral fluids shaping tissues. *Curr. Opin. Genet. Dev.* 70–77 (2019). doi:10.1016/j.gde.2019.06.015

89. Navis, A. & Bagnat, M. Developing pressures: FLUID forces driving morphogenesis. *Curr. Opin. Genet. Dev.* **32**, 24–30 (2015).

90. Chan, C. J. & Hiiragi, T. Integration of luminal pressure and signalling in tissue self-organization. *Dev.* **147**, 1–10 (2020).

91. Clausen, M. V., Hilbers, F. & Poulsen, H. The structure and function of the Na,K-ATPase isoforms in health and disease. *Front. Physiol.* **8**, 1–16 (2017).

92. Madan, P., Rose, K. & Watson, A. J. Na/K-ATPase β1 subunit expression is required for blastocyst formation and normal assembly of trophectoderm tight junction-associated proteins. *J. Biol. Chem.* **282**, 12127–12134 (2007).

93. Brown, P. D., Davies, S. L., Speake, T. & Millar, I. D. Molecular mechanisms of cerebrospinal fluid production. *Neuroscience* **129**, 955–968 (2004).

94. Caplan, M. J., Anderson, H. C., Palade, G. E. & Jamieson, J. D. Intracellular sorting and polarized cell surface delivery of (Na+,K+)ATPase, an endogenous component of MDCK cell basolateral plasma membranes. *Cell* **46**, 623–631 (1986).

95. Wiley, L. M. Cavitation in the mouse preimplantation embryo: Na K-ATPase and the origin of nascent blastocoele fluid. *Dev. Biol.* **105**, 330–342 (1984).

96. Watson, A. J. & Barcroft, L. C. Regulation of blastocyst formation. *Front. Biosci.* 708–730 (2001). doi:10.2741/watson

97. Gordon Betts, J. *et al.* 3.1 The cell membrane. in *Anatomy and Physiology* (OpenStax, 2013).

98. Frizzell, R. A. & Hanrahan, J. W. Physiology of epithelial chloride and fluid secretion. *Cold Spring Harb. Perspect. Med.* **2**, 1–20 (2012).

99. Bagnat, M., Navis, A. & Marjoram, L. Cftr controls lumen expansion and function of Kupffer's vesicle in zebrafish. *Dev.* **140**, 1703–1712 (2013).

100. Yang, B., Sonawane, N. D., Zhao, D., Somlo, S. & Verkman, A. S. Small-molecule CFTR inhibitors slow cyst growth in polycystic kidney disease. *J. Am. Soc. Nephrol.* **19**, 1300–1310 (2008).

101. Maître, J. L. *et al.* Asymmetric division of contractile domains couples cell positioning and fate specification. *Nature* **536**, 344–348 (2016).

102. Bryant, D. M. *et al.* A molecular network for de novo generation of the apical surface and lumen. *Nat. Cell Biol.* **12**, 1035–1045 (2010).

103. Nielsen, J. S. & McNagny, K. M. The role of podocalyxin in health and disease. *J. Am. Soc. Nephrol.* **20**, 1669–1676 (2009).

104. Navis, A. & Nelson, C. M. Pulling together: Tissue-generated forces that drive lumen morphogenesis. *Semin. Cell Dev. Biol.* **55**, 139–147 (2016).

105. Gutzmann, J. H. & Sive, H. Epithelial relaxation mediated by the myosin phosphatase regulator Mypt1 is required for brain ventricle lumenexpansion and hindbrain morphogenesis. *Development* **137**, 795–804 (2010).

106. Rutkowski, J. M. & Swartz, M. A. A driving force for change: interstitial flow as a morphoregulator. *Trends Cell Biol.* **17**, 44–50 (2007).

107. Blum, M., Schweickert, A., Vick, P., Wright, C. V. E. & Danilchik, M. V. Symmetry breakage in the vertebrate embryo: When does it happen and how does it work? *Dev. Biol.* **393**, 109–123 (2014).

108. Lammert, E. & Axnick, J. Vascular lumen formation. *Cold Spring Harb. Perspect. Med.* **2**, 1–9 (2012).

109. Zajac, O. *et al.* Tumour spheres with inverted polarity drive the formation of peritoneal metastases in patients with hypermethylated colorectal carcinomas. *Nat. Cell Biol.* **20**, 296–306 (2018).

110. Leighton, J., Estes, L. W., Mansukhani, S. & Brada, Z. Adenocarcinoma and of Renal Tubular Epithelium. *Cancer* 1022–1028 (1970). doi:10.1002/1097-0142(197011)26:5<1022::aid-cncr2820260509>3.0.co;2-m

111. Leighton, J., Brada, Z., Estes, L. & Justh, G. Secretory Activity and Oncogenicity of a Cell Line (MDCK) Derived from Canine Kidney. *Science (80-.).* **163**, 472–473 (1969).

112. Chan, C. J. *et al.* Hydraulic control of mammalian embryo size and cell fate. *Nature* **571**, 112–116 (2019).

113. Wang, A. Z., Ojakian, G. K. & Nelson, W. J. Steps in the morphogenesis of a polarized epithelium Part I. *Science (80-.).* 137–152 (1990).

114. Tanner, C., Frambach, D. A. & Misfeldt, D. S. Transepithelial transport in cell culture. A theoretical and experimental analysis of the biophysical properties of domes. *Biophys. J.* **43**, 183–190 (1983).

115. Coulombre, A. J. The role of intraocular pressure in the development of the chick eye. I. Control of eye size. *J. Exp. Zool.* **133**, 211–225 (1956).

116. Coulombre, A. J. & Coulombre, J. L. The Role of Intraocular Pressure in the of the Chick Eye. *AMA Arch Ophthalmol* **59**, 502–506 (1958).

117. Swinburne, I. A. *et al.* Lamellar projections in the endolymphatic sac act as a relief valve to regulate inner ear pressure. *Elife* **7**, 1–34 (2018).

118. Fütterer, C., Colombo, C., Jülicher, F. & Ott, A. Morphogenetic oscillations during symmetry breaking of regenerating Hydra vulgaris cells. *Europhys. Lett.* **64**, 137–143 (2003).

119. Ruiz-Herrero, T., Alessandri, K., Gurchenkov, B. V., Nassoy, P. & Mahadevan, L. Organ size control via hydraulically gated oscillations. *Dev.* **144**, 4422–4427 (2017).

120. Northey, J. J., Przybyla, L. & Weaver, V. M. Tissue force programs cell fate and tumor aggression. *Cancer Discov.* **7**, 1224–1237 (2017).

121. Gómez-González, M., Latorre, E., Arroyo, M. & Trepat, X. Measuring mechanical stress in living tissues. *Nat. Rev. Phys.* **2**, 300–317 (2020).

122. Wiederhielm, C. A., Woodbury, J. W., Kirk, S. & Rushmer, R. F. Pulsatile Pressures in the Microcirculation of Frog's Mesentery. *Am. J. Physiol.* **207**, 173–176 (1964).

123. Harris, A. K., Wild, P. & Stopak, D. Silicone Rubber Substrata : A New Wrinkle in the Study of Cell Locomotion. *Science.* **208**, 177–179 (1980).

124. Bergert, M. *et al.* Confocal reference free traction force microscopy. *Nat. Commun.* **7**, (2016).

125. Brugués, A. *et al.* Forces driving epithelial wound healing. *Nat. Phys.* **10**, 683–690 (2014).

126. Delanoë-Ayari, H., Rieu, J. P. & Sano, M. 4D traction force microscopy reveals asymmetric cortical forces in migrating dictyostelium cells. *Phys. Rev. Lett.* **105**, 2–5 (2010).

127. Zhou, J., Pal, S., Maiti, S. & Davidson, L. A. Force production and mechanical accommodation during convergent extension. *Dev.* **142**, 692–701 (2015).

128. Legant, W. R. *et al.* Measurement of mechanical tractions exerted by cells in three-dimensional matrices. *Nat. Methods* **7**, 969–971 (2010).

129. Steinwachs, J. *et al.* Three-dimensional force microscopy of cells in biopolymer networks. *Nat. Methods* **13**, 171–176 (2016).

130. Laplace, Pierre Simon. *Supplément au dixième livre du Traité de Mécanique Céleste: Sure l'Action Capillaire*. (Chez J.B.M. Duprat, 1805).

131. Roca-Cusachs, P., Conte, V. & Trepat, X. Quantifying forces in cell biology. *Nat. Cell Biol.* **19**, 742–751 (2017).

132. Ishihara, S. & Sugimura, K. Bayesian inference of force dynamics during morphogenesis. *J. Theor. Biol.* **313**, 201–211 (2012).

133. Hayashi, T. & Carthew, R. W. Surface mechanics mediate pattern formation in the developing retina. *Nature* **431**, 647–652 (2004).

134. Kong, W. *et al.* Experimental validation of force inference in epithelia from cell to tissue scale. *Sci. Rep.* **9**, 1–12 (2019).

135. Romo, A., Badel, P., Duprey, A., Favre, J. P. & Avril, S. In vitro analysis of localized aneurysm rupture. *J. Biomech.* **47**, 607–616 (2014).

136. Lu, J., Zhou, X. & Raghavan, M. L. Inverse method of stress analysis for cerebral aneurysms. *Biomech. Model. Mechanobiol.* **7**, 477–486 (2008).

137. Valon, L., Marín-Llauradó, A., Wyatt, T., Charras, G. & Trepat, X. Optogenetic control of cellular forces and mechanotransduction. *Nat. Commun.* **8**, (2017).

138. Long, R., Hall, M. S., Wu, M. & Hui, C. Y. Effects of gel thickness on microscopic indentation measurements of gel modulus. *Biophys. J.* **101**, 643–650 (2011).

139. Strale, P. O. *et al.* Multiprotein Printing by Light-Induced Molecular Adsorption. *Adv. Mater.* **28**, 2024–2029 (2016).

140. Alvéole. Micropatterning: Surface functionalization. (2021). Available at: https://www.alveolelab.com/technology/micropatterning-surface-functionalization/.

141. del Álamo, J. C. *et al.* Three-Dimensional Quantification of Cellular Traction Forces and Mechanosensing of Thin Substrata by Fourier Traction Force Microscopy. *PLoS One* **8**, (2013).

142. Álvarez-González, B. *et al.* Three-dimensional balance of cortical tension and axial contractility enables fast amoeboid migration. *Biophys. J.* **108**, 821–832 (2015).

143. Bar-Kochba, E., Toyjanova, J., Andrews, E., Kim, K. S. & Franck, C. A Fast Iterative Digital Volume Correlation Algorithm for Large Deformations. *Exp. Mech.* **55**, 261–274 (2015).

144. Salbreux, G., Charras, G. & Paluch, E. Actin cortex mechanics and cellular morphogenesis. *Trends Cell Biol.* **22**, 536–545 (2012).

145. Schindelin, J. *et al.* Fiji: An open-source platform for biological-image analysis. *Nat. Methods* **9**, 676–682 (2012).

146. Naghdi, P. M. The theory of shells and plates. in *Linear Theories of Elasticity and Thermoelasticity: Linear and Nonlinear Theories of Rods, Plates, and Shells,* 425–640 (Springer Berlin Heidelberg, 1973).

147. Marsden, J. E. & Hughes, J. R. *Mathematical Foundations of Elasticity*. (Dover Publications, 1994).

148. Bonet, J. & Wood, R. D. *Nonlinear Continuum Mechanics for Finite Element Analysis*. (Cambridge University Press, 1997).

149. do Carmo, M. *Differential Geometry of Curves and Surfaces*. (Courier Dover Publications, 2016).

150. Yury. Ellipsoid fit. (2021).

151. Stringer, C., Wang, T., Michaelos, M. & Pachitariu, M. Cellpose: a generalist algorithm for cellular segmentation. *Nat. Methods* **18**, 100–106 (2021).

152. Echarri, A. *et al.* An Abl-FBP17 mechanosensing system couples local plasma membrane curvature and stress fiber remodeling during mechanoadaptation. *Nat. Commun.* **10**, (2019).

153. Del Pozo, M. A., Lolo, F. N. & Echarri, A. Caveolae: Mechanosensing and mechanotransduction devices linking membrane trafficking to mechanoadaptation. *Curr. Opin. Cell Biol.* **68**, 113–123 (2021).

154. Bridges, A. A., Jentzsch, M. S., Oakes, P. W., Occhipinti, P. & Gladfelter, A. S. Micron-scale plasma membrane curvature is recognized by the septin cytoskeleton. *J. Cell Biol.* **213**, 23–32 (2016).

155. Akintunde, A. R., Miller, K. S. & Schiavazzi, D. E. Bayesian inference of constitutive model parameters from uncertain uniaxial experiments on murine tendons. *J Mech Behav Biomed Mater* **96**, 285–300 (2019).

156. Vemaganti, K., Madireddy, S. & Kedari, S. On the inference of viscoelastic constants from stress relaxation experiments. *Mech. Time-Dependent Mater.* **24**, (2020).

157. Martínez-Ara, G. *et al.* Optogenetic control of apical constriction induces synthetic morphogenesis in mammalian tissues. *bioRxiv* 2021.04.20.440475 (2021).

158. Wong, S. W. *et al.* Controlled Deposition of 3D Matrices to Direct Single Cell Functions. *Adv. Sci.* **7**, 1–9 (2020).

159. Ishihara, S., Marcq, P. & Sugimura, K. From cells to tissue: A continuum model of epithelial mechanics. *Phys. Rev. E* **96**, 1–14 (2017).

160. Gudipaty, S. A. *et al.* Mechanical stretch triggers rapid epithelial cell division through Piezo1. *Nature* **543**, 118–121 (2017).

161. Uroz, M. *et al.* Regulation of cell cycle progression by cell-cell and cell-matrix forces. *Nat. Cell Biol.* **20**, 646–654 (2018).

162. Levayer, R., Dupont, C. & Moreno, E. Tissue Crowding Induces Caspase-Dependent Competition for Space. *Curr. Biol.* **26**, 670–677 (2016).

163. Eisenhoffer, G. T. & Rosenblatt, J. Bringing balance by force: Live cell extrusion controls epithelial cell numbers. *Trends Cell Biol.* **23**, 185–192 (2013).

164. Bertet, C., Sulak, L. & Lecuit, T. Myosin-dependent junction remodelling controls planar cell intercalation and axis elongation. *Nature* **429**, 667–671 (2004).

165. Elosegui-Artola, A. *et al.* Force Triggers YAP Nuclear Entry by Regulating Transport across Nuclear Pores. *Cell* **171**, 1397-1410.e14 (2017).

166. Reynolds, N. *et al.* Image-derived modeling of nucleus strain amplification associated with chromatin heterogeneity. *Biophys. J.* **120**, 1323–1332 (2021).

167. Barnes, D., Beaty, G., Bolívar, J. *et al*. *Tissue Culture of Epithelial Cells*. (Plenum Press, 1985). doi:10.1007/978-1-4684-4814-6

168. Clevers, H. Modeling Development and Disease with Organoids. *Cell* **165**, 1586–1597 (2016).

8 APPENDICES

8.1 Appendix 1

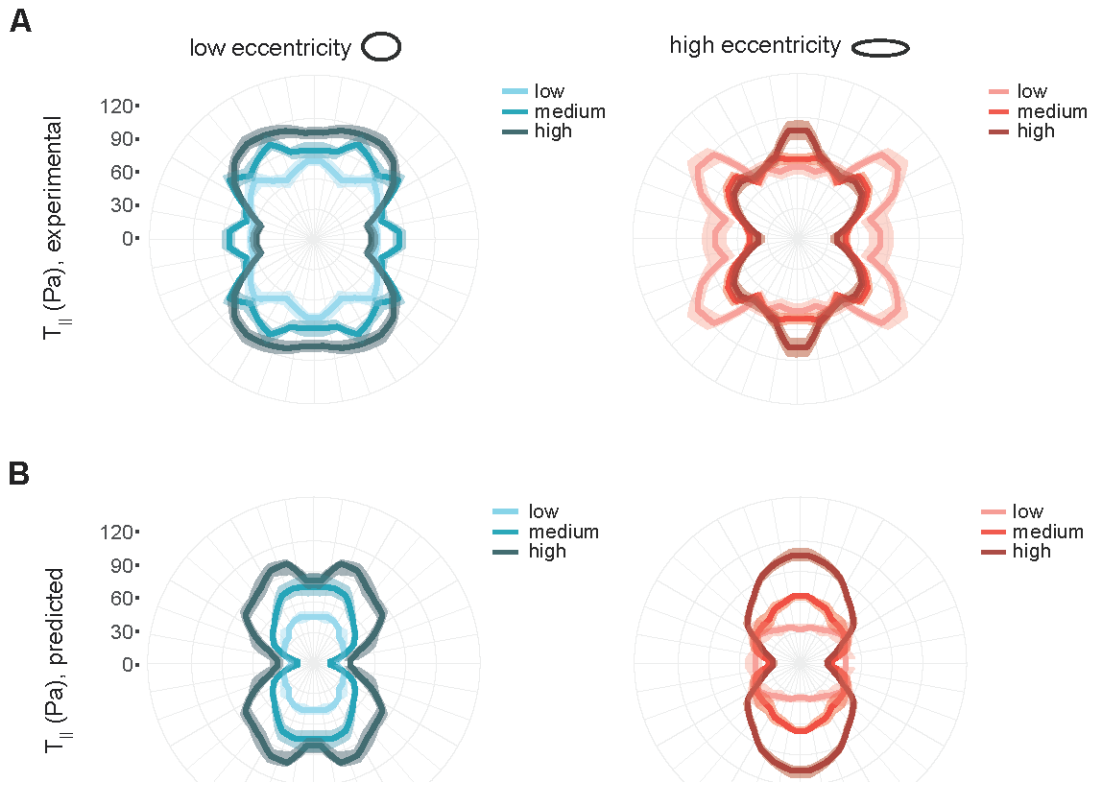

Figure 42: Tangential tractions in ellipsoidal domes with low inflation. *a, Experimental tangential tractions at the dome-substrate interface for low, medium and high inflation levels. Left: low eccentricity. n=13 (low), 27 (medium), 16 (high). Right: high eccentricity. n=10 (low), 15 (medium), 21 (high). The tractions have been averaged in the four quadrants using the symmetry of the system (methods). b, Predicted tangential tractions at the dome-substrate interface for low, medium and high inflation levels obtained with our surface stress inference method. Left: low eccentricity. n=7 (low), 9 (medium), 8 (high). Right: high eccentricity. n=7 (low), 8 (medium), 8 (high). The tractions have been averaged using the symmetry of the system. The line and shaded area indicate median and 95%CI of the median by bootstrapping the data.*

8.2 Appendix 2

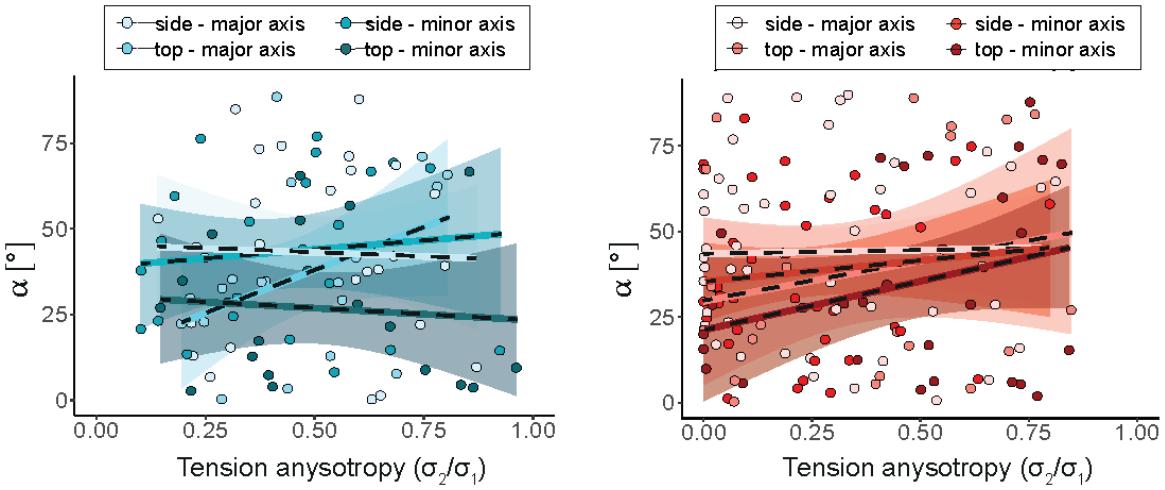

Figure 43: Cell alignment vs Tension anisotropy. *Value of α with respect to local tension anisotropy for cells in highly inflated domes with low eccentricity (left) and high eccentricity (right). Tension anisotropy is computed as the ratio of the second largest component (σ_2) and the largest component (σ_1) of the local principal stress. Data for every dome region (side vs top, minor axis vs major axis) is shown in a different colour. Lines indicate a linear fit of the data. Shaded areas are SE. n=28 (major side, left), 19 (major top, left), 23 (minor side, left), 20 (minor top, left), 51 (major side, right), 45 (major top, right), 42 (minor side, right), 33 (minor top, right).*

8.3 Appendix 3

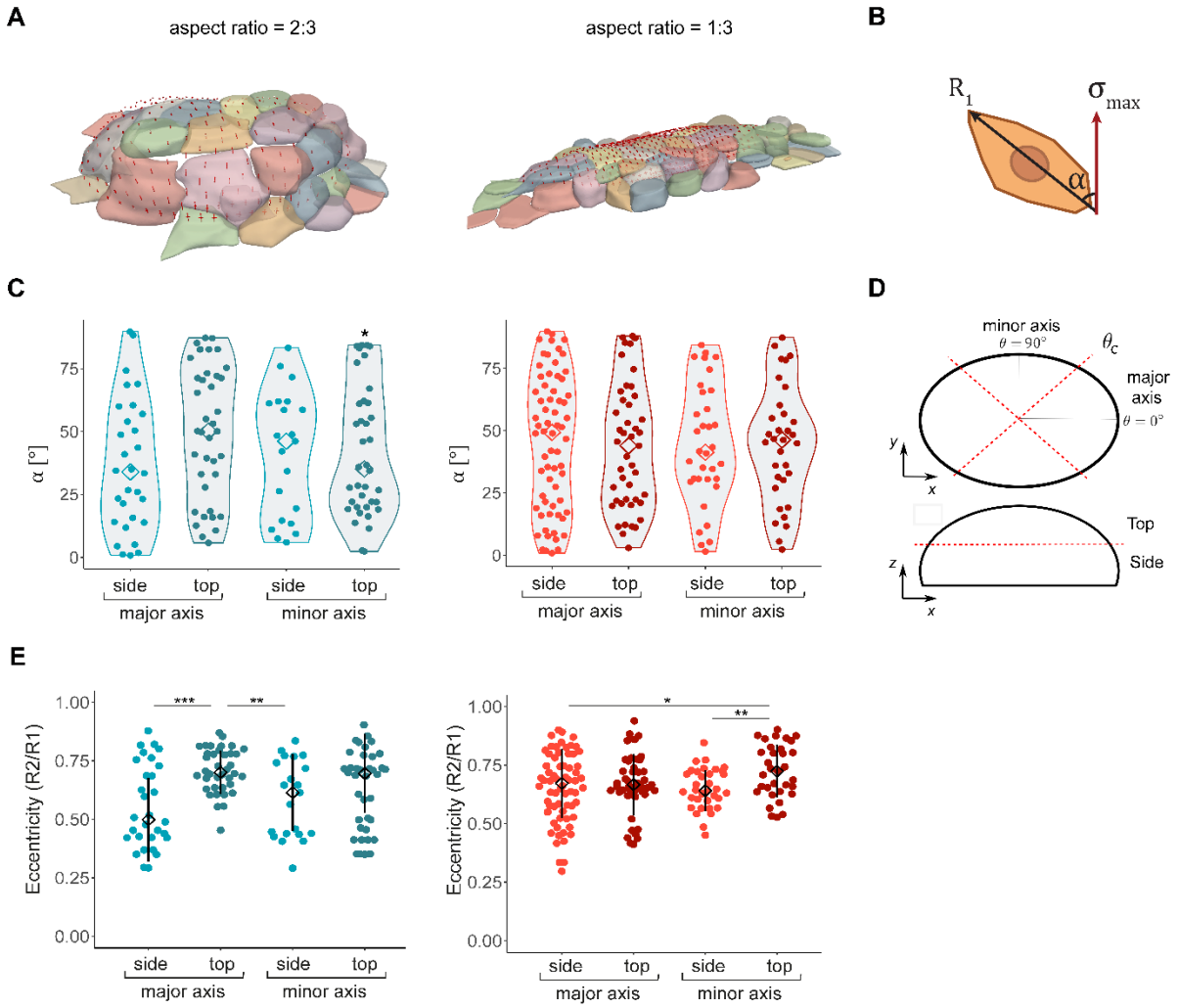

Figure 44: Relationship between stress and cell shape in low inflation anisotropic domes*. a, Segmented cells on top of low inflation ellipsoidal domes with 2:3 (left) and 1:3 (right) aspect ratio. The red arrows represent the principal components of the inferred stress. b, Schematic showing the calculation of angle a between the longest cell axis (R1) and the direction of the maximum principal stress (σ_{max}). c, Distribution of angles a for the different regions of highly inflated domes. Statistical significance was determined by comparing the median between each distribution and 10000 randomly generated uniform distributions with the same* n. *d, Schematic indicating the different dome regions in which cells were classified. e, Cell eccentricity computed as the ratio between the second longest axis (R2) and the longest axis (R1) of the cells shown in (c). Data are shown as median ± sd of n=30 (major side, left), 38 (major top, left), 21 (minor side, left), 38 (minor top, left), 66 (major side, right), 45 (major top, right), 34 (minor side, right), 33 (minor top, right). c, P = 0.019. e, Statistical significance was determined using the Wilcoxon rank sum test for unpaired samples. Only statistically different pairwise comparisons are indicated. Left: P = 5.3e-04 (major side vs major top), 5.5e-03 (major top vs minor side). Right: P = 0.033 (major side vs minor top), 7.7e-03 (minor side vs minor top). *P < 0.05, **P < 0.01 and ***P < 0.001.*

8.4 Appendix 4

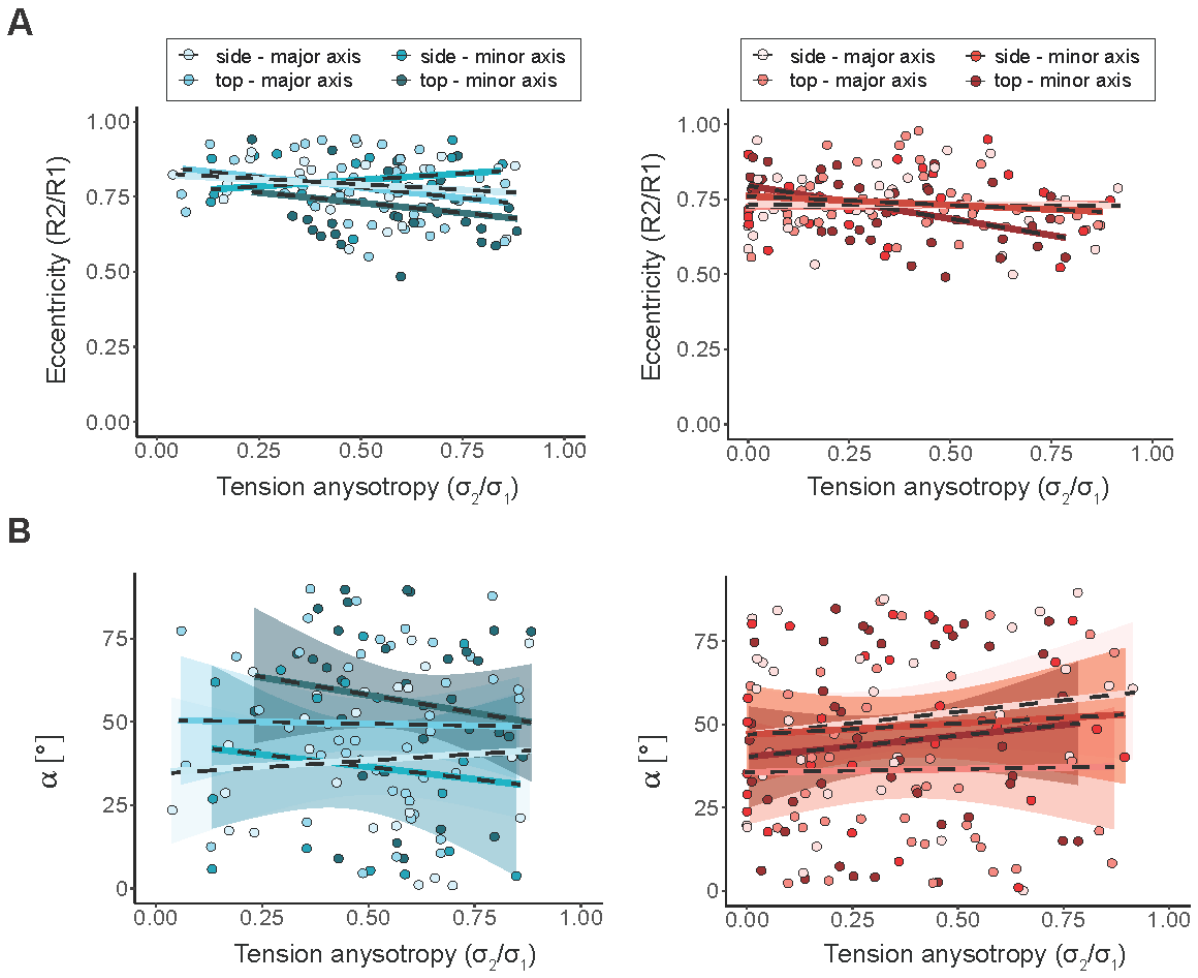

***Figure 45: Effect of tension anisotropy on nuclei geometry and alignment**. a, Value of nuclei eccentricity computed as the ratio between the two radii of the projected ellipse with respect to local tension anisotropy in highly inflated domes with low eccentricity (left) and high eccentricity (right). Tension anisotropy is computed as the ratio of the second largest component (σ_2) and the largest component (σ_1) of the local principal stress. b, Values of α with respect to local tension anisotropy in highly inflated domes with low eccentricity (left) and high eccentricity (right). α is computed as the angle between the longest nuclei axis and the direction of maximal principal stress. Data for every dome region (side vs top, minor axis vs major axis) is shown in a different colour. Lines indicate a linear fit of the data. Shaded areas are SE. n=25 (major side, left), 43 (major top, left), 18 (minor side, left), 33 (minor top, left), 32 (major side, right), 40 (major top, right), 29 (minor side, right), 42 (minor top, right).*